

Pore-Scale Modeling for Interphase Mass Transfer during the VAPEX Process

by

Haisheng Yu

A thesis submitted in partial fulfillment of the requirements for the degree of

Doctor of Philosophy

in

PETROLEUM ENGINEERING

Department of Civil and Environmental Engineering
University of Alberta

© Haisheng Yu, 2024

ABSTRACT

Solvent injection processes offer a promising alternative to steam-based techniques for heavy oil recovery. Multiple mass transfer mechanisms, including interphase mass transfer, diffusion, and convection, would affect the process efficiency and recovery performance. Understanding the mass transfer processes in solvent-based heavy oil recovery processes is fundamental to accurately modeling the solvent/heavy oil interfacial dynamics and designing efficient solvent recovery methods. The pore-scale modeling approaches offer a potential for handling the interface mass transfer in detail and provide some fundamental understanding of macro-scale modeling. However, the traditional interphase methods (e.g., continuous species transfer method) suffer numerical instability issues, especially for convection-dominated cases (Péclet number or $Pe > 1$).

In this thesis, a robust simulation framework based on the level-set method is proposed first to simulate the injection of a vaporized solvent (i.e., propane) into a bitumen-oil system. A pore-scale two-phase multi-component flow simulation is constructed. The solution of the Navier-Stokes equation is coupled with the level-set formulation to track the fluid/fluid interface; a concentration jump is applied to simulate the mass transfer across the gas-liquid interface. The model is validated against several bulk fluid systems where analytical solutions can be derived. The model is tested using a more complex pore-scale system; a macro-scale mass transfer coefficient is estimated based on the linear mass transfer model. For the convection-dominated cases, an artificial diffusion coefficient term was introduced into the interphase mass transfer equation to reduce the numerical stability.

To overcome the issues of numerical instability issues for the traditional interphase mass methods, a conservative LS-C-CST formulation was developed. The new model (LS-C-CST) is suitable for a wider range of Péclet numbers. Compared with the standard LS-CST method, the LS-C-CST method accurately captures the interfacial concentration discontinuity for convection-dominated and significantly reduces the numerical instabilities. This new formulation was validated with a model where the analytical solution exists and compared with the standard CST method. Therefore, the proposed LS-C-CST method can achieve a good accuracy in capturing the interfacial concentration discontinuity for convection-dominated regime. Additionally, the proposed LS-C-CST method is further employed to simulate the interphase mass transfer mechanisms of the VAPEX process. The main mechanisms were captured through simulation studies, including the capillary effect, snap-off mechanisms, and gravity effects. Numerical simulation of the vapor extraction (VAPEX) process with uniform pore structure was studied to reproduce experimental observations. The influence of interfacial mass transfer was explored. Collectively, these contributions provide some insight into the solvent-assisted recovery methods for heavy oil and bitumen production in the future research.

PREFACE

This thesis is an original work by Haisheng Yu. Parts of the research project have been previously published or are ready for journal submission.

Chapter 3 and 4 are composed in part by Yu, H., & Leung, J. Y. (2023). Numerical pore-scale simulation of propane injection for heavy oil displacement processes. *International Journal of Multiphase Flow*, 159, 104319. I was responsible for the conceptualization, methodology, formal analysis, writing – original draft. Leung, J. Y. was the supervisory author and was involved in project administration, funding acquisition, conceptualization, data curation, writing – review and editing.

Chapter 5 and 6 of this thesis represents an original contribution by Haisheng Yu and contains previously unpublished content.

DEDICATION

To my ever-loving and devoted parents, Heqin Bai and Jiasheng Yu

To my beloved wife and son, Yue Lu and Aiden

ACKNOWLEDGEMENT

On the journey of my Ph.D. studies at the University of Alberta, I have gained immense help and support from many individuals. Without this, this dissertation would not have been possible. This journey has been marked by academic rigor and personal growth, and I acknowledge with profound gratitude those who have been instrumental in this process.

I extend my deepest gratitude to my supervisor, Dr. Juliana Y. Leung, for her unwavering support, invaluable guidance, and insightful feedback throughout my Ph.D. journey. Her expertise and dedication have been critical in shaping my research and academic development. She is a good mentor and a devoted researcher who is a role model for me to follow.

I would like to express my special thanks to the members of the examining committee, Dr. Xuehua Zhang, Dr. Japan Trivedi, Dr. Hamid Emami-Meybodi, Dr. Huazhou (Andy) Li, and Dr. Bo Zhang, whose thorough evaluations and constructive criticisms have greatly enriched my dissertation. Their expertise and thoughtful perspectives have significantly enhanced the depth and quality of my work.

I am also profoundly grateful to the Dr. Juliana's research group, a team of brilliant and dedicated individuals. The collaborative environment, stimulating discussions, and shared experiences within this group have been integral to my development as a researcher. Their camaraderie and support have made this journey both enriching and memorable.

Lastly, I extend my heartfelt appreciation to my friends and family for their unwavering encouragement and understanding throughout this challenging and rewarding journey. Special thanks to my wife, Yue Lu, for her endless patience, love, and steadfast

belief in my capabilities. To my son, Aiden, your joy and innocence have been a constant source of inspiration and motivation. Your presence has brought light and balance to my life during the most demanding phases of my academic pursuit.

TABLE OF CONTENTS

ABSTRACT.....	ii
PREFACE.....	iv
DEDICATION.....	v
ACKNOWLEDGEMENT.....	vi
TABLE OF CONTENTS.....	viii
LIST OF TABLES.....	xii
LIST OF FIGURES.....	xiii
LIST OF SYMBOLS.....	xvi
CHAPTER 1: INTRODUCTION.....	1
1.1 Background and Motivations.....	1
1.2 Problem Statement.....	4
1.3 Research Objectives.....	6
1.4 Thesis Outline.....	7
CHAPTER 2: LITERATURE REVIEW.....	9
2.1 History of Solvent-Assisted Recovery Processes.....	9
2.2 Fundamental of the Vapor Extraction (VAPEX) Process.....	10
2.3 Main Mechanisms of the VAPEX Process.....	12
2.3.1 Mass Transfer by Diffusion.....	14
2.3.2 Asphaltenes Precipitation.....	17

2.3.3	Theoretical Analytical Model for VAPEX	18
2.4	Pore-Scale Modelling Methods.....	20
2.4.1	Direct Numerical Simulation (DNS) Methods	22
2.4.2	Pore-Network Modeling (PNM).....	26
2.5	Mathematical Modeling of Interphase Mass Transfer	27
2.6	Marangoni Effect	31
 CHAPTER 3: A TWO-PHASE PORE-SCALE INTERPHASE MASS TRANSFER		
MODELLING USING THE LEVEL-SET METHOD.....		
3.1	Overview.....	34
3.2	Numerical Model	35
3.2.1	Level-Set Method.....	35
3.2.2	Interfacial Mass Transfer Model.....	39
3.3	Numerical Setup and Discretization	41
3.4	Model Validation	42
3.4.1	Validation Case #1 – Capillary Imbibition	42
3.4.2	Validation case #2 – Diffusion-only mass transfer.....	45
3.5	The Wettability Effects on the Waterflooding Process.....	48
3.6	Summary.....	51
 CHAPTER 4: NUMERICAL PORE-SCALE SIMULATION OF TWO-PHASE FLOW		
IMMISCIBLE DISPLACEMENT PROCESSES.....		
4.1	Overview.....	53

4.2	Application Case Studies	53
4.2.1	Application Case #1 - Vaporized Solvent Injection into a 2D Capillary Tube	53
4.2.2	Application Case #2 – Vaporized Solvent Injection in a Natural Porous Medium	58
4.3	Summary	64
CHAPTER 5: A CONSISTENT INTERPHASE MASS TRANSFER METHOD AND LEVEL- SET FORMULATION FOR INCOMPRESSIBLE TWO-PHASE FLOWS		65
5.1	Overview.....	65
5.2	Mathematic Formulation.....	66
5.2.1	Hydrodynamics – Level-Set Method	66
5.2.2	Mass Transfer Model	70
5.3	Discretization Schemes	74
5.4	Validation, Results, and Discussion.....	75
5.4.1	Hydrodynamic Solver Validation – Co-Current Two-Phase Flow.....	75
5.4.2	Coupled Hydrodynamic and Mass Transfer Solver Validation – Two-Phase Displacement.....	77
5.5	Lid-Driven Cavity.....	79
5.6	Summary	87
CHAPTER 6: PORE-SCALE NUMERICAL SIMULATION OF VAPORIZED SOLVENT- BASED PRODUCTION PROCESSES.....		88
6.1	Overview.....	88

6.2	Pore-Scale Mechanisms	89
6.3	Mathematical Formulation.....	93
6.3.1	Hydrodynamics equation	94
6.3.2	LS-C-CST Method.....	96
6.4	Physical Model Description.....	98
6.5	Numerical Scheme	101
6.6	Results.....	103
6.7	Summary.....	109
CHAPTER 7: CONCLUSION AND FUTURE WORK		111
7.1	Summary and Conclusions	111
7.2	Recommendations for Future Work.....	114
BIBLIOGRAPHY.....		117
Appendix A.....		139
Appendix B.....		141

LIST OF TABLES

Table 4.1. Parameters for application case #1.	54
Table 4.2. Parameters for application case #2.	60
Table 5.1. Fluid properties for case #1.	81
Table 6.1. Fluid Properties for Solvent Extraction Experiments (James, 2009).....	100

LIST OF FIGURES

Figure 1.1. The schematic of the VAPEX process: solvent vapor dissolves at the interface, diffuses through the bitumen, diluted heavy oil drainage under gravity effect to the producer.	3
Figure 2.1. Schematic of the Solvent-Assisted Oil Recovery using Two Horizontal Wells (Adapted from James, 2009).....	10
Figure 2.2. Schematic of the Solvent-Bitumen/Heavy Oil Interface and the Related Solvent Concentration Profiles (Modified from James, 2009).	14
Figure 2.3. Mutual Diffusion Coefficients as a Function of Solvent Concentration for Different Types of Solvents (Fayazi and Kantzas, 2019).....	16
Figure 2.4. Bitumen Viscosity as a Function of Asphaltene Content (Luo and Gu, 2005).	18
Figure 2.5. Schematic of Circular Solvent Chamber Evolution Insider a VAPEX physical model: Rising, Spreading, and Falling (Adapted from Lin et al., 2014).....	20
Figure 3.1. Representation of level set method with gas/liquid interface.....	36
Figure 3.2. Schematic diagram of the numerical implementation.	42
Figure 3.3. Schematic of the model setup for validation case #1.	43
Figure 3.4. Interface position as a function of time for validation case #1.....	44
Figure 3.5. Schematic of the model setup for validation case #2.	45
Figure 3.6. Mesh sensitivity analysis.....	46
Figure 3.7. Normalized concentration profiles along line AA' at different times.....	47
Figure 3.8. Schematic of the pore-throat body geometry	49
Figure 3.9. Initial oil saturation for two different cases. (a) The oil saturated pores; (b) oil unsaturated pores.....	49
Figure 3.10. Evolution of the phase distribution for the water-wet state ($\theta = 0$) during the immiscible displacement in oil saturated pores.	50
Figure 3.11. Evolution of the phase distribution for the oil-wet state ($\theta = 180^\circ$) during the immiscible displacement in oil saturated pores.	51

Figure 4.1. Schematic of the model setup for application case #1.	54
Figure 4.2. Simulated normalized concentration profiles at different times.....	55
Figure 4.3. Normalized concentration profile along the capillary tube mid-plane at different times ($Pe = 2$) for application case #1.	55
Figure 4.4. Normalized concentration profiles along the capillary tube mid-plane at different times ($Pe = 200$) for application case #1.	57
Figure 4.5. Schematic of the complex porous medium and related boundary conditions (white area – solid grains; grey area – pore space).	59
Figure 4.6. Phase fraction profiles at different times for application #2.	61
Figure 4.7. Propane concentration profiles at different times for application #2.	61
Figure 4.8. Liquid phase viscosity at different times for application #2.	62
Figure 4.9. (a) Evolution of the mass flux per interfacial area as a function of concentration difference. (b) An enlarged view of late time data (orange circle) illustrates the linear relationship.....	63
Figure 5.1. Representation of the level-set method of the gas-liquid interface.	69
Figure 5.2. Schematic of the layered co-current two-phase flow in a horizontal channel.....	76
Figure 5.3. The velocity distribution in the y-direction at $x = L/2$ for different viscosity ratios..	77
Figure 5.4. Concentration profiles of (a) LS-CST and (b) LS-C-CST approaches at different times for $Pe_{local} = 0.005, 0.5, \text{ and } 50$ cases.....	79
Figure 5.5. Schematic of the single lid-driven cavity.	81
Figure 5.6. Simulated velocity profiles at steady state and concentration fields at different times for different viscosity ratios.	82
Figure 5.7. Average velocity within trapped zone versus viscosity ratio.	83
Figure 5.8. Simulation results for different viscosity ratios. (a) Average concentration in each phase versus time; (b) red curve – Mass flux per interfacial area and concentration difference versus time.	85

Figure 5.9. Mass flux per interfacial area at a particular time versus the corresponding concentration difference for different viscosity ratios.	86
Figure 6.1. The Micromodel Design and Micromodel Pattern.	99
Figure 6.2. Schematic of the Experimental Setup (Modified from Chatzis, 2002).	99
Figure 6.3. Schematic of the computational domain and related boundary conditions (white area – solid grains; grey area – pore space).	102
Figure 6.4. Evolution of the phase distribution during the VAPEX Process in a 2D Micromodel (Grey area – Vapor solvent; dark area - Bitumen).	104
Figure 6.5. Evolution of the vapor solvent concentration distribution during the VAPEX Process in a 2D Micromodel (Grey area – Vapor solvent; dark area - Bitumen).	105
Figure 6.6. (a) Solvent concentration distribution within the porous medium at 500 s; (b) the enlarged area of the swept region near the interface.	106
Figure 6.7. Formation of valleys and peaks at the bitumen/solvent interface (a) Simulation results; (b) experimental results (Chatzis, 2002).	107
Figure 6.8. Pore scale phenomena in VAPEX interfaces: capillary effect, snap-off, and advancing terminal meniscus (a) simulation results at time = 2950 s; (b) experimental observations (Chatzis, 2002).	108
Figure 6.9. VAPEX interface advancement in micromodel.	108
Figure 6.10. Evolution of the average oil viscosity within the porous medium during the VAPEX process.	109

LIST OF SYMBOLS

$\overline{C}_{i,g}$	average normalized concentration of species i , mol/m ³
\vec{n}	normal vector, dimensionless
a	area of the fluid-fluid interface, m ²
C_i	global concentration of component i , mol/m ³
$C_{p,i}$	concentration of species i in phase p , mol/m ³
D	diffusion coefficient, m ² /s
$D_{p,i}$	diffusion coefficient of the species i in phase p , m ² /s
f	Standard level-set function, dimensionless
F_i	convection fluxes, mol/m ² s
F_i	interfacial mass flux, mol/m ² s
F_{st}	surface tension, N/m
g	gravitational vector, m/s ²
H	Henry's constant, dimensionless
H_{sm}	smear-out Heaviside function, dimensionless
I	interface area, m ²
J_i	diffusion fluxes, mol/m ² s
k	Interfacial mass transfer coefficient, m ²
k_i	interfacial mass transfer coefficient, m/s
L	length of the capillary tube, m
L_{char}	characteristic length, m

M	viscosity ratio, dimensionless
P	pressure, Pa
r	diameter of the capillary tube, m
$S_{p,i}$	source term of species i in phase p , mol/m ³ s
t	time, s
u	velocity, m/s
U_0	inlet velocity, m/s
V	grid cell volume, m ³
V_p	volume of the p -phase occupied, m ³
x	position vector, m

Greek Letters:

ρ_l	density of phase l , kg/m ³
μ_l	viscosity of phase l , Pa s
γ	re-initialization parameter, m/s
$\overline{\psi}$	volume-averaged quantities
κ	interfacial curvature, dimensionless
Φ	continuous species transfer compressive term, mol/m ² s
ε	interface thickness, m
ϕ	Smoothed LS function, dimensionless
δ	tuning parameter, dimensionless
σ	surface tension, N/m

ϑ	contact angle, °
δ	thickness of the transition zone, m

Acronyms:

<i>2D</i>	Two-Dimensional
<i>Ca</i>	Capillary Number
<i>CCS</i>	Cyclic Steam Stimulation
<i>CFD</i>	Computational Fluid Dynamics
<i>CST</i>	Continuous Species Transfer
<i>DNS</i>	Direct Numerical Simulation
<i>FEM</i>	Finite Element Method
<i>IFT</i>	Interfacial Surface Tension
<i>LBM</i>	Lattice Boltzmann Method
<i>LS</i>	Level-Set Method
<i>LS-C-CST</i>	Conservative Level-Set Compressive Continuous Species Transfer
<i>N-Solv</i> [®]	Warm VAPEX
<i>PARDISO</i>	Parallel Direct Sparse Solver
<i>Pe</i>	Péclet Number
<i>PFM</i>	Phase Field Method
<i>PNM</i>	Pore-Network Model
<i>SAGD</i>	Steam-Assisted Gravity Drainage
<i>VOF</i>	Volume of Fluid Method

CHAPTER 1 : INTRODUCTION

1.1 Background and Motivations

Heavy oil and bitumen deposits in Canada contain vast hydrocarbon resources; however, the production of these resources is becoming increasingly challenging due to their environmental footprint (Upreti et al., 2007). Heavy oil/bitumen, characterized by its high viscosity (with a lower °API gravity) and trapped within sand grains in shallow geological formations (low pressure), makes producing economically with conventional recovery techniques very difficult. Cold production of lower viscosity heavy oil is possible, known as CHOPS – Cold Heavy Oil Production with Sand. However, it is limited to particular geological formations (e.g., thin and unconsolidated sand reservoirs) and lower production rates (with an average recovery factor of approximately 10%). (Istchenko and Gates 2014; Yu and Leung, 2020). Otherwise, the primary consideration in developing heavy oil reservoirs is reducing its viscosity in economically and environmentally friendly ways. The heavy oil recovery methods of viscosity reduction can be categorized into the thermal method (e.g., SAGD) and mass transfer (solvent diffusion).

Many existing commercial recovery methods involve the injection of thermal energy; for example, steam flooding, steam-assisted gravity drainage (SAGD), and cyclic steam stimulations (CSS) are some of the most widely adopted methods to reduce oil viscosity injecting steam. Despite the relatively high efficiency of these thermal methods, the main drawbacks are that they are energy-intensive and require a considerable amount of water and natural gas to generate steam, contributing to significant greenhouse gas emissions and water usage. In addition, many reservoirs with thin and unconsolidated pay zones, overlying gas

caps, and high-water saturation are not suitable candidates for thermal methods due to excessive heat loss to the over/under-burden. Therefore, alternative solvent-based recovery techniques have been piloted by many operators in recent years. Many alternative methods involve injecting a solvent (mixture of various light hydrocarbons or CO₂) instead of steam to reduce bitumen/heavy oil viscosity. Examples include Vapor Extraction (VAPEX) and warm VAPEX (James, 2009). Solvent-based oil recovery technology was tested in the 1970s by injecting a light hydrocarbon solvent followed by steam (Alikhan and Ali, 1974). The VAPEX process, the solvent analog to SAGD, was later developed (Butler and Mokrys, 1989). In addition to reducing energy consumption, the injected solvents may promote *in-situ* asphaltene precipitation, improving the quality of produced oil (Das and Butler, 1996; Upreti and Lohi et al., 2007; Haghghat and Maini, 2008).

Due to the low molecular diffusion coefficient for most vapor solvent/heavy oil systems, dispersion and convection are typically the dominant mechanisms at the reservoir scale (Boustani and Maini, 2001). In the VAPEX process, the mass transfer of the solvent-heavy oil systems could be enhanced by the diffusive, convective, and interphase mass transfer across the solvent/heavy oil interfaces (e.g., interface renewal, capillary imbibition, and film drainage) (Das, 1998; Yazdani and Maini, 2005; Rostami et al., 2007). Initially, when the injected vaporized solvent drains into the reservoir formation, the front solvent contact with the bitumen can be diffused into the bitumen and reduced viscosity until reaches thermodynamic equilibrium at the interfaces (Mohammadzadeh et al., 2010; Das and Butler, 1998). When the gravity force overcomes the capillary height of imbibition, the diluted heavy oil (live oil) could be drained into the bottom producer. Here, the driving force for molecular diffusion is the concentration difference between the solvent at the live oil/vapor interface

and the solvent concentration within the bitumen. In this process, convective mass transfer can occur at the solvent/bitumen interface during the injection period. Meanwhile, the buoyancy effect arising from the difference in density between vaporized solvent and bitumen leads to the growth of the solvent chamber under the caprock. Then, the solvent chamber spreads laterally outwards, sweeping the oil-bearing formation as the viscosity-reduced oil drains downwards. Complexities of this form exist at different stages of solvent chamber evolution, which are schematically shown in **Figure 1.1**, such as capillarity-driven counter-current local flow in the mixing zone.

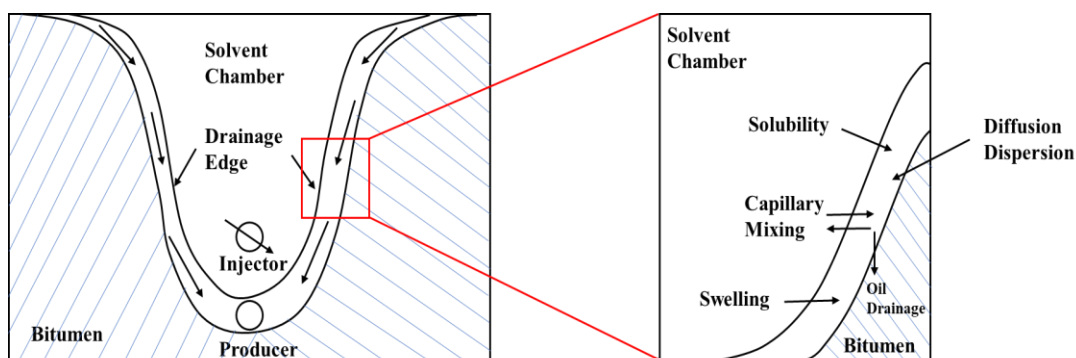


Figure 1.1. The schematic of the VAPEX process: solvent vapor dissolves at the interface, diffuses through the bitumen, diluted heavy oil drainage under gravity effect to the producer.

Although some conventional methods (e.g., core flooding, sand-pack experiments, and reservoir simulations) provide some insight into the recovery process, the actual processes happening within the porous medium still remain unknown (Qi et al., 2017). Indeed, the pore-scale events associated with the solvent injection can further affect the flow properties at larger scales. Most of the current studies focused on the recovery during the process without resolving the pore-scale recovery mechanisms and interfacial interactions

that enable the recovery. Due to the limited information on the physical and chemical processes at relevant scales, diffusion, and dispersion-based mass transfer are not yet understood well, even without the complication of phase changes associated with asphaltene precipitation, transportation, and settling. With the rapid development of imaging and analysis technologies, VAPEX experiments conducted in micromodels (Chatzis, 2002; James, 2009) provide valuable insights on the interactions between phases at the pore level, including capillary effects, wettability, and relative permeability. However, such processes at pore scale are not yet well developed to the extent of incorporating the observed pore-scale phenomena into mathematical models. Thus, a robust pore-scale model of the VAPEX process is needed to formulate ways for representing pore level physics mathematically, which can potentially be used to improve the VAPEX process at relatively larger scales. Understanding the mass transfer processes in solvent-based heavy oil recovery processes is fundamental to accurately modeling the solvent/heavy oil interfacial dynamics and designing efficient solvent recovery methods.

1.2 Problem Statement

The literature review in the next chapter has revealed several limitations in understanding the *in-situ* solvent extraction of heavy oil.

The first challenge is that the current theoretical or numerical model cannot account for the oil production rates from laboratory work, only considering molecular diffusion. Effective diffusivity, two or three orders of magnitude higher than the measured mutual diffusion coefficient, needs to match the experimental results. Moreover, mass transfer in bitumen/solvent systems, diffusion, and convective dispersion-based processes are not yet

understood well, even without considering the phase change associated with asphaltene precipitation/deposition. Most of the current study focuses on the diffusivity of vapor solvents in heavy oil. Indeed, the experimental observations indicate that convective mass transfer plays an important role at the pore-scale. Thus, a robust pore-level mathematical model is necessary to understand the mass transfer mechanisms during the solvent recovery of heavy oil.

The second challenge is that the solvent concentration is not continuous at the bitumen/solvent interface, unlike the heat transfer, referred to as the concentration jumps at the interface. At the pore-scale level, the thermodynamic equilibrium of the system is defined as the ratio of the quality of the chemical potential for each species at the interface, summarized by Henry's law. Thus, it means there is interface mass transfer from one phase to another until it reaches a new equilibrium. On the other hand, mass balance implies the flux continuity across the interface. Thus, a robust and accurate modeling method for simulating the interphase mass transfer in the VAPEX process must satisfy those interfacial boundary conditions, including accurately computing the evolution of the interface movement.

The last challenge is the numerical instabilities issue coming from the dispersion-enhanced mass transfer within the porous medium. As discussed in the previous section, convective dispersion mass transfer plays a significant role in the VAPEX process. This means a larger Péclet number (convection-dominated regime) case, which causes the unphysical oscillations around the interface area. Currently, the main idea of most of the stabilization methods for such a convection-dominated regime is to add an additional diffusive term. Within that, adding an artificial diffusion term into the concentration equation

is the simplest approach to decrease the Péclet number. However, such methods bring the extra unphysical diffusive and compromise the concentration jump at the interface. A more stabilized interphase mass transfer model needs to simulate the VAPEX process where the diffusion coefficients of solvent into heavy oil are very small.

1.3 Research Objectives

The ultimate objective of this research is to develop a robust pore-scale model to simulate vaporized solvent extraction recovery processes to investigate the main mass transfer mechanisms. The corresponding research objectives are summarized as follows:

Develop a robust simulation framework to accurately simulate the solvent/heavy oil interfacial dynamics and capture the interfacial mass transfer mechanisms. The level-set formulation is applied to track the bitumen/solvent interface movement. The pressure velocity distribution is solved by using the Navier-Stokes equations. The computational domain is discretized using the Finite Element Method (FEM).

Combining the interfacial boundary conditions, a single-field interphase mass transfer equation describes the mass transfer across the fluid/fluid interface.

Revisit the conservative level-set equation (C-LS method) to rederive the multiphase species transport equation to maintain the numerical stability for a convective-dominated regime.

The proposed pore-scale mathematical framework needs to be validated against the experimental results. The main mass transfer mechanisms, including diffusion, convection, capillary effect, and gravity effect, are needed to couple into the mathematical model. The

new interfacial knowledge (e.g., the Marangoni effect) induced by the concentration gradient along the interface should also be coupled.

1.4 Thesis Outline

This thesis contains seven chapters. In Chapter 1, the background and motivation of this research are included, then the research objectives are illustrated. Chapter 2 presents a literature review of the history of solvent-assisted extraction recovery processes, the fundamentals of the VAPEX process, and the main mass transfer mechanisms of the VAPEX process. Then, it provides an overview of the current VAPEX analytical model, the current main method of pore-scale modeling.

Chapter 3 provides the developmental and validation processes of the proposed pore-scale modeling based on the level-set method. This framework can be used to simulate the multicomponent interphase mass transfer in the porous medium, such as drainage and imbibition processes.

In Chapter 4, the proposed model developed in Chapter 3 is applied to simulate a convective-dominated case. An artificial diffusion term was introduced into the multicomponent species mass transfer formulation to reduce the numerical oscillations. Then, the proposed model is applied to investigate multicomponent interphase mass transfer in a complex pore-scale system; a macro-scale mass transfer coefficient at the REV scale was computed based on the linear mass transfer model.

Chapter 5 presents a new compressive interphase mass transfer consistent with the conservative level-set method, referred to as the LS-C-CST method. The novelty of this mathematical framework is the introduced compressive term comes from the rederivation of

the conservative level-set equation. It provides good accuracy in simulating species interphase mass transfer, especially for the convective-dominated regime.

In Chapter 6, a VAPEX micromodel was built, followed by the proposed framework in Chapter 5 to capture the main mass transfer mechanisms and compare them with the experimental observations. Indeed, the interface movement velocity was also computed from pore-scale simulation and compared with the experimental results.

Chapter 7 summarizes the conclusions obtained from this thesis and provides some suggestions for future work on this research topic.

CHAPTER 2 : LITERATURE REVIEW

2.1 History of Solvent-Assisted Recovery Processes

Solvent-based oil recovery technology was first tested in the 1970s by injecting a light hydrocarbon solvent followed by steam (Alikhan and Ali, 1974), where Allen (1974) introduced the variation of the ‘huff n puff’ process by utilizing solvents and steam. Later, Allen and Redford (1976) proposed the co-injection of liquid solvents and non-condensable gas into the reservoirs at reservoir conditions. For the consideration of the solvent’s costs and availability, Nenniger (1979) suggested using pure gases or mixtures injected at or below the saturation vapor pressure (e.g., carbon dioxide, methane, and ethane). However, few field tests are conducted during that period due to the low oil production rates and complex field applications (Das and Butler, 1998). It is worth noting that all of the technologies discussed above are based on the vertical injector or production and injection from the same vertical well. With the introduction of the horizontal wells technology and successfully applied to the SAGD process in the 1990s, the solvent-assisted ideas aroused new concerns and focus. A non-porous model (line source Hele-Shaw cells) was conducted by Bulter and Mokrys (1989) to study liquid toluene bitumen extraction processes, and a related theoretical model suggested that the use of solvents may increase the heavy oil recovery efficiency. A typical solvent-assisted heavy oil recovery method using two horizontal wells is illustrated in **Figure 2.1**.

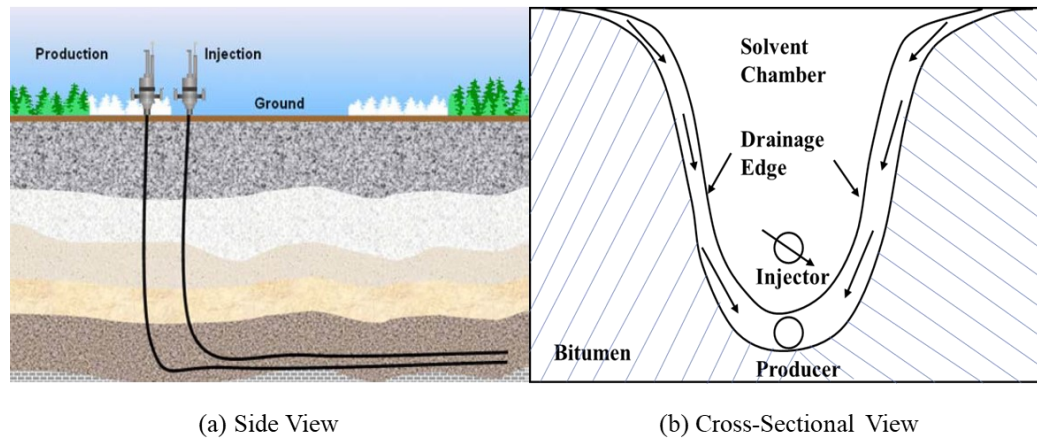


Figure 2.1. Schematic of the Solvent-Assisted Oil Recovery using Two Horizontal Wells
(Adapted from James, 2009)

2.2 Fundamental of the Vapor Extraction (VAPEX) Process

Different solvent-based methods could be classified into non-thermal (non-condensing) and thermal solvent hybrid (condensing) injection processes. For non-condensing solvent extraction processes, either pure or mixed vaporized light hydrocarbon solvents diffuse into the bitumen close to or below the dew point pressure; the diluted oil would drain by gravity into a lower horizontal well. In the case of a condensing solvent extraction process, a heated solvent mixture consisting of hydrocarbons heavier than propane is injected and condenses at the solvent-bitumen interface. The VAPEX process, the solvent analog to SAGD, was later developed (Butler and Mokrys, 1989). Das and Butler (1996, 1998) experimentally investigated the VAPEX performance and the effect of asphaltene precipitation through a series of experiments from a one-dimension Hele-Shaw cell to a two-dimension packed model. They found that oil production increased by 35% with the solvent used by the onset of the deasphalting.

Solvent processes are generally less effective than steam injection because mass transfer due to diffusion/dispersion is generally much slower than thermal energy transfer (e.g., conduction) (Butler and Mokrys, 1991; Mokrys and Butler, 1993; Ardali et al., 2012; Shi and Leung, 2014, 2015;). However, Bulter and Mokrys (1991) and Das (1995) demonstrated experimentally that the extraction rate of solvent processes at the laboratory scale was much higher than theoretical predictions. The other VAPEX experiments in a sand pack conducted by Das and Butter (1998) suggested that interphase mass transfer could also be enhanced by capillary imbibition, surface renewal, and film drainage. All these studies illustrated that interphase mass transfer of the solvent into the bitumen is a key controlling factor. Due to the low molecular diffusion coefficient for most bitumen/solvent systems, dispersion and convection are typically the dominant mass transfer mechanisms at the reservoir scale. At isothermal conditions, such as those encountered in VAPEX, physical mechanisms, including molecular diffusion, convection, and interphase mass transfer, should be considered.

The studies mentioned above revealed that using pure solvent alone may not be practical in the field. Therefore, thermal solvent injection methods, such as warm VAPEX and hybrid VAPEX, have been investigated, including experimental and numerical studies. The patented N-Solv® technology is a condensing solvent extraction process in which heated solvent is injected and condensed at the VAPEX interface (Nenniger and Nenniger, 2001; Rezaei and Chatzis, 2008). The latent heat of the heat solvent transfers to the cold bitumen interface, and the condensed solvent dilutes the bitumen, both of which improve the recovery (Nenniger and Dunn, 2008; Qi et al., 2017). Thus, mass transfer and heat conduction/convection are the main mechanisms in the thermal solvent injection processes. Jiang et al. (2010) conducted a warm solvent soak experiment using butane in Grosmont core samples. The results suggested that the

diffusivity of solvents in the bitumen and overall recovery could be higher than that of solvents used alone in the process. Indeed, as the solvent operating temperatures are between 30 and 120 °C, the energy required is much lower than the SAGD, which means significantly reduced greenhouse emissions (Van 2021; Qi et al., 2017). Several researchers have attempted to model the solvent-based recovery process using different numerical tools. Diffusion and dispersion of solvents into bitumen are the main mechanisms in the solvent-based process. However, transport-related parameters (e.g., diffusion coefficient, dispersion, and mass transfer coefficient) are often treated to be constant in most cases due to the lack of control and understanding of the governing equations of the system. Thus, this resulted in unrealistic input values to match the historical production of the experiments and fields since some of the earlier works by Azin et al. (2005), in which a mechanistic model was developed to simulate the VAPEX process in porous media neglected the capillary effect. This model consists of a 2-D convective-diffusion equation for the constant variable system while a simplified 2-D Brinkmann equation for the flow of the diluted oil. However, they did not address the boundary condition of the system, the correlation for the viscosity, or the molecular diffusion coefficient used within the system. Das (2005) proposed a 2-D field scale model to simulate the VAPEX process using CMG-STARS. This model was used to match the experimental data with different orders of magnitude of diffusion and dispersion coefficient. The final diffusion and dispersion coefficient used, however, was unrealistically high for a gas-liquid system.

2.3 Main Mechanisms of the VAPEX Process

Several experimental studies have been conducted in the past twenty years to study the interphase mass transfer at the pore scale for various solvent-based recovery processes. Glass-etched micromodels coupled with advanced image analysis techniques have facilitated

the direct visualization of bitumen/solvent interface movement. Chatzis (2002) measured the dynamic movement of a bitumen-solvent interface in a pore-scale VAPEX model made of glass beads to elucidate the interphase mass transfer mechanisms. James and Chatzis (2004, 2007, 2009) extended the analysis to study pore-scale mass transfer mechanisms with a set of micromodels. Qi et al. (2017) used a micromodel made of glass beads to study condensing solvent extraction processes and the related displacement processes at the pore scale. Similar micromodel experiments were developed by Xu et al. (2018) to examine the detailed interfacial physics of the steam-solvent co-injection process. The solvent-bitumen/heavy oil interface and the related concentration profile of the solvent-assisted process are shown in Figure 2.2. The mass transfer mechanisms of the solvent-assisted process are highly dependent on whether the solvent condenses or not. In this study, we focus on the non-condensing solvent recovery process (VAPEX). Mass transfer by diffusion, convection of the solvent into the heavy oil, and interphase mass transfer, as well as gravity drainage effect, are the main mechanisms involved in the VAPEX process. There has been lots of discussion about the role of the diffusion and convection dispersion in the VAPEX process (Butler and Mokrys, 1989, 1991; Boustani and Maini, 2001; Das, 1995; James and Chatzis, 2005; Taheri et al., 2010; Moghadam et al., 2008; Wang et al., 2016). One agreement is that diffusion and convection all play a major role in all the solvent-assisted recovery processes but are not quantified properly.

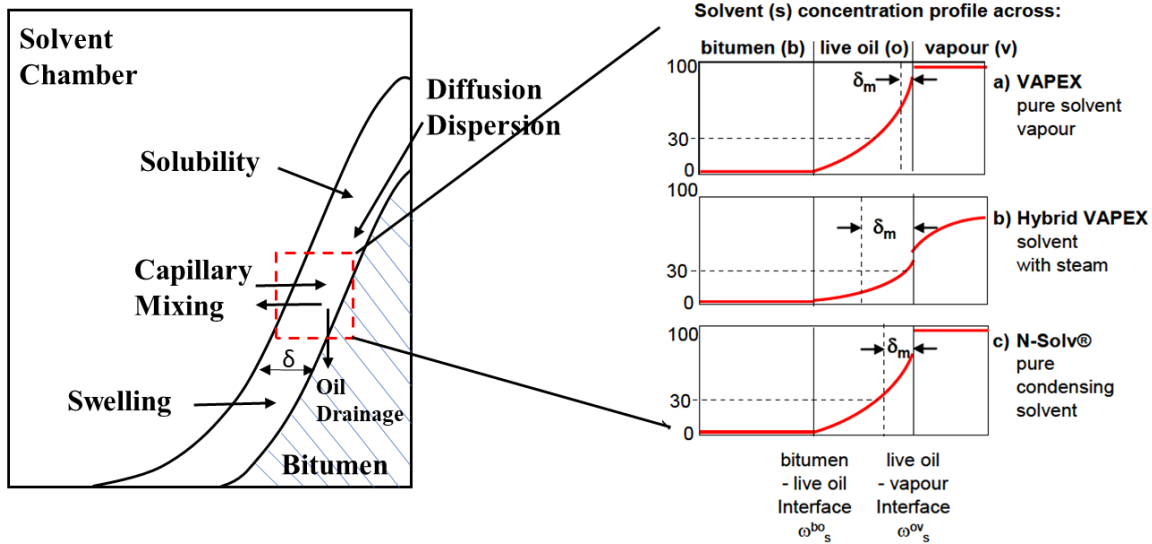


Figure 2.2. Schematic of the Solvent-Bitumen/Heavy Oil Interface and the Related Solvent Concentration Profiles (Modified from James, 2009).

2.3.1 Mass Transfer by Diffusion

As stated earlier, the first part of the process involves the vapor solvent molecules diffusing into heavy oil to reduce the viscosity of heavy oil. Then, the diluted heavy oil would be drained into the bottom producer well under the gravity effect over the capillary and viscous forces at that height. The driving force of molecular diffusion is the solvent concentration gradient between the solvent-rich phase and the heavy oil within the porous medium. Thus, the mass transfer by diffusion mechanism was suggested by Das (1995) to govern this process. The solvent convective dispersion into heavy oil may sometimes happen without diffusion (Mworira et al., 2024). The diffusion process can be defined by three stages. Initially, the diffusion of the vapor solvent molecules diffuses into the solvent-bitumen interface following the solvent concentration gradient. Then, the solvent molecules move across the interface governed by the solvent solubility at certain conditions until they reach thermodynamic equilibrium. After that, the component of the solvent diffuses into the oil

phase, causing the oil to swell, the extent of which is a function of the mutual diffusion coefficient (Fayazi and Kantzas, 2019). Diffusion coefficients were found to be a function of solvent concentration in the heavy oil phase (James et al., 2009; Ghanavati et al., 2014; Fayazi and Kantzas, 2019). With the assumption of the volume change upon mixing of two phases, Perkins et al. (1963) suggested that the net transport of one of the constituents across any arbitrary plane can be described by Fick's diffusion equation.

$$\frac{dG}{dt} = -D_0 A \frac{\partial C}{\partial x} \quad (2.1)$$

where G is the quantity of material diffusing across a plane; D_0 is the molecular diffusion coefficient; A is the cross-sectional area for diffusion; C is the concentration of the solvent.

Typically, the molecular diffusion coefficient (D_0) defined in **Equation 2.1** is a function of solvent concentration. Perkins et al. (1963) mentioned that the molecular diffusion coefficient must be defined as a function of solvent concentration in Equation 2-1 before integration for complete accuracy. However, the mathematics describing behavior with variable diffusion coefficient in **Equation 2.1** is quite complicated (Perkins et al., 1963). Thus, the most common way is to use an effective average diffusion coefficient to describe the diffusion behavior. The constant volume method and constant pressure method are the most general ways to estimate the molecular diffusion coefficient of vapor solvents in heavy oil systems (Khalifa, 2021). However, such experiments suffer long experimentation durations caused by the low molecular diffusion coefficient and low solubility of solvent in heavy oil. As shown in **Figure 2.3**, the mutual diffusion coefficients relationship between the solvent concentration is evaluated by the Vignes diffusivity model (Fayazi and Kantzas, 2019). Due to the low molecular diffusion coefficient for most bitumen/solvent systems,

dispersion and convection are typically the dominant mass transfer mechanisms at the reservoir scale.

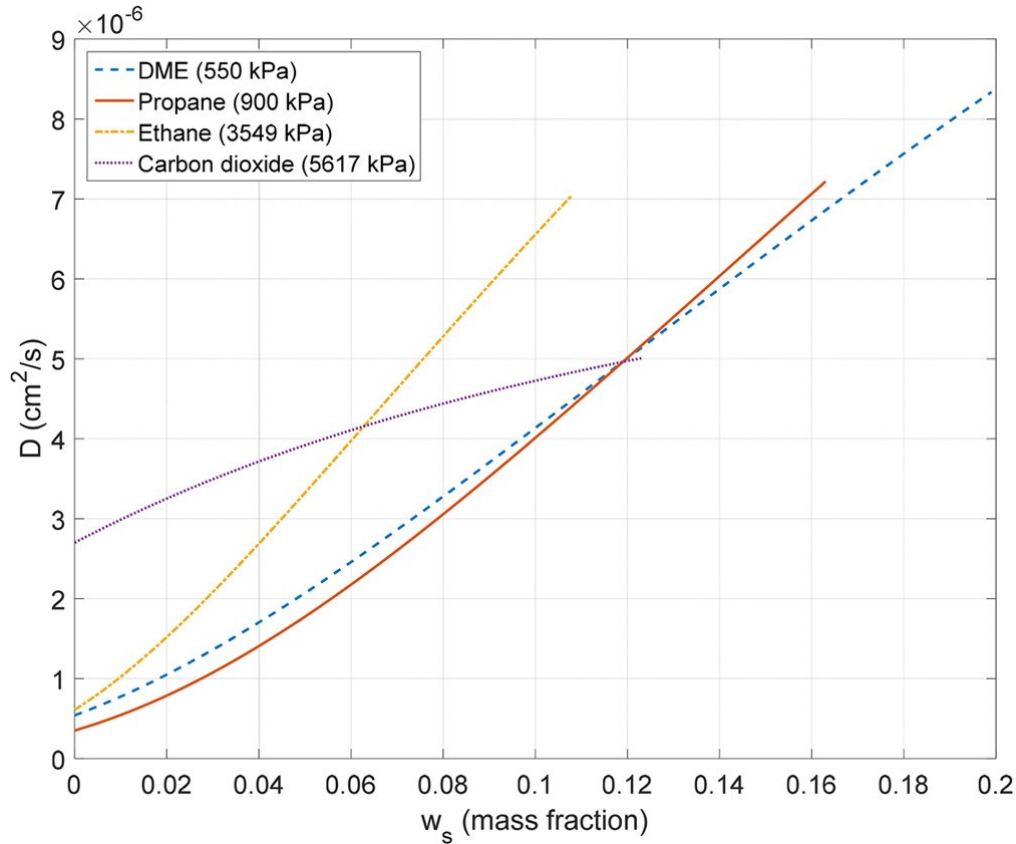


Figure 2.3. Mutual Diffusion Coefficients as a Function of Solvent Concentration for Different Types of Solvents (Fayazi and Kantzas, 2019).

The fundamental criteria in delivering the solvents into the bitumen system are to maintain the highest possible mass transfer driving force with the minimum amounts of solvent used. Due to the diffusion in gas phases being much larger than in liquids and the compressibility of the gas phases, it is suggested that the solvent be injected as a vapor phase with the maximum partial pressure of the solvent (James, 2009). The mixing of the solvent and heavy oil is caused by diffusion and convection dispersion.

2.3.2 Asphaltenes Precipitation

Besides the mixing of the solvent and heavy oil, the precipitation phenomena of asphaltenes were often observed with propane-rich solvents where the operating pressure was above the vapor pressure of propane (Mokrys and Butler, 1993). As shown in **Figure 2.4**, asphaltene precipitation provides a significant viscosity reduction and *in-situ* upgrading of heavy oil (James, 2009). They further found that the ratio of the solvent to heavy oil is required over a certain onset value in order to precipitate asphaltenes, and the onset value is solvent-dependent (Mokrys and Butler, 1993). However, the produced precipitates might block the tiny pores and cause formation damage (formation permeability reduced) (Haghighat and Maini, 2010). A recovery performance test conducted by Li et al. (2020) revealed that the recovery factor for propane solvent is higher than for pentane. The reason behind that is propane precipitants are in a liquid phase with negligible pore plugging but significant capillary trapping (Li et al., 2020). It is also seen that the operating conditions (temperature and pressure), solvent type, and ratio have a significant effect on asphaltenes precipitation. Phase equilibrium behavior evaluation can be used as a tool for screening criteria on VAPEX performance evaluation so as to have an economical design.

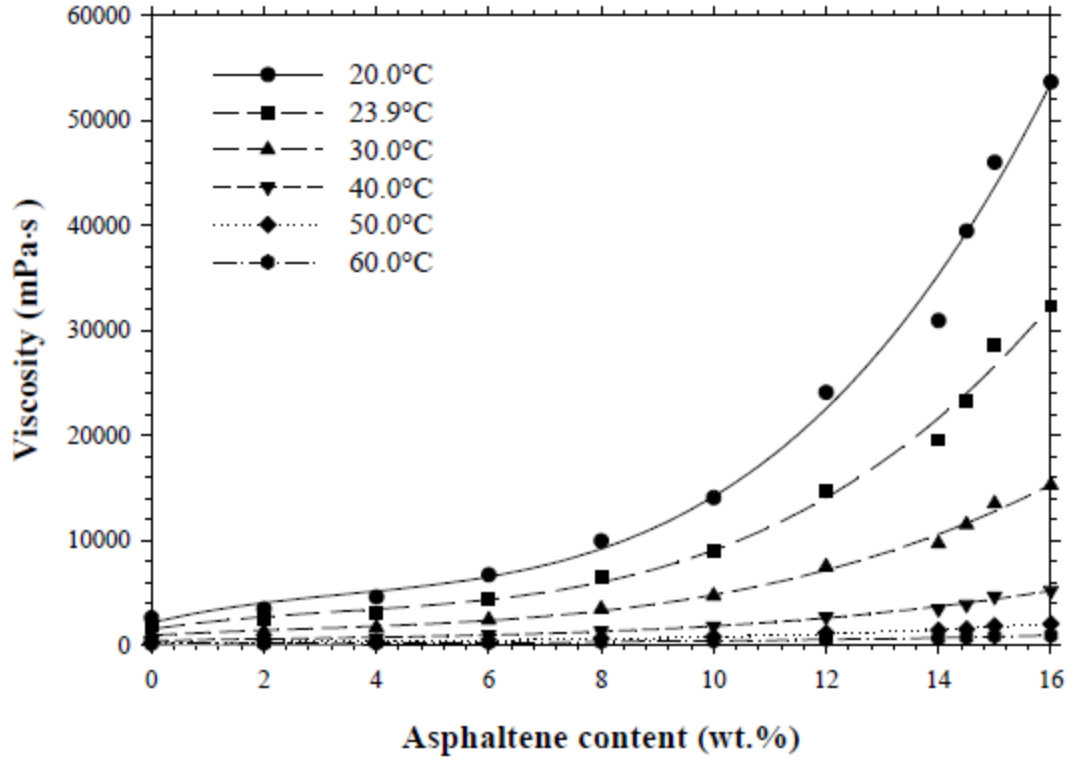


Figure 2.4. Bitumen Viscosity as a Function of Asphaltene Content (Luo and Gu, 2005).

2.3.3 Theoretical Analytical Model for VAPEX

Butler and Mokrys (1989) proposed the first VAPEX mathematical model by combining Fick's second law of diffusion and Darcy's law into the governing equations of the mass and momentum balance, respectively. They made two fundamental assumptions: 1) solvent mass transfer into the bitumen under the pseudo-steady state condition (i.e.,) and 2) constant solvent-bitumen moving velocity in the x-direction. After combining the proper initial and boundary conditions, the final equation for estimating recovery rates is as follows:

$$Q = \sqrt{2kg\phi\Delta S_o h N_s} \quad (2.2)$$

$$N_s = \int_{c_{\min}}^{c_{\max}} \frac{\Delta\rho D_s (1-c_s)}{\mu c_s} dc_s \quad (2.3)$$

where h is the vertical drainage height; k is the permeability; g is gravitational acceleration; ϕ is the porosity; ΔS_o is the oil saturation change in the solvent chamber; the $\phi\Delta S = 1$ for a Hele-Shaw cell; the $\Delta\rho$ is the density difference of the dilute heavy oil and solvent; and the D_s is the diffusion coefficient.

The proposed analytical model indicates that the oil production rate is proportional to the square root of the diffusion coefficient and height of the drainage for a Hele-Shaw cell (porosity = 1). It is noted that Butler and Morkry's model does not include mechanical dispersion and capillary effects and fails to capture the porous medium physics within the porous medium. Later, Das (1995) introduced an apparent diffusion coefficient into Butler and Morkry's model to account for the effect of the porous medium on recovery rates.

$$Q = \sqrt{2kg\phi^\Omega \Delta S_o h N_s} \quad (2.4)$$

where Ω is the cementation factor that counts the effect of sand particles in the matrix.

With the assumption of the solvent chamber growth as a circle with changing center location, Lin et al. (2014) developed a model to predict the oil flow rate during the solvent chamber growth period. The thickness of the transition zone was used as an adjustable parameter between the theoretical model and experimental results.

$$t_r = \Delta t_r \frac{R_0}{\delta_r} \left[\left(\frac{H}{2R_0} \right)^2 - 1 \right] + t_0 \quad (2.5)$$

$$Q(t) = \Delta S_o \phi d \pi R_0^2 \left[\frac{(t-t_0)\delta_r}{\Delta t_r R_0} + 1 \right] \quad (2.6)$$

However, this model also ignored the porous medium and fluid mixing physics effect on the transition zone. Subsequent theoretical analytical models mostly relied on the original development of Butler and Morkry's model. The issue is that all such models assume a

constant thickness of the transition zone as the main adjustable parameter to match the experimental results. However, James (2019) observed that the thickness of the transition zone is a solvent-heavy oil dependency.

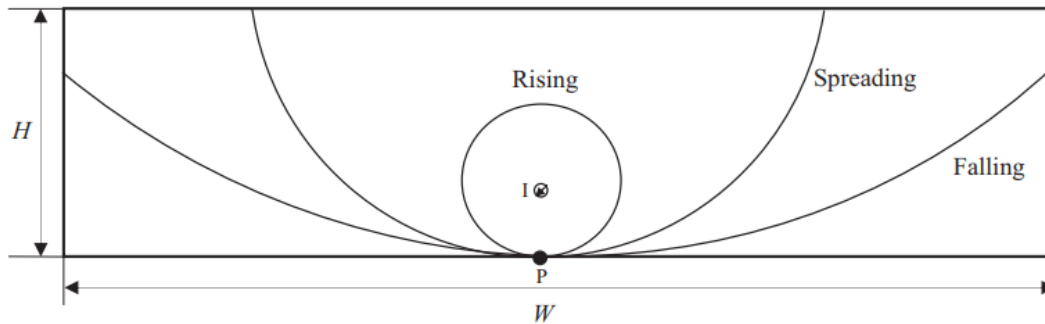


Figure 2.5. Schematic of Circular Solvent Chamber Evolution Insider a VAPEx physical model: Rising, Spreading, and Falling (Adapted from Lin et al., 2014).

2.4 Pore-Scale Modelling Methods

For a wider range of scientific or industrial applications, especially in enhanced oil recovery (e.g., solvent extraction), geological carbon storage, and contamination/remediation, are all involved with interphase mass transfer phenomena, which is the mass transfer of dissolved chemical species (solutes) across the interface from one phase to another (Lake 1989; Yiotis et al., 2001; You and Lee 2022; Agaoglu et al., 2016; Yaksi et al., 2021; Cohen et al., 2015). Interphase mass transfer is a complicated multi-physical process including multiple mechanisms (e.g., diffusion, convection/viscous, capillary) and fully coupled between the multiphase flow and mass transfer in a complex porous medium. With a representative elementary volume (REV) scale approach, the macroscopic effective properties (e.g., porosity, permeability) over a REV of the porous medium are usually defined (**Figure 2.6**). A continuum approach is a standard method used

to simulate the fluid flow at the Darcy scale, where the effective macroscopic properties over the control volume within the porous medium are needed (Molins and Knabner, 2019; Leung, 2014). Since such macroscopic properties are in turn dependent on the microscopic properties of the system, pore-scale related experiments and numerical studies are necessary. Accurate models of such processes have fundamental importance to better understanding the physics of fluids and accurately scale-up the associated processes at a larger-scale (Agaoglu et al., 2015; Jia et al., 1999; Chomsurin et al., 2003; Dillard and Blunt, 2000; Leung and Srinivasan, 2011).

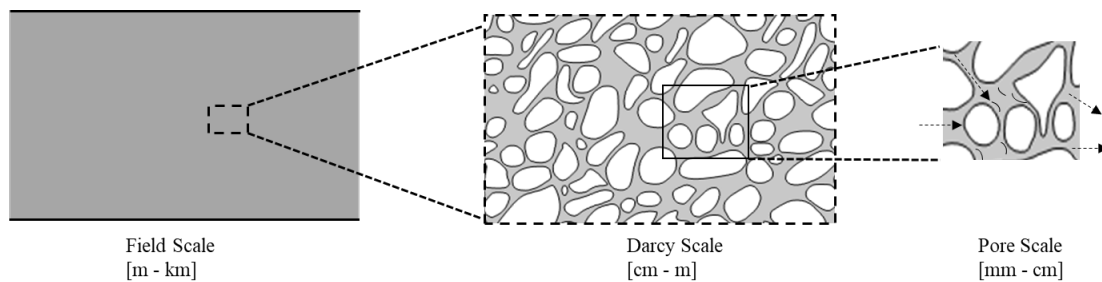


Figure 2.6. Schematic of the Different Scales of Fluid Flow in Porous Medium.

Compared to Darcy-based models, the critical capability of pore-scale modeling is that they can provide details of fluid flow within the void space of a porous medium (Zaretskiy et al., 2010). Two common approaches that can be implemented to simulate the interphase mass transfer at the pore-scale level are direct numerical simulation (DNS) and pore network model (PNM). For the PNM approach, the geometry of the porous medium is a simplified representation of a network of pore throats and bodies, where Poiseuille's law governs flow (Blunt et al., 2002). One drawback of this method is its inability to fully capture fluid flow mechanisms due to the assumption of an immobile dissolving phase and simplified geometry (Basirat et al., 2017; Mehmani and Tchelepi, 2019; Meakin and Tartakovsky, 2009;

Yin et al., 2019; An et al., 2020). In the DNS approach, the relevant governing equations (e.g., Boltzmann or Navier-Stokes equations) are solved directly over the void space within the pore structure. This approach can be further subdivided into the Lattice Boltzmann method (LBM) and grid-based computational fluid dynamics (CFD) (Yu et al., 2005). Several studies were carried out studying interfacial mass transfer using the DNS method of the Navier-Stokes equation, where the relevant governing equations were solved directly over the mesh domain without simplifying the pore geometry. For the CFD approach, the relevant governing equations (e.g., Navier-Stokes and continuity equations) are directly solved within the discretized void space by finite-volume or finite-element techniques, and the interface movement is tracked by an indicator function, such as the volume of fluid (VOF), phase field, and level-set method (LS). In the following section, we will briefly introduce the main pore-scale modeling techniques, respectively.

2.4.1 Direct Numerical Simulation (DNS) Methods

2.4.1.1 Particle-Based Approaches

In the particle-based approaches, fluids are represented as particles, where the fluid properties are computed based on the interactions and neighborhood searches among the particles (Agertz et al., 2007; Ye et al., 2016; Tafuni et al., 2021). The Lattice-Boltzmann Method (LBM) and smoothed particle hydrodynamics (SPH) methods are the two common approaches applied on the multiphase fluid flow in porous medium.

Unlike the traditional CFD methods, where the Navier-Stokes equations solved directly, LBM simplifies the complex interactions of fictive particles into discrete speeds on a lattice based on mesoscopic kinetic equations and microscopic models (Benzi et al., 1992).

Thus, LBM models the fluid flow through such particles' propagation and collision over a discrete lattice. The general form of the LBM equation, which is a discrete version of the Boltzmann equation, can be written as:

$$f_i(x + c\delta_i, t + \delta_t) - f_i(x, t) = \Omega[f_i(x, t)] + F(x, t) \quad (2.7)$$

where $f_i(x, t)$ is the particle distribution function, the population of particles moving in the i -th direction, with velocity v_i at position x at time t . Ω is the collision term, and F is the external force. At a speed in one lattice time step, includes a propagation step where the particles move along discrete lattice direction to the neighboring one and a collision step where particles coming from different directions collide with others towards local equilibrium manner (Golparvar et al., 2018; Guo and Zheng, 2008).

The propagation or streaming step is purely kinematic, which means it only involves the moving of particle distribution function, $f_i(x, t)$ along the lattice direction, c through a time step, δ_t .

$$f_i(x + c\delta_i, t + \delta_t) = f_i(x, t) \quad (2.8)$$

The collision step involves the modification of the particle's distribution based on the local equilibrium between the molecules of a fluid (Bhatnagar et al., 1954). The most common collision operator in LBM is the Bhatnagar-Gross-Krook (BGK) operator, which describes as

$$f_i(x, t + \delta_t) - f_i(x, t) = -\frac{1}{\tau}(f_i(x, t) - f_i^{eq}(x, t)) \quad (2.9)$$

where τ is the relaxation time related to the kinematic viscosity of the fluid, and the left-hand side represents the change in the particle distribution function due to collisions.

Depending on the different configurations of the lattice used (e.g., D2Q9 for two dimensions and nine vectors), the macroscopic properties naturally from the distribution functions at the lattice nodes (Golparvar et al., 2018).

$$\rho = \sum_{i=1}^Q f_i, \quad u = \frac{1}{\rho} \sum_{i=1}^Q f_i c_i \quad (2.10)$$

LBM is the most popular method for multiphase flow simulation at the pore scale (Meakin and Tartakovsky, 2009; Huang et al., 2015; Liu et al., 2015). Fluid-fluid interaction in complex geometries can be readily captured by solving the LB equations for fluid flow and species transport. However, the relation between the interaction forces and fluid dynamics is poorly defined; complex case-dependent calibration procedures are necessary (Ferrari and Lunati, 2013; Frank et al., 2018).

2.4.1.2 Grid-Based Computational Fluid Dynamics (CFD)

The DNS method adopted in this study can directly capture all the physical mechanisms, but it is the most computationally intensive. A computational mesh is constructed over the void space within the pore structure; numerical solutions of relevant governing equations (e.g., Navier-Stokes equation) based on finite-volume or finite-element methods are coupled with interface-tracking methods (e.g., Level-Set or LS, Volume of Fluid or VOF, and Phase Field methods) (Ferrari and Lunati, 2013; Meakin and Tartakovsky, 2009).

The VOF method is the most commonly used approach to simulate the multiphase fluid flow where an indicator function is introduced to represent the interface location (Gopala and Van, 2008). The VOF method is popular due to its mass conservation property; however, it lacks accuracy when modeling the curvature near an interface because of the

discontinuity of its color function (Sussman and Puckett, 2000; Olsson and Kreiss, 2005; Fleckenstein and Bothe, 2015; Alpak et al., 2016). Moreover, the normal vector of the interface and the curvature near an interface are not directly computed with VOF (Alpak et al., 2016). Compared to the VOF method, the LS and Phase Field methods can handle topological changes with high accuracy (Olsson and Kreiss 2005), which defines f_{LS} as a continuous function. The main disadvantage of the classic LS method, however, is that it is not conservative (Sussman and Puckett, 2000; Sun and Tao, 2010). Therefore, Olsson and Kreiss (2005) proposed a conservative LS method by introducing a smeared-out Heaviside function as a level set function. The interface is defined as the zero-isosurface of the field and is not diffusive by construction – as the binary field means that the point is either on one side of the interface or the other side. The geometric descriptors (normal vector and curvature) associated with the LS method are also straightforward to compute compared to the VOF method (Chevalier, 2019). Therefore, the LS method is particularly suitable for simulating multiphase flow in a porous medium exhibiting a wide range of capillary numbers (Xu et al., 2006; Yiotis et al., 2021). The main challenge of modeling interphase mass transfer is imposing the flux continuity and the thermodynamics equilibrium at the interface (i.e., a concentration jump condition) (Maes and Soluaine, 2018). Haroun et al. (2010) proposed a new Continuous Species Transfer (CST) formulation coupled with VOF to tackle this issue. Graveleau et al. (2017) have successfully applied this method to simulate the multi-component mass transfer for subsurface flow.

2.4.2 Pore-Network Modeling (PNM)

In pore network modeling (PNM), the complex pore space of the porous medium is represented as a simplified network of pores and throats (Van Dijk et al., 2004; Blunt et al., 2013). One example of the equivalent PNM of a porous medium shown in **Figure 2.7**.

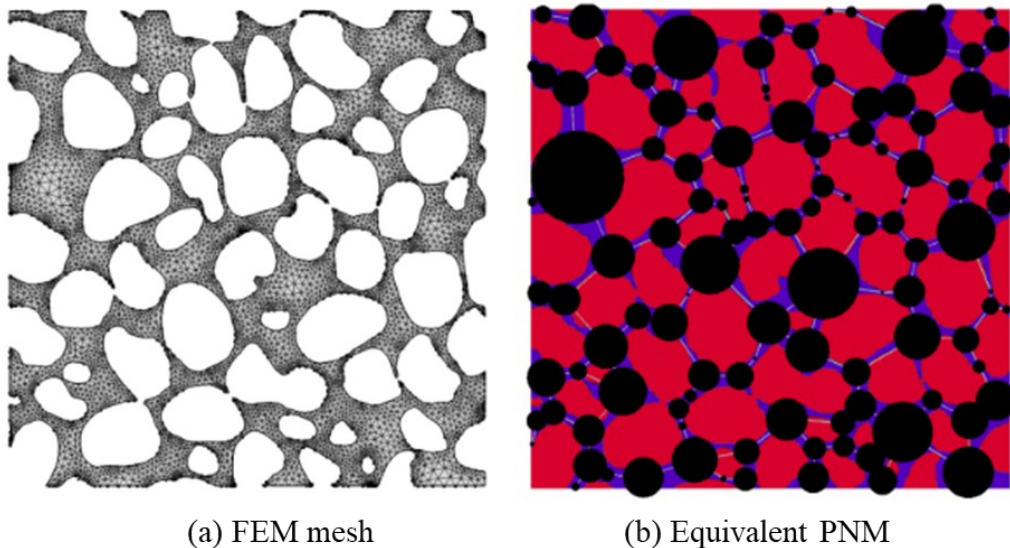


Figure 2.7. An Equivalent Pore Network Modeling of Pores and Throats of a Real Pore Structure (Adapted from Gostick et al., 2016).

Quasi-static and dynamic PNM models are two main approaches used to simulate the multiphase fluid flow in porous medium, the scope of application mainly depends on the fluid flow properties, particularly the capillary number (Blunt, 2001; Blunt et al., 2002). For the capillary force dominated ($Ca < 10^{-5}$) cases, the quasi-static pore network model can be applied to simulate immiscible displacement under capillary pressure equilibrium, neglecting the viscous forces, such as the initial state of the oil recovery (Soll and Celia, 1993; Hui and Blunt, 2000). The main assumptions of the quasi-static modeling are that 1) Newtonian and incompressible; 2) the changes in fluid-flow occur slow enough that the system can be

assumed to be equilibrium at each time step; 3) capillary dominated flow. A mixed wet model with triangular throats model was developed by Hui and Blunt (2002) to investigate the initial oil saturation, spreading efficiency, and wettability effect on relative permeability curve.

In contrast, dynamic pore-network models are generally applied on the regimes where the capillary number is higher ($Ca > 10^{-4}$), where the flow is governed by the Navier-Stokes equations. Unlike the quasi-static models that assumes equilibrium at each time step, dynamic pore-network models account the pressure change over time and have the capability to simulate the dynamic phenomena, like viscous fingering, phase entrapment, and pore-scale mechanisms (Blunt and King, 1991; Blunt and Scher, 1995; Hughes and Blunt, 2000; Joekar-Niasar et al., 2012). Dynamic pore-network models offer an alternative method to capture the dynamic aspects of multiphase flow, especially under non-equilibrium conditions. However, such methods suffer from some limitations: 1) Over-simplification of the real geometry leads to inaccuracies in fluid flow distribution; 2) Dynamic changes of the pore structure due to dissolution or precipitation is hard to capture by using the normal PNMs; 3) Accurately modeling the fluid-fluid interactions, especially includes the complex surface chemistry.

2.5 Mathematical Modeling of Interphase Mass Transfer

Simulating interphase mass transfer phenomena is important for a wider range of subsurface flow applications, such as geological carbon storage, enhanced recovery (e.g., solvent extraction), and contamination/remediation. Interphase mass transfer refers to the mass transfer of dissolved chemical species (solutes) across the interface from one phase to another (Lake, 1989; Yiotis et al., 2001; You and Lee, 2022; Agaoglu et al., 2016; Yaksi et

al., 2021; Cohen et al., 2015). In a complex porous medium, it involves multiple physical mechanisms, including diffusion, convection/viscous, capillary, gravity, and phase equilibrium. A standard continuum approach is to simulate the fluid flow at the Darcy scale, where the effective macroscopic properties over the control volume within the porous medium are needed (Molins and Knabner, 2019; Leung, 2014). Since such macroscopic properties are, in turn, dependent on the microscopic properties of the system, pore-scale related experiments and numerical studies are necessary to estimate these macroscopic properties. Therefore, although pore-scale models are too computationally demanding for simulating these subsurface processes at the field scale, they are for calibrating and studying the interplay between various mechanisms at the pore level and for accurate scale-up of these associated processes at a larger scale (Agaoglu et al., 2015; Jia et al., 1999; Chomsurin et al., 2003; Dillard and Blunt, 2000; Leung and Srinivasan, 2011).

In recent years, with advanced image analysis techniques and increased computational power, considerable efforts have been devoted to investigating the mass transfer across fluid interfaces through numerous experimental and numerical studies. Early experimental works were mainly related to chemical engineering (e.g., segmented flow microreactors and NAPL contamination/remediation) and petroleum recovery technology. Miller et al. (1990) performed experimental studies using a one-dimensional column apparatus to measure the mass transfer between NAPLs and the aqueous phase in a glass bead media system. They observed that the macroscopic mass transfer coefficient is a function of fluid saturation, aqueous phase velocity, and particle size distribution. Yaksi et al. (2021) also investigated the effect of interphase mass transfer on the dissolution rate of the NAPLs in a series of flushing experiments. They illustrated that the interphase mass transfer is directly influenced

by the interfacial contact area, flow properties (e.g., flow rates, path), porous medium properties (e.g., mean grain diameter and pore size distribution), and the distribution of the fluid phases in the pore space. Other authors have also reached similar conclusions (Agaoglu et al., 2015; Liu et al., 2014). In the broader context of solvent-assisted extraction, many experimental and simulation studies were conducted to elucidate the interphase mass transfer mechanisms at the pore-scale level (Chatzis, 2002; James and Chatzis, 2004, 2009; Qi et al., 2017; Xu et al., 2018; Yu and Leung, 2023). Although experimental works provide insights into the physics of interphase mass transfer phenomena, they can be time-consuming, costly, especially on experimental reproducibility, and limited to specific laboratory setups; hence, they may not offer sufficient information about the fluid-fluid interface across a broad range of conditions, rendering the uncertainty. Therefore, pore-scale numerical models can be used as alternative tools for simulating interphase mass transfer over different situations and heterogeneity configurations. This flexibility facilitates quantifying uncertainty macroscopic mass transfer rate for accurate scale-up approaches.

A key challenge for modeling interphase mass transfer in the CFD framework is to ensure flux continuity and thermodynamic equilibrium at the fluid/fluid interface and capture the discontinuity in concentration across the interface (Yang and Mao, 2005; Deising et al., 2016; Maes and Soulaine, 2018; Gao et al., 2021; Yu and Leung, 2023). Haroun et al. (2010) and Marschall et al. (2012) proposed a single-field (one-scalar) model (i.e., a single global concentration] within the algebraic VOF framework, coupled with a Continuous Species Transfer (CST) formulation for reactive liquid films. Deising et al. (2016) developed a more comprehensive VOF-CST formulation with two different forms of the mixture diffusion coefficient definitions. Graveleau et al. (2017) extended the VOF-CST approach to simulate

subsurface fluid flow processes with moving contact lines. However, it was shown that the standard CST formulation leads to significant numerical instability near the interface/front for convection-dominated flow with a high local Péclet number (Pe) dominated by convection near the interface (Yang et al., 2017; Maes and Soulaine, 2018). This led to truncation errors and inconsistencies in the advection operators for both phase fraction and species transport fields (Deising et al., 2016; Yang et al., 2017; Maes and Soulaine, 2018, 2020; Maes and Menke, 2021; Yu and Leung, 2023). Numerical instability is subdued if the flow is diffusion-dominant. Therefore, one approach is to refine the mesh density around the interface to ensure the local $Pe < 0.5$ (Beers, 2007; Yang et al., 2017). Alternatively, some approaches involve the introduction of an artificial diffusion coefficient to mitigate numerical instabilities. However, artificial diffusion or numerical dispersion leads to interface smearing and compromises the ability to estimate the concentration discontinuity (jump) (Yu and Leung, 2023).

Maes and Soulaine (2018) improved the standard CST formulation by adding a compressive term into the concentration equation, known as the Compressive CST approach (C-CST). Their formulation was developed within the algebraic VOF framework, and they demonstrated the potential to yield more accurate results, particularly in a convection-dominated regime ($Pe \geq 100$). Although the algebraic VOF method is great for tracking interface movement due to its robustness and intrinsic mass conservation properties, a significant limitation is its inherent inaccuracy in computing interface curvature due to the discontinuous nature of the step function (Sussman and Puckett, 2000; Olsson and Kreiss, 2005; Fleckenstein and Bothe, 2015; Alpak et al., 2016; Gao et al., 2021).

2.6 Marangoni Effect

Mass transfer induced by surface tension gradient along the interface is named as Marangoni effect. When the surface tension coefficient is constant, a static equilibrium can be reached at the fluid-fluid interface. At this condition, the pressure is discontinuous across the interface with zero velocity due to the surface tension force is exactly balanced by a jump pressure across the interface. The existence of the surface tension gradient at the interface will lead to a slip velocity in the tangential direction on the interface. The reason is that the force arising from the variation of the surface tension acts only in the tangential direction of the interface (Lam et al., 1983). The existence of a surface tension coefficient gradient will eventually cause internal circular flows from regions of low surface tension towards to the regions of high surface tension indicated in **Figure 2.8** (Engberg et al., 2014). The fluid motion due to Marangoni convection can enhance or depress the heat transfer or mass transfer rate (Wegener et al., 2009; Wegener and Paschedag, 2011; Engberg et al., 2014).

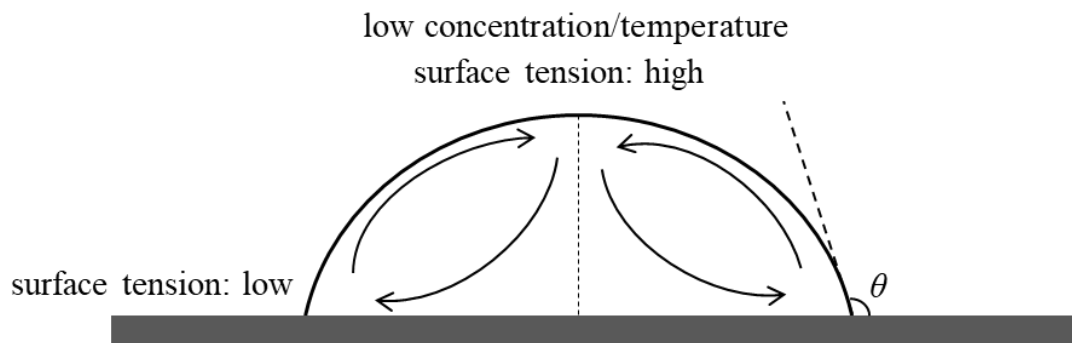


Figure 2.8. Schematic of the Marangoni effect caused by variations in solute concentration or temperature along the interface; The black arrow: direction of fluid flow induced by Marangoni effect; Contact angle, θ .

Sternling and Scriven (1959) developed a 2-D numerical model by combining Navier-Stokes, Fick's first law (diffusion equation), and balancing of interfacial forces to describe this phenomenon. The numerical results indicated that the unbalanced stresses along the interface could produce interface instability and convective fluxes. The Marangoni effect could improve the oil recovery by accelerating the interface oscillations (Groothuis and Zuiderweg, 1960; Lam et al., 1983; Lyford et al., 1998). A Hele-Shaw cell glass beads micromodel was conducted by Lam et al. (1983) to study the recovery of oil droplets by water and propanol flooding. Following the critical Capillary number calculated based on the Sorensen model (1980), they concluded that the Marangoni convection plays a significant role in oil recovery. Pratt (1991) then observed that the Marangoni effect could help to recover the trapped residual oil. Several core flooding and sandpack flooding experiments were conducted by Zhang et al. (2018) to form an emulsion using the interface turbulence (Marangoni effect) to improve heavy oil recovery under waterflooding. The Marangoni effect and mass transfer phenomena were observed by using microscope and nuclear magnetic resonance (NMR), respectively. The results indicated that the Marangoni effect can help to extract the heavy oil by converting interfacial energy into kinetic energy. From the numerical point of view, few studies were focused on the Marangoni effect induced by interphase mass transfer.

Recent research works on Marangoni effect mainly focus on the thermal Marangoni effect, termed as thermocapillary instability (Chen et al., 2015; Engberg et al., 2014; Wang et al., 2022). A 2D mathematical model coupled with the level set method in a moving reference frame was developed by Wang et al. (2008) to simulate the single drops induced mass transfer in liquid-liquid extraction systems. The results showed that the Marangoni

convection increases the mass transfer coefficient. Due to the limitations of the 2D model, nonphysical effects in the rising velocity were reported. A dimensionless number, Marangoni number is to define to quantify the effect of the Marangoni convection. However, up to now there is no general definition, one possibility at isothermal condition is:

$$Ma = -\frac{L\Delta\sigma}{\mu D} \quad (2.11)$$

where L is the characteristic length (e.g., droplet radius, a film thickness); σ is the surface tension; and μ is the dynamic viscosity.

CHAPTER 3 : A TWO-PHASE PORE-SCALE INTERPHASE MASS TRANSFER MODELLING USING THE LEVEL-SET METHOD

3.1 Overview

Solvent injection processes offer a promising alternative to steam-based techniques for heavy oil recovery. Multiple mass transfer mechanisms, including interphase mass transfer, diffusion, and convection, would affect the process efficiency and recovery performance. Understanding the mass transfer processes in solvent-based heavy oil recovery processes is fundamental to accurately modeling the solvent/heavy oil interfacial dynamics and designing efficient solvent recovery methods.

A robust simulation framework based on the level-set method is proposed in this study to simulate the injection of a vaporized solvent (i.e., propane) into a bitumen-oil system. A pore-scale two-phase multi-component flow simulation is constructed. The solution of the Navier-Stokes equation is coupled with the level-set formulation to track the fluid/fluid interface; a concentration jump is applied to simulate the mass transfer across the gas-liquid interface. The model is validated against several bulk fluid systems where analytical solutions can be derived.

The level-set simulation framework is useful for simulating multiphase multi-component interphase mass transfer in porous media. It serves as a tool to examine these different mechanisms' (e.g., diffusive, convective, and interphase mass transfer) interactions and relative importance under various conditions. This chapter presents a new CST formulation coupled with the conservative LS method to simulate the interphase mass transfer at two-phase flow for non-condensing solvent extraction in a pore-scale model. The

simulation is subsequently used to examine the effects and interplay of various mechanisms under different conditions.

3.2 Numerical Model

This section briefly describes the process of the two-phase flow modeling in porous media coupled with the interphase mass transfer at the pore-scale level. First, the Navier-Stokes equations for multiphase flow and the level set method are introduced. Next, the multiphase species transport model is implemented to describe the mass transfer across the interface.

The following simplifications and assumptions are invoked: (1) The solvent molecules can diffuse away from the interface following Fick's law, and the solvent concentration distribution at the gas-liquid interface can be described by Henry's law. (2) Incompressible system. (3) No asphaltene precipitation. (4) Laminar flow. (5) Isothermal conditions. (6) Only mass transfer of component solvent occurs between the phases.

3.2.1 Level-Set Method

The Level-Set method (LS) has been widely adopted to simulate the interface movement between two immiscible phases in pore-scale flow modeling (Ganguli and Kenig, 2011; Li, Huang, and Meakin, 2010; Li and Huang, 2011; Trebotich and Graves, 2015; Zhao et al., 2019). In the standard LS formulation, f_{LS} is defined as a contour of a signed distance function:

$$|f_{LS}| = d(\vec{x}) = \min_{x_i \in I} (|\vec{x} - \vec{x}_i|) \quad (3.1)$$

where I is the interface, \vec{x} is the position vector, and $d(\vec{x})$ is a distance measure; if $f_{LS}(\vec{x}) < 0$, the cell is occupied by phase 1 (liquid); if $f_{LS}(\vec{x}) > 0$, the cell is occupied by phase 2 (gas).

The standard LS equation is given by:

$$\frac{\partial f_{LS}}{\partial t} + \nabla(\vec{u}f_{LS}) = 0 \quad (3.2)$$

To improve numerical robustness, Olsson and Kreiss (2005) formulated a smoothed LS function (ϕ) using the smeared-out Heaviside function, H_{sm} .

$$\phi = H_{sm}(f_{LS}(\vec{x})) = \begin{cases} 0 & f_{LS} < -\varepsilon \\ \frac{1}{2} \left(1 + \frac{f_{LS}}{\varepsilon} + \frac{1}{\pi} \sin\left(\frac{\pi f_{LS}}{\varepsilon}\right) \right) & -\varepsilon \leq f_{LS} \leq \varepsilon \\ 1 & f_{LS} > \varepsilon \end{cases} \quad (3.3)$$

where ε is a numerical parameter equal to half of the smeared-out interface thickness. ϕ varies between 0 and 1, and the interface is located where its value equals 0.5 (Figure 3.1).

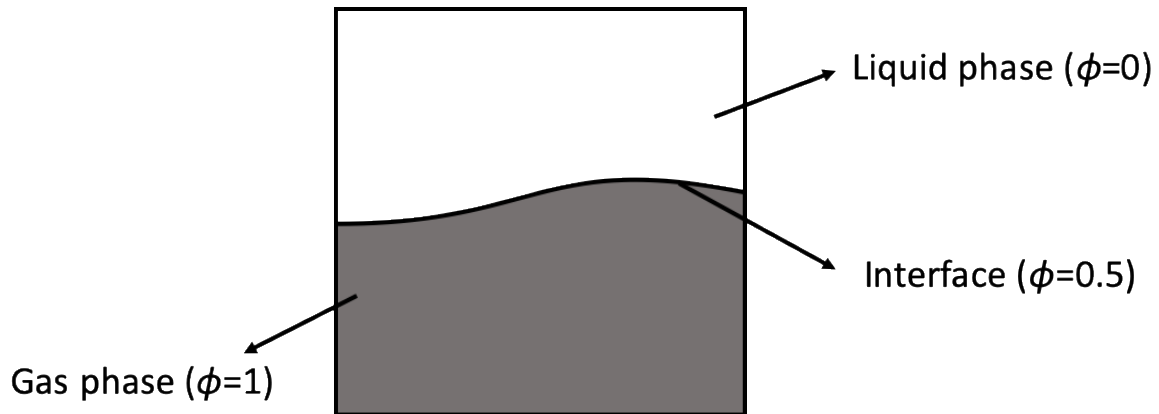


Figure 3.1. Representation of level set method with gas/liquid interface.

As mentioned earlier, the interface movement is tracked based on **Equation 3.2**. Such a movement of the interface causes a change in the LS function, ϕ and thus, the interface thickness would vary along the interface. To achieve a constant interface thickness and reduce the extent of numerical error introduced by the smearing, **Equation 3.2** is modified with a re-initialization term, as shown in **Equation 3.5**, to correct the motion of the interface, while those on the right-hand side are necessary for numerical stability (Olsson and Kreiss, 2005).

$$\frac{\partial \phi}{\partial t} + \vec{u} \cdot \nabla \phi = \gamma \nabla \cdot \left(\varepsilon \nabla \phi - \phi(1-\phi) \frac{\nabla \phi}{|\nabla \phi|} \right) \quad (3.4)$$

where γ is the re-initialization parameter equal to the maximum expected velocity magnitude. The parameter ε is equal to the size of the largest element within the computational domain.; it determines the thickness of the region that ϕ increases smoothly from zero to one, and its value is of the same order of magnitude as the size of an average mesh element.

Other volume-averaged quantities ($\bar{\psi}$), such as the pressure (p) and velocity (\vec{u}) are assigned into the center of the grid cell:

$$\bar{\psi} = \frac{1}{V} \int_{V_p} \psi_p dV \quad (3.5)$$

Where V_p is the volume of the p -phase occupied within the representative grid cell volume V , ψ_p is a quantity associated with the p -phase ($p = l, g$) with ‘ l ’ and ‘ g ’ denoting the liquid phase and gas phase, respectively. Thus, $\bar{\psi}$ it can be defined using the smoothed LS function ϕ :

$$\bar{\psi} = \psi_l * \phi + \psi_g * (1-\phi) \quad (3.6)$$

The fluid density and viscosity, which are considered mixture quantities within the interface region, are defined according to the following equation:

$$\begin{aligned}\rho &= \rho_g + (1 - \phi)\rho_l \\ \mu &= \mu_g + (1 - \phi)\mu_l\end{aligned}\quad (3.7)$$

The solution of **Equation 3.4** is coupled with the Navier-Stokes equation and continuity equation to simulate the moving interface under isothermal conditions:

$$\rho \frac{\partial \vec{u}}{\partial t} + \rho \vec{u} \cdot \nabla \vec{u} = -\nabla p + \nabla \cdot \mu (\nabla \vec{u} + \nabla \vec{u}^T) + \vec{F}_{st} + \rho \vec{g} \quad (3.8)$$

$$\nabla \cdot \vec{u} = 0 \quad (3.9)$$

where F_{st} is the surface tension evaluated numerically with the continuum surface force (CSF) model (Brackbill et al., 1992).

$$\vec{F}_{st} = -\sigma \kappa \vec{n} \nabla \phi \quad (3.10)$$

Where σ is the surface tension coefficient, the interface normal vector \vec{n} and the interfacial curvature κ are determined based on ϕ :

$$\vec{n} = \frac{\nabla \phi}{|\nabla \phi|} \quad (3.11)$$

$$\kappa = -\nabla \cdot \vec{n} \quad (3.12)$$

A wetted wall boundary condition is imposed on the surface of each solid grain for the LS equation, and the contact angle for the wetting phase θ is set to a constant value. The no-slip boundary condition is also applied on the surface of each solid grain.

$$\vec{n}_{wall} \cdot (\varepsilon_{ls} \nabla \phi - \phi(1 - \phi) \frac{\nabla \phi}{|\nabla \phi|}) = 0 \quad (3.13)$$

$$\vec{u} = 0 \quad (3.14)$$

where ε_{ls} represents the interphase thickness and is defined as half of the maximum element size for numerical stability.

3.2.2 Interfacial Mass Transfer Model

Considering a species component i in a multiphase system, the concentration of species i in phase p , $C_{p,i}$ can be expressed by the classical convection-diffusion equation (Bird et al., 1960):

$$\frac{\partial C_{p,i}}{\partial t} + \nabla \cdot (\vec{u} C_{p,i}) = \nabla \cdot (D_{p,i} \nabla C_{p,i}) + S_{p,i} \quad (3.15)$$

where $C_{p,i}$ is the concentration of species i in phase p , and the $D_{p,i}$ is the diffusion coefficient of the species i in phase p . $S_{p,i}$ is the source term of species i in phase p . Henry's law describes the concentration jump across the gas-liquid interface at equilibrium (Haroun et al., 2010):

$$P_g^i = H X_{l,i}^e \quad (3.16)$$

where $X_{l,i}^e$ is the molar concentration of species i in the liquid phase (l) at equilibrium. H is Henry's coefficient, and P_g^i is the partial pressure for species i in the gas phase (g) at equilibrium. Its dimensionless form can be written as:

$$C_{g,i} = H_D C_{l,i} \quad (3.17)$$

where H_D is the dimensionless Henry's constant. $C_{l,i}$ and $C_{g,i}$ is the concentration of species i in the liquid (l) and gas (g) phases, respectively. The continuity of interfacial mass fluxes is imposed:

$$D_l \frac{\partial C_{l,i}}{\partial \vec{n}} = D_g \frac{\partial C_{g,i}}{\partial \vec{n}} \quad (3.18)$$

To rewrite the transport equation in terms of the global concentration of component i , C_i , the formulation by Haroun et al. (2010a, 2010b), Marschall et al. (2012), and Deising et al. (2016) is followed:

$$C_i = \phi C_{l,i} + (1 - \phi) C_{g,i} \quad (3.19)$$

The corresponding transport equation involving C_i is:

$$\frac{\partial C_i}{\partial t} + \nabla \cdot (F_i) = \nabla \cdot J_i \quad (3.20)$$

where

$$\begin{aligned} F_i &= C_{l,i} \phi \vec{u} + C_{g,i} (1 - \phi) \vec{u} = C_i \vec{u} \\ J_i &= \phi D_{l,i} \nabla C_{l,i} + (1 - \phi) D_{g,i} \nabla C_{g,i} \end{aligned} \quad (3.21)$$

The convection and diffusion fluxes F_i and J_i are described in terms of global variables. Haroun et al. (2010a, 2010b) proposed a new one-field equation, referred to as the Continuum Species Transfer (CST) method, that couples **Equation 3.21** and the interface boundary conditions (i.e., **Equations 3.18 and 3.19**):

$$J_i = D_i \nabla C_i + \Phi \quad (3.22)$$

where

$$\Phi = D_i \frac{C_i(1-H)}{\phi + H(1-\phi)} \nabla \phi \quad (3.23)$$

Thus, combining **Equation 3.20** to **3.23**, the final transport equation can be expressed as:

$$\frac{\partial C_i}{\partial t} + \underbrace{\nabla \cdot (\vec{u} C_i)}_{\text{convection}} = \underbrace{\nabla \cdot (D_i \nabla C_i)}_{\text{diffusion}} + \underbrace{\nabla \Phi_i}_{\text{discontinuity}} \quad (3.24)$$

At the solid boundary (e.g., grain surface), $\nabla C_i = 0$. Finally, an explicit coupling strategy is adopted for solving all the equations: at each time step, the velocity/pressure field and phase fraction field are first computed using **Equations 3.4, 3.8, and 3.9**; the results are then used in **Equation 3.24** to compute the concentration distribution field.

3.3 Numerical Setup and Discretization

A novel workflow that integrates the relevant mechanisms of multiphase flow and mass transfer (as described in the previous section) is implemented. A flow chart of the general coupling strategy is shown in **Figure 3.2**. The key procedures are introduced:

[Multiphase Flow Model + Interface Tracking Model]: Solve the Navier Stokes equation and the LS equation to calculate ϕ , \vec{u} , and p .

[Mass Transfer Model]: Calculate C_i with the updated effective diffusion coefficient (**Equation 3.15**).

The mathematical model is implemented using a commercial finite-element-based solver COMSOL Multiphysics 5.5 (2019). The spatial discretization is performed with the limited linear differencing scheme. The governing partial differential equations are solved by the COMSOL linear solver - parallel direct sparse solver (PARDISO) (COMSOL, 2019). Time stepping is solved with the backward Euler method. The adaptive time-steeping scheme adjusts the timestep size automatically to maintain the desired relative tolerance. The convergence criteria are based on the weighted Euclidean normal of the solution-based estimated relative error. The mesh size is refined according to the complexity of the geometry and interface thickness. Readers should refer to the manual in the COMSOL Multiphysics® Reference Manual, Version 5.5 (COMSOL Inc., 2019) for further details.

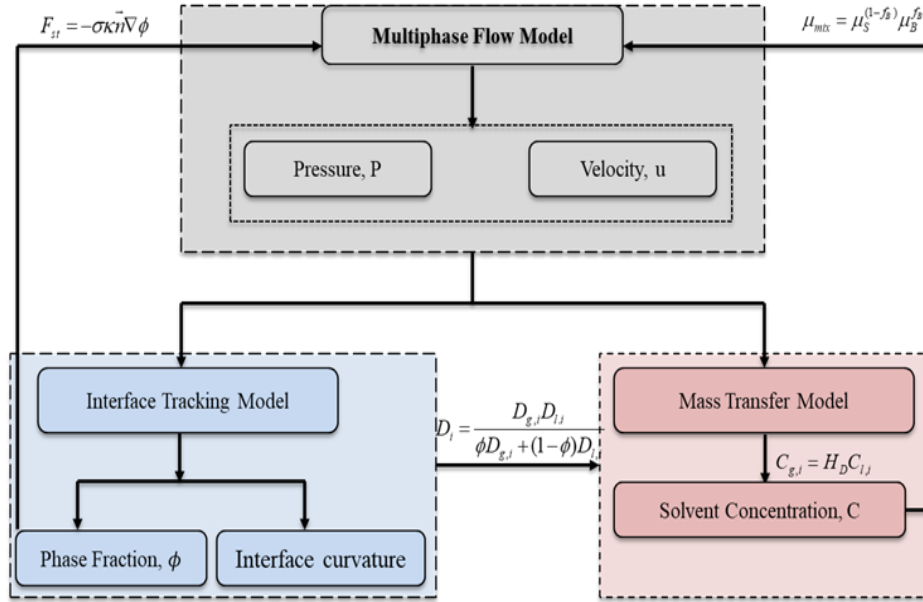


Figure 3.2. Schematic diagram of the numerical implementation.

3.4 Model Validation

In this section, two simple cases are presented. Model results are compared against the analytical solutions, and mesh sensitivity is also analyzed.

3.4.1 Validation Case #1 – Capillary Imbibition

A simple case is designed to model the capillary imbibition of two immiscible fluids. A schematic of the model setup is shown in **Figure 3.3**. A two-dimensional (2D) domain of $10\ \mu\text{m} \times 350\ \mu\text{m}$, as shown in **Figure 3.3**, is considered. Initially, a portion of the domain (a capillary tube of $L = 200\ \mu\text{m}$) is filled with the non-wetting fluid. Wetting and no-slip boundary conditions (**Equations 3.13** and **3.14**), as well as the periodic boundary condition, are applied. The periodic boundary condition in the y-direction serves to mimic an “infinite reservoir.” The relevant parameters are listed in **Table 3.1**.

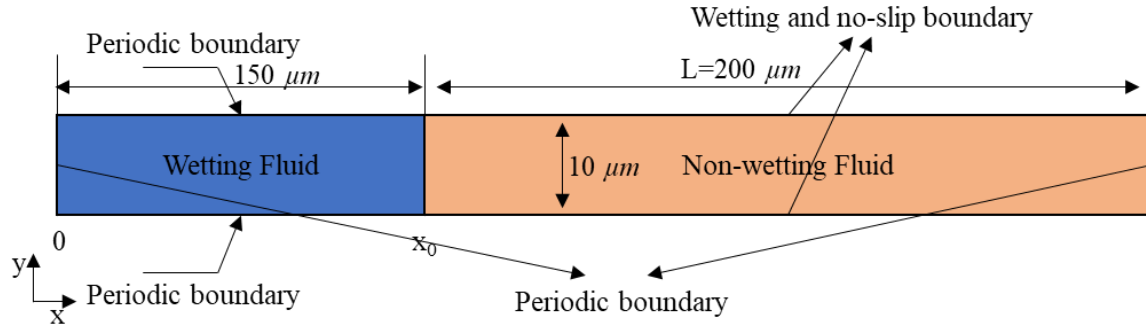


Figure 3.3. Schematic of the model setup for validation case #1.

Table 3.1. Parameters for validation case #1.

Parameters	Value
Wetting fluid density (kg/m ³)	1000
Wetting fluid viscosity (cP)	10
Non-wetting fluid density (kg/m ³)	1000
Non-wetting fluid viscosity (cP)	1
Diffusion Coefficient in liquid and gas phase (m ² /s)	10 ⁻⁴
Dimensionless Henry's constant	2
Contact angle	60°
Surface tension coefficient (N/m)	0.04

Assuming isothermal condition, incompressibility, and neglecting the contribution of the inertial and gravity effects, the analytical solution for the interface position as a function of time was proposed by Washburn and Lucas (1921):

$$\sigma \cos(\theta) = \frac{6}{r} [\mu_w x + \mu_n (L - x)] \frac{dx}{dt} \quad (3.25)$$

where r represents the distance from the center of the capillary tube; μ_w and μ_n are the viscosities of the wetting and non-wetting fluids, respectively. **Equation 3.25** can be written as an integral form:

$$\frac{\mu_w - \mu_n}{2} (x^2 - x_0^2) + \mu_n L(x - x_0) = \frac{r\sigma \cos(\theta)}{6} t \quad (3.26)$$

The analytical solutions are computed and plotted in MATLAB®. A comparison between the numerical model predictions and the analytical solution (**Equation 3.26**) is shown in **Figure 3.4**, and a good agreement is observed. Therefore, the implementation of a two-phase fluid flow solver is verified.

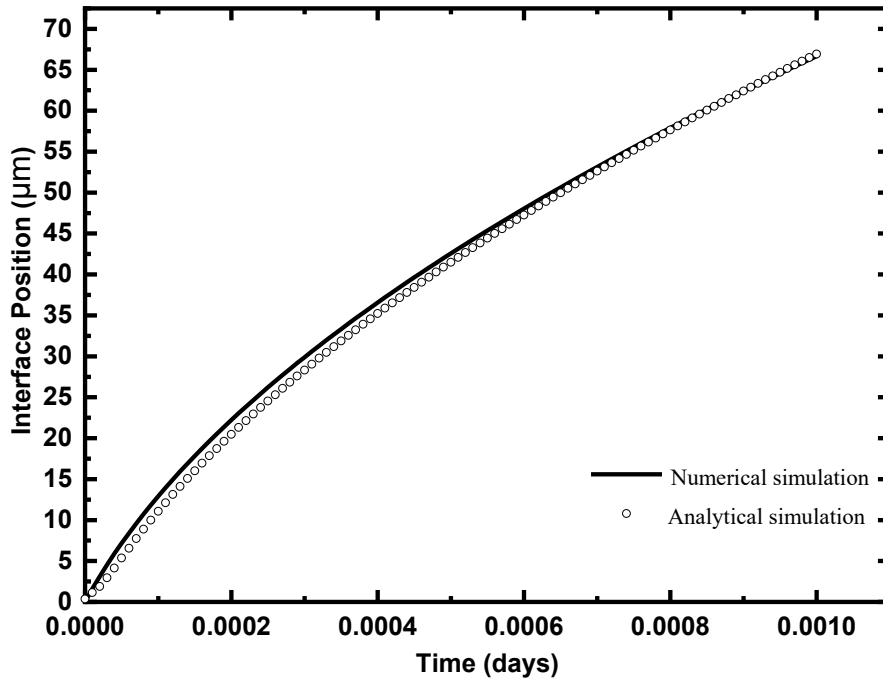


Figure 3.4. Interface position as a function of time for validation case #1.

3.4.2 Validation case #2 – Diffusion-only mass transfer

A diffusion-driven mass transfer case is presented here. Model results are compared against the analytical solution, and mesh sensitivity is also analyzed. A two-dimensional (2D) tube of dimensional $8 \text{ mm} \times 1 \text{ mm}$, as shown in **Figure 3.5**, is considered. Initially, the right half is filled with a liquid ($\phi = 1$), while the left half is filled with gas ($\phi = 0$); the gas phase contains a passive tracer (component i) with an initial concentration

$$C_i(x, 0) = \begin{cases} C_i^0 = C_0 \text{ mol/m}^3, & \phi = 0 \\ 0, & \phi = 1 \end{cases} .$$

Since both ends are open ($p = 0$) and the capillary

pressure is ignored, the total velocity remains zero. The relevant parameters are presented in **Table 3.2**. Five computational grids are generated to analyze the solution dependency on mesh size with the same mesh topology. **Figure 3.6** demonstrates the convergence of normalized concentration at a certain location versus the total number of elements. The final mesh size is selected so that additional improvement in accuracy is less than 1%. A non-uniform grid with triangular elements is used with the maximum element size of 0.0067 mm and the minimum element size of $2 \times 10^{-5} \text{ mm}$ of the selected mesh. The value of ε (interface thickness) is half of the maximum element size within the computational domain.

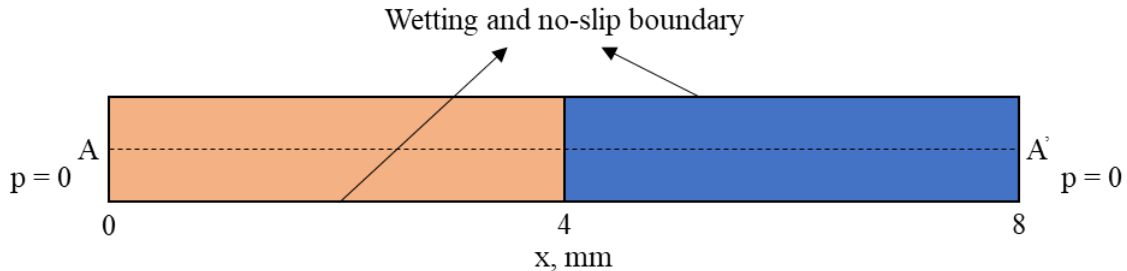


Figure 3.5. Schematic of the model setup for validation case #2.

Table 3.2. Parameters of validation case #2.

Parameters	Value
Liquid density (kg/m ³)	1000
Liquid viscosity (cP)	1
Gas density (kg/m ³)	1.29
Gas viscosity (cP)	0.0185
Diffusion coefficient in liquid and gas phases (m ² /s)	10 ⁻⁴
Dimensionless Henry's constant	2
Contact angle	90°
Surface tension (N/m)	0.07

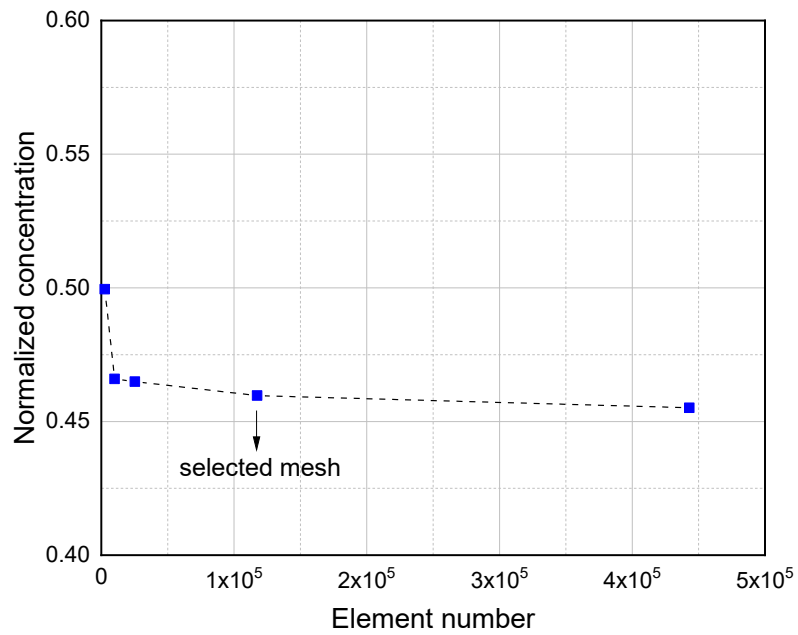


Figure 3.6. Mesh sensitivity analysis.

As for this diffusion-only case, the analytical solution for $C_i(x,t)$ is shown in the following equation (see **Appendix A** for derivation):

$$C_i(x,t) = \begin{cases} \frac{HC_i^0}{H+1} \operatorname{erf}\left(\frac{0.004-x}{2\sqrt{Dt}}\right) + \frac{C_i^0}{H+1}, & \phi = 0 \\ \frac{HC_i^0}{H+1} \operatorname{erf}\left(\frac{0.004-x}{2\sqrt{Dt}}\right) + \frac{H}{H+1}, & \phi = 1 \end{cases} \quad (3.27)$$

The normalized concentration (C_i / C_0) profiles along line AA' (see **Figure 3.5**) at different times are plotted in **Figure 3.7**. The simulated profiles are in excellent agreement with the analytical solutions.

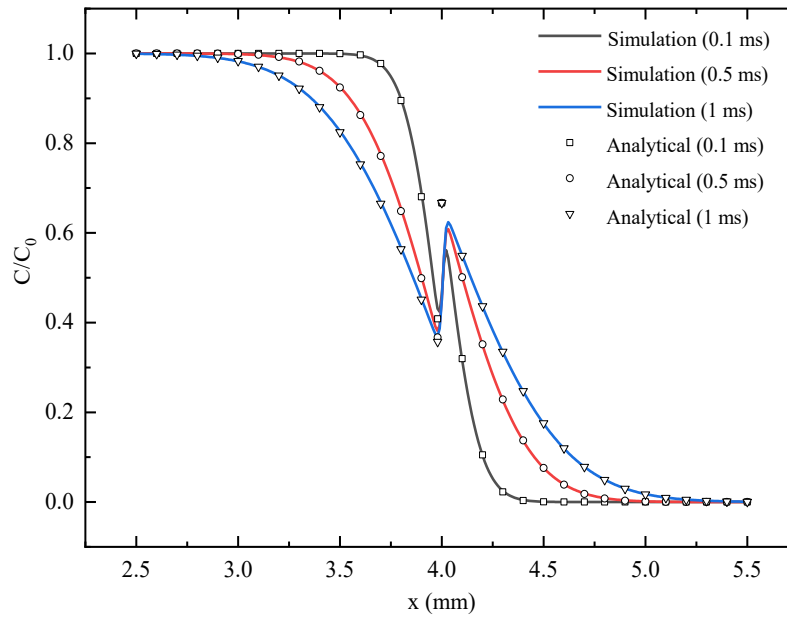


Figure 3.7. Normalized concentration profiles along line AA' at different times.

3.5 The Wettability Effects on the Waterflooding Process

In this section, a pore-scale simulation of the waterflooding process was simulated within the porous medium to investigate the effects on the immiscible displacement processes. Immiscible fluid-fluid displacement in porous medium is a fundamental process that happens in various engineering applications including but not limited to contaminant transport (Blunt et al., 1793; Menke et al., 2015; Haggerty and Gorelick, 1995), carbon capture and sequestration (Andrew et al., 2013; Krevor et al., 2015; Saraf and Bera, 2021), and enhanced oil recovery (Armstrong and Wildenschild, 2012). Our study focuses on the impact of wettability on fluid flow distribution and recovery efficiency during the immiscible displacement process. A two-dimensional pore-throat body geometry is designed to mimic the pore-throat features of the porous medium. The geometry of the porous medium with the dimension information is shown in **Figure 3.8**. In our simulation, the porous medium is initially filled with the oil phase (the density of the oil phase $\rho_o = 910 \text{ kg/m}^3$ and viscosity $\mu_o = 0.01 \text{ Pa}\cdot\text{s}$). Then, the water phase (the density of the water phase $\rho_w = 1000 \text{ kg/m}^3$ and viscosity $\mu_w = 0.001 \text{ Pa}\cdot\text{s}$) is injected from the inlet (left boundary) at a constant velocity with a value of 0.1 m/s . The outlet (right boundary) is set up with a zero-pressure boundary condition. The solid wall boundaries are wall conditions with a fixed contact angle, θ . The oil/water interfacial tension is 32 mN/m . The corresponding capillary number (defined as $Ca = \frac{\mu_w U}{\sigma}$) of 3.125×10^{-5} , which means a capillary-dominated displacement. To explore the impact of wettability effect on phase distribution and recovery efficiency, two different initial oil distribution cases are designed with three pairs of contact angles (**Figure 3.9**).

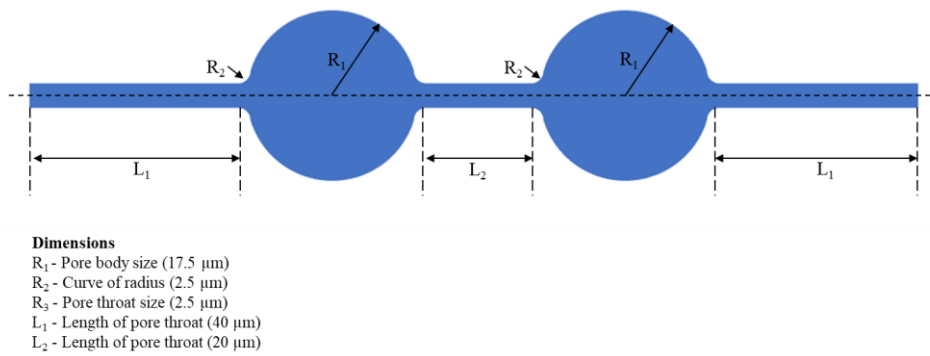


Figure 3.8. Schematic of the pore-throat body geometry

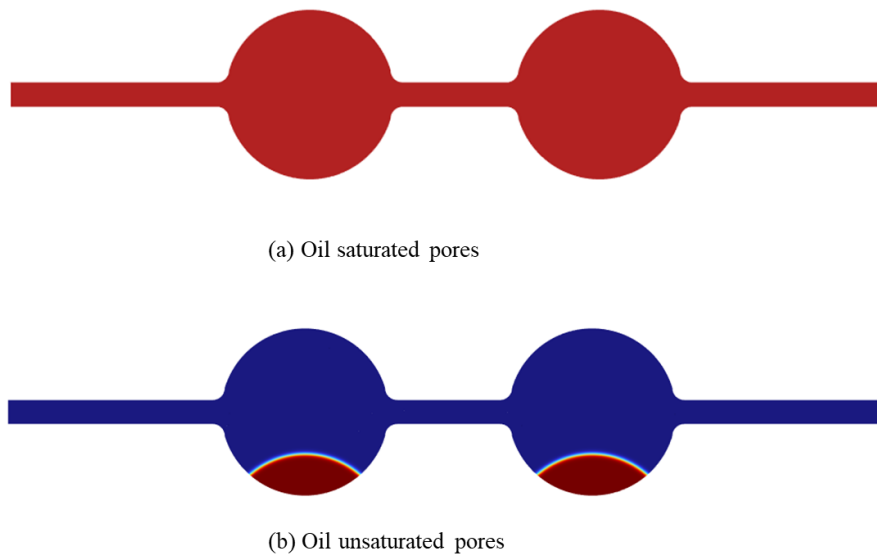


Figure 3.9. Initial oil saturation for two different cases. (a) The oil-saturated pores; (b) oil-unsaturated pores (red area – oil phase; blue area – water phase).

The results of the wettability cases presented were conducted using three different contact angles of 0, 90°, and 180°. The lowest energy equilibrium state between the solids and fluids is reached when the measured contact angle is equal to the equilibrium contact angle. Figure 3.10 shows the evolution of the phase distribution of the initial oil-saturated

pores case for the water-wet state. For the totally water-wet state ($\theta = 0$) case, the invading fluid (water phase) gradually occupied all the pores with the stable flow, resulting in a complete displacement after the water breakthrough. Figure 3.11 shows the evolution of the phase distribution for the totally oil-wet state ($\theta = 180^\circ$) case. It can be seen that the oil phase sticks onto the solid walls due to the strongly oil-wet condition, and the water phase is convex to the larger pores covered with a thin oil film formed. The water phase forms globules of varying sizes in the central part of the larger pores. The water phase has no direct contact with the solid walls. In this case, the water breakthrough time is relatively faster with a concave meniscus shape (residual oil phase).

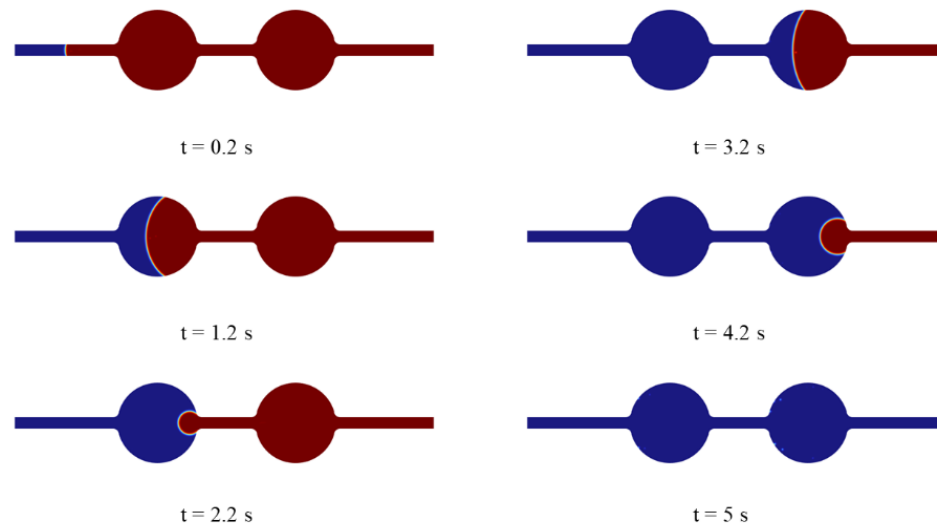


Figure 3.10. Evolution of the phase distribution for the water-wet state ($\theta = 0$) during the immiscible displacement in oil saturated pores (red area – oil phase; blue area – water phase).

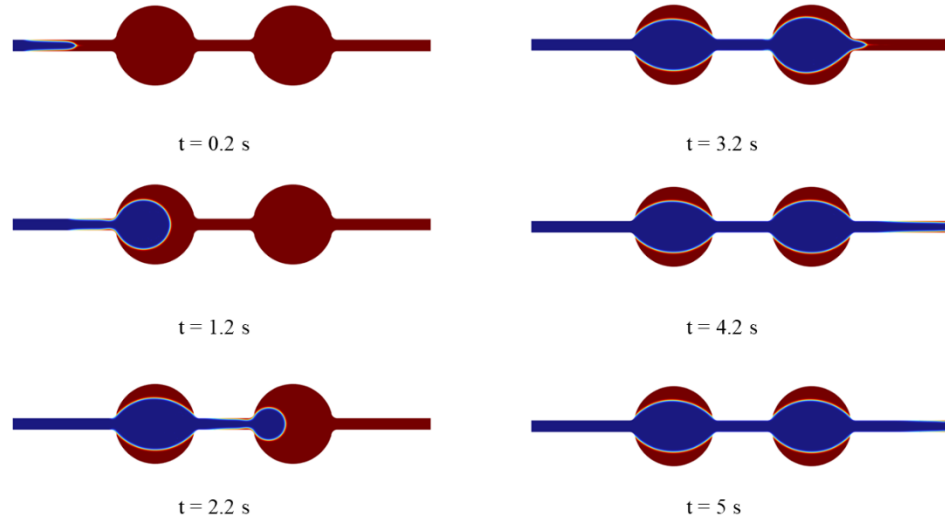


Figure 3.11. Evolution of the phase distribution for the oil-wet state ($\theta = 180^\circ$) during the immiscible displacement in oil-saturated pores (red area – oil phase; blue area – water phase)..

3.6 Summary

In this work, the conservative level-set equation, Navier-Stokes equation, continuity equation, and CST formulation are coupled to simulate vaporized solvent injection processes at the pore-scale level. Key mechanisms such as convection, diffusion, interphase mass transfer, and capillarity are incorporated. In detail, the capillary effect was accounted with the surface tension force term in Navier-Stokes equations and the wetting effect boundary conditions. The model is validated against several bulk fluid systems where analytical solutions can be derived. Then, we investigate the wettability effect on the immiscible displacement during the waterflooding process using the proposed pore-scale modeling. We designed a pore-throat body geometry to quantify the wettability effect by considering the contact angles in two different initial oil-distributed cases. The simulation results show that

wettability alteration is an effective way to enhance oil recovery, especially to change the wetting state of the rock to a more water-wet state.

CHAPTER 4 : NUMERICAL PORE-SCALE SIMULATION OF TWO-PHASE FLOW IMMISCIBLE DISPLACEMENT PROCESSES

4.1 Overview

The mathematical formulations and related pore-scale two-phase multi-component flow solver are described and validated in Chapter 3. In this chapter, several case studies are presented to illustrate the methods, and the relevant scale-up parameter results will be discussed. First, a drainage process is simulated in a two-dimensional capillary tube for both diffusion-dominated and convection-dominated processes. Simulation results of the dimensionless concentration distribution are shown. Unphysical oscillation issues are observed over a wider range of the computational domain for the convection-dominated process. To alleviate the numerical error near the interface and capture the interfacial concentration discontinuity, an artificial diffusion coefficient term is introduced to the interfacial mass transfer model. Next, the vaporized solvent injection in a natural sandstone porous medium study is presented, where results are scaled-up for computing the REV-based mass transfer coefficient based on the linear transfer model.

4.2 Application Case Studies

4.2.1 Application Case #1 - Vaporized Solvent Injection into a 2D Capillary Tube

This section presents two examples to illustrate how the proposed model can be employed to model a solvent injection process. First, a drainage process is simulated to study interphase mass transfer across a moving interface in a capillary tube. The model setup is shown in **Figure 4.1**. The capillary tube is initially filled with a liquid ($\phi = 1, C_i = 0$). At $t >$

0, gas ($\phi = 0$, $C_i = C_0 \text{ mol/m}^3$) is injected into the capillary tube from the left boundary at a constant velocity $U_0 = 0.04 \text{ m/s}$. At the tube outlet (right boundary), $p = 0 \text{ Pa}$. A no-slip boundary condition is implemented along the wall (top and bottom boundaries), while other key parameters are listed in **Table 3.1**. The normalized concentration profiles at different times are shown in **Figure 4.2**.

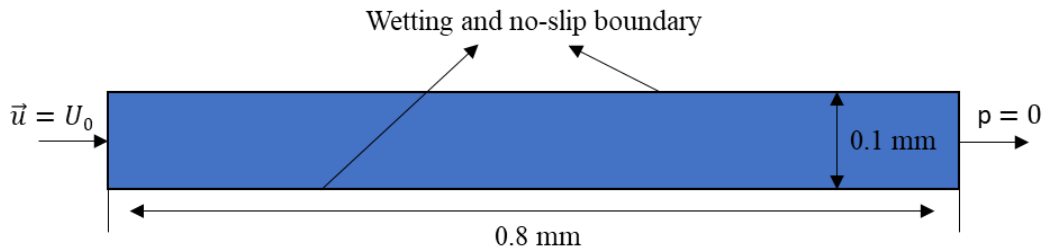


Figure 4.1. Schematic of the model setup for application case #1.

Table 4.1. Parameters for application case #1.

Parameters	Value
Liquid (water) density (kg/m^3)	1000
Liquid (water) viscosity @20 °C (cP)	1
Gas (Air) density (kg/m^3)	1
Gas (Air) viscosity @20 °C (cP)	$1.8 \cdot 10^{-2}$
Diffusion coefficient in liquid and gas phases (m^2/s)	10^{-6}
Dimensionless Henry's constant	2
Contact angle	45°
Surface tension (mN/m)	35

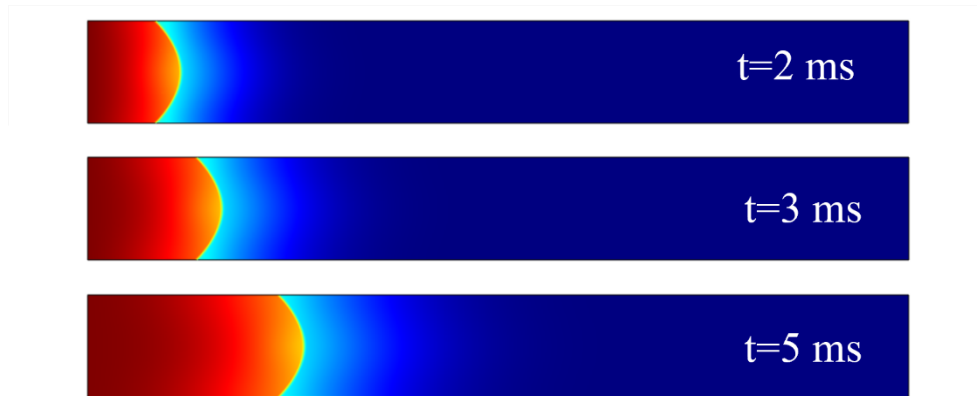


Figure 4.2. Simulated normalized concentration profiles at different times.

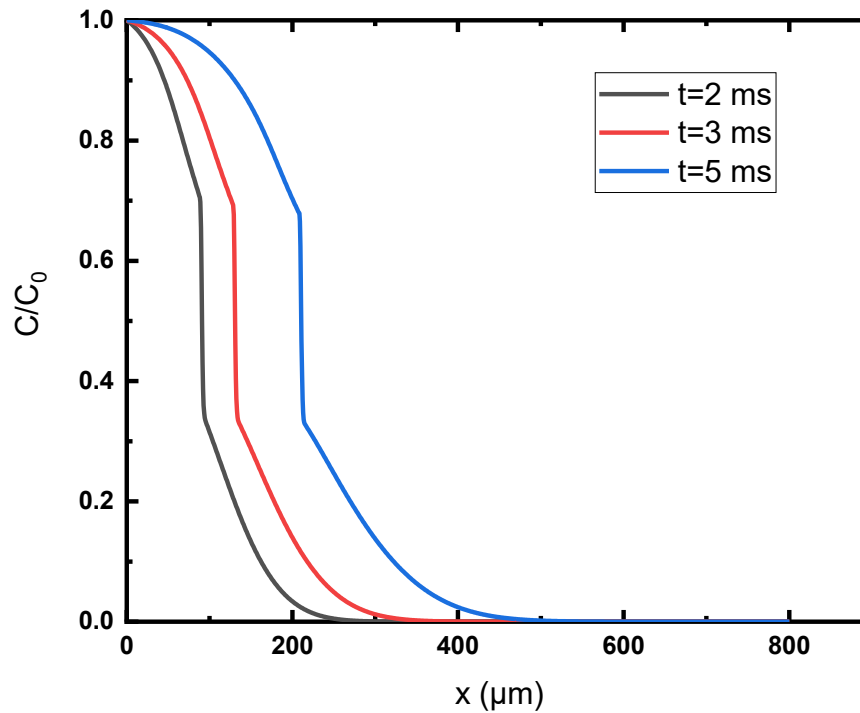


Figure 4.3. Normalized concentration profile along the capillary tube mid-plane at different times ($Pe = 2$) for application case #1.

It should be noted that numerical instability issues arise when the Péclet number, Pe , as defined by the following equation, exceeds unity (Beers, 2007; Deen, 1998):

$$Pe = \frac{\text{convective term}}{\text{diffusive term}} = \frac{U_0 L_{char}}{D} \quad (4-1)$$

where L_{char} is the characteristic length and is equal to the radius of the capillary tube. Figure 4.4 shows an example of $Pe = 200$, with the diffusion coefficient of $1 \times 10^{-8} \text{ m}^2/\text{s}$. The concentration profiles along the mid-plane of the capillary tube at different times are shown. Unphysical oscillations are observed over a wide region around/near the interface. They can result from truncation errors and inconsistencies associated with the advection operator between phases and species transport equation (Yang et al., 2016; Deising et al., 2016; Maes and Soulaine, 2018; Maes and Soulaine, 2020; Maes and Menke, 2021). To alleviate the numerical error near the interface and capture the interfacial concentration discontinuity, one approach is using an artificial compressive advective term or an anti-diffusive advection term in the volumetric phase-fraction transport equation to counteract the artificial mass transfer (Olsson and Kreiss, 2005; Weller, 2006; So et al., 2011). More recent works, including Maes and Soulaine (2018, 2020), apply the same advection operator to obtain a fully consistent advection scheme and avoid the artificial mass transfer at the interface with the algebraic VOF method. Another approach is adding an artificial diffusion; Yang et al. (2017) showed that the mesh density should be designed such that diffusion would dominate over advection locally ($Pe_{local} < 0.5$). Given that the LS method is used here, an artificial diffusion coefficient is used to reduce the numerical instabilities.

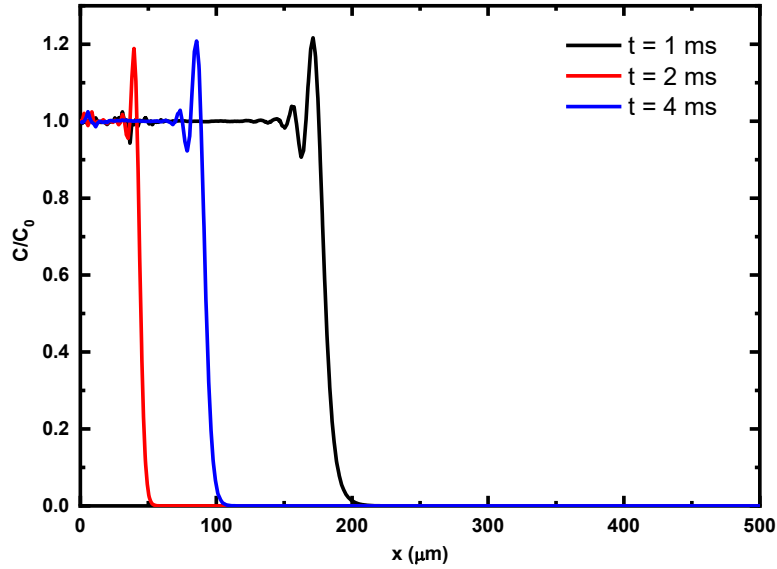


Figure 4.4. Normalized concentration profiles along the capillary tube mid-plane at different times ($Pe = 200$) for application case #1.

An artificial diffusion coefficient, D_{art} , defined as follows, is introduced for stability purposes (COMSOL, 2019):

$$D_{art} = \delta U_0 L_{char} \quad (4-2)$$

where δ is the tuning parameter. The artificial diffusion coefficient is added to the physical diffusion coefficient, D , giving an overall diffusion coefficient of $D + D_{art}$. Then, we have a corresponding element Péclet number:

$$Pe = \frac{U_0 L_{char}}{D + D_{art}} = \frac{U_0 L_{char}}{D + \delta U_0 L_{char}} \quad (4-3)$$

To ensure that the Peclet number does not exceed 1, a tuning parameter of $\delta = 1$ is needed. In this study, we find that a smaller value is often sufficient to stabilize the simulation.

Figure 4.4 shows the concentration profiles corresponding to $\delta = 1$. It is important to note

that the amount of artificial diffusion depends on the mesh size. One should consider the decrease in solution accuracy if a large artificial diffusion is added (e.g., over-smoothing the interface). It can affect the solution significantly. A finer mesh is associated with a smaller artificial diffusion and lower truncation error but a higher computational cost. Therefore, a reasonable mesh should be selected to balance between computational costs and model accuracy.

4.2.2 Application Case #2 – Vaporized Solvent Injection in a Natural Porous Medium

A more complex 2D porous medium derived from a thin slice of Berea sandstone (Keller et al., 1997) is considered. The domain size is $660 \mu\text{m} \times 320 \mu\text{m}$ (**Figure 4-5**). The vapor-extraction process under various flow conditions is simulated. The domain is initially filled with a liquid or oil ($\phi = 1$, $C_i = 0$). An injection zone saturated with the vaporized solvent is appended to the right boundary. At time zero, an initial gas-liquid interface is established. At $t > 0$, a vaporized solvent of propane ($\phi = 0$, $C_i = C_0 \text{ mol/m}^3$) is injected at the left boundary with a constant velocity $\vec{u} = U_x = 0.01 \text{ m/s}$. At the outlet (right boundary), $p = 0 \text{ Pa}$. A wetted wall boundary condition with a constant contact angle is applied on the surface of the grains. The average pore diameter, porosity, and permeability are approximately $30 \mu\text{m}$, 0.55 , and 1.66 mD . The computation domain is discretized with triangular elements. An adaptive mesh refinement technique is used to refine grids around the interface and pore throats (Amiri and Hamouda, 2014).



Figure 4.5. Schematic of the complex porous medium and related boundary conditions (white area – solid grains; grey area – pore space).

The domain is initially filled with the oil phase, which is displaced by the vaporized solvent. The other parameters used in this model are summarized in **Table 4.2**. The corresponding capillary number $Ca = \frac{\mu_{mv} U_0}{\sigma}$, defined as the ratio of viscous drag force to surface tension force (Beers, 2007 and Deen, 1998), is 4.3×10^{-3} .

Table 4.2. Parameters for application case #2.

Parameters	Value
Oil density, (kg/m ³)	789
Oil viscosity, (cP) @25 °C	23,000
Gas density, (kg/m ³)	1.808
Gas viscosity, (cP) @25 °C	0.015
Diffusion Coefficient in liquid and gas phase, (m ² /s)	6.8 x 10 ⁻¹⁰ (Yang and Gu, 1996)
Dimensionless Henry's constant	2 @ 25 °C
Contact angle	45°
Surface tension, (mN/m)	34.7

Solvent injection into a bitumen reservoir reduces viscosity significantly and improves oil recovery. Compared with the density of the vaporized solvent, the solvent-heavy oil density is considered constant here. The logarithmic mixing rule, as shown in **Equation 4.4** (Arrhenius, 1887), commonly used for modeling solvent-oil mixtures, is applied:

$$F_i = k_i a(\overline{C_{i,g}} - H * \overline{C_{i,l}}) \quad (4.4)$$

where x and μ are mole fraction and viscosity, respectively, the subscripts *mix*, *b*, and *s* refer to the mixture, bitumen, and solvent.

Figures 4.6 and **4.7** show the phase fraction and propane concentration at different times, respectively. The liquid phase viscosity decreases dramatically as the solvent is transported into the liquid phase, as shown in **Figure 4.8**.

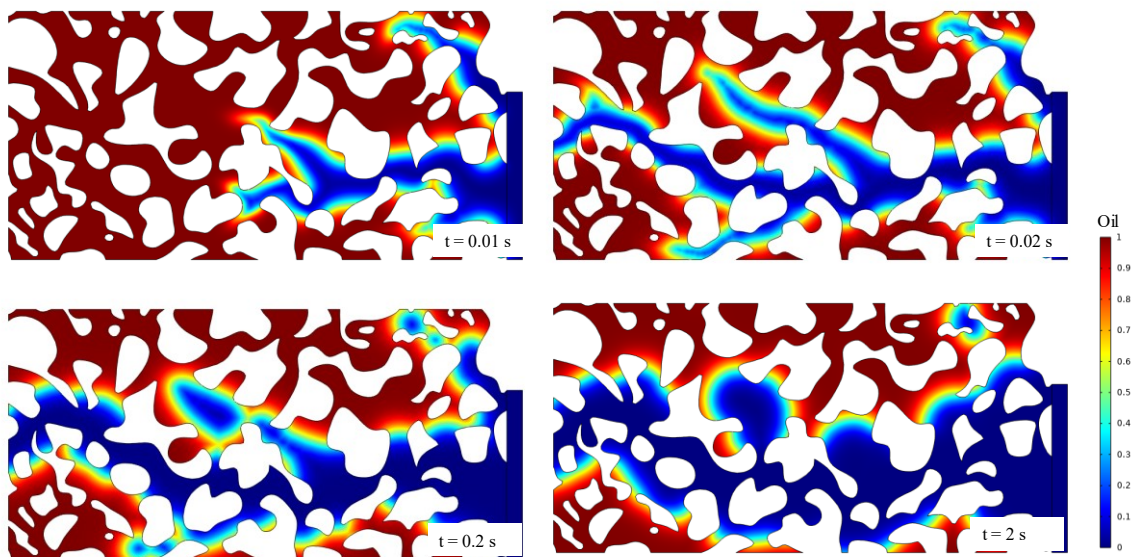


Figure 4.6. Phase fraction profiles at different times for application #2.

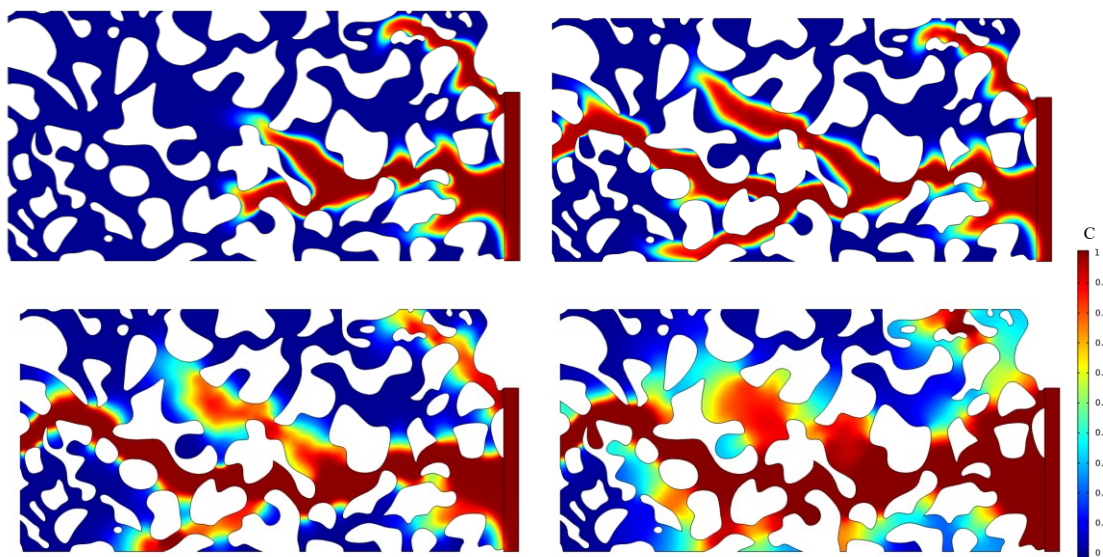


Figure 4.7. Propane concentration profiles at different times for application #2.

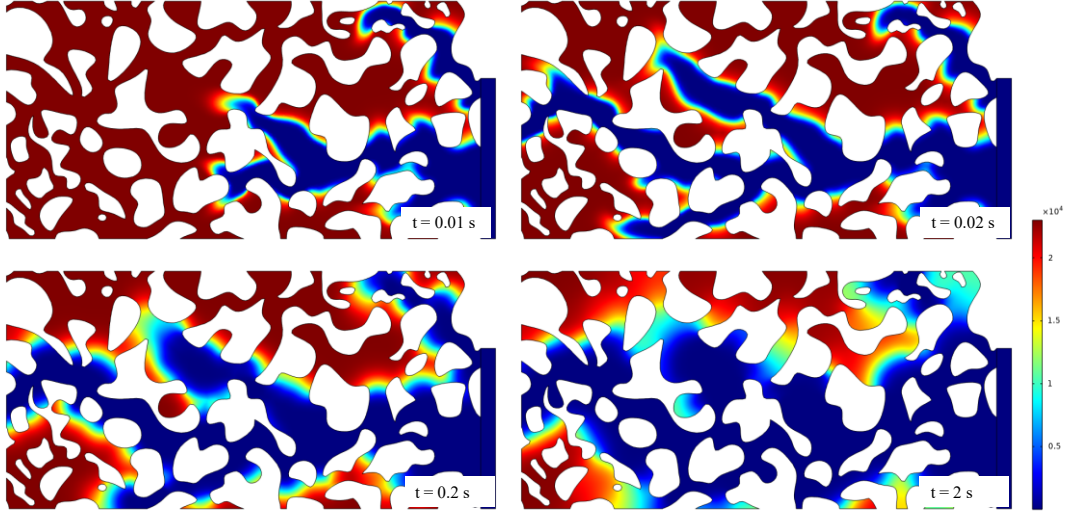


Figure 4.8. Liquid phase viscosity at different times for application #2.

In this section, the pore-scale simulation results are used to compute an effective macro-scale mass transfer coefficient k_i , representing the combined effect of the mass transfer due to dispersion, diffusion, and interfacial transport (Leung and Srinivasan, 2012). Considering the low molecular diffusion and pore-size heterogeneity in heavy oil, Maes and Soulaine (2018) noted that the linear transfer model would provide a more accurate prediction of k_i . Therefore, the linear transfer mode (Soulaine et al., 2011) is used to define k_i , relating the interfacial mass flux and the concentration difference:

$$F_i = k_i a (\overline{C_{i,g}} - H^* \overline{C_{i,l}}) \quad (32)$$

where F_i is the interfacial mass flux, k_i is the interfacial mass transfer coefficient, and a is the interfacial area, accounting for the variation in interfacial contact area due to the pore-scale heterogeneity. $\overline{C_{i,g}}$ and $\overline{C_{i,l}}$ represents the average normalized concentration of species i in the gas and liquid phases, respectively. The local average concentration of species in each phase and the mass transfer flux can be obtained directly from the pore-scale simulation.

Figure 4.9: plots F_i/a versus the concentration difference at a particular time. The late-time data are highlighted with a green circle (enlarged in **Figure 4.9 (b)**). It is noted that F_i/a does exhibit a linear relationship with the concentration difference after a certain period of time. From 0.17 s to 0.198 s, the slope of the trend line (i.e., k_i) is approximately 0.0001 m/s, while its value is reduced to 3.85×10^{-5} m/s from 0.198 s to 2 s. This procedure would yield a single value of k_i for a given pore-scale model. Suppose multiple realizations of the pore-scale models are simulated due to uncertainty in heterogeneity; a probability distribution of k_i , can be calibrated by assembling the results from those different realizations, and it represents the uncertainty due to heterogeneity in the scale-up of k_i (Leung and Srinivasan, 2011; Leung, 2014; Vishal and Leung, 2017; Andrianova and Leung, 2021).

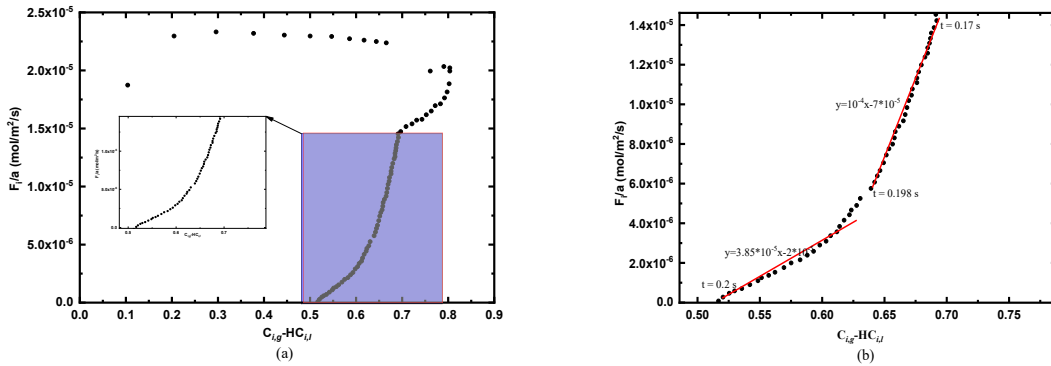


Figure 4.9. (a) Evolution of the mass flux per interfacial area as a function of concentration difference. (b) An enlarged view of late time data (orange circle) illustrates the linear relationship.

4.3 Summary

In this chapter, the conservative level-set equation, Navier-Stokes equation, continuity equation, and CST formulation are coupled to simulate vaporized solvent injection processes at the pore-scale level. Key mechanisms such as convection, diffusion, interphase mass transfer, and capillarity are incorporated. The numerical model is tested in several scenarios, including bulk fluid systems (e.g., capillary tube) and natural sandstone porous media. It is observed that numerical instability may result when simulating the displacement of a more viscous fluid by a less viscous fluid (e.g., non-condensing or vaporized solvent injection process). The problem can be rectified by introducing an artificial diffusion term as a function of the mesh size.

The scale-up analysis also provides insights into using the pore-scale simulation results for computing an effective macro-scale mass transfer coefficient. Depending on the size of the pore-scale model, this macro-scale can be considered the Darcy scale. The mass transfer coefficient is estimated from the slope of the late-time data, where a linear relationship between interfacial flux and concentration difference is inferred based on a linear transfer model. Lastly, this macro-scale mass transfer coefficient is sensitive to pore-scale heterogeneity, interfacial contact areas, and flow velocity. The results illustrate that the interfacial mass transfer can be captured when modeling Darcy-scale or field-scale flow properties for solvent-based oil recovery processes.

CHAPTER 5 : A CONSISTENT INTERPHASE MASS TRANSFER METHOD AND LEVEL-SET FORMULATION FOR INCOMPRESSIBLE TWO-PHASE FLOWS

5.1 Overview

Characterizing the interphase mass transfer phenomena in a porous medium is essential for many engineering applications. The pore-scale modeling approaches offer a potential for handling the interface mass transfer in detail and provide some fundamental understanding of macro-scale modeling. However, the traditional interphase methods (e.g., continuous species transfer method) suffer numerical instability issues, especially for convection-dominated cases (Péclet number or $Pe > 1$). In this chapter, we propose a consistent interphase mass transfer method by adding a compressive term to a conservative Level Set Continuous Species Transfer (LS-CST) model presented in our previous work in Chapter 3 (Yu and Leung, 2023). The new model (LS-CCST) is suitable for a wider range of Péclet numbers. First, the LS-CCST model is validated using various specific cases where the analytical solution exists. Compared with the standard LS-CST method, the LS-CCST method accurately captures the interfacial concentration discontinuity for convection-dominated and significantly reduces the numerical instabilities. Then, the proposed model is used to simulate the interphase mass transfer of a two-phase immiscible displacement process in a single cavity. The simulation results show that the average velocity within the trapped phase zone has a linear relationship with the natural logarithm of the viscosity ratio, and the results are used for estimating an upscaled (effective) mass transfer coefficient. A positive correlation between the viscosity ratio and the effective mass transfer coefficient can be observed. Indeed, a constant effective mass transfer coefficient is achieved after a certain

travel time under various flow conditions. Additional mixing in the trapped phase from the recirculation inside the dead-end pores, especially for high-viscosity fluid pairs, is observed.

5.2 Mathematic Formulation

This section introduces a novel interface mass transfer model, LS-CST, to simulate the two-phase multicomponent transport system at the pore scale. First, a single-field formulation of Navier-Stokes equations coupled with the level-set method is formulated to solve the time evolution of the pressure, velocity, and phase fraction distributions. Then, a new compressive multiphase species transport (LS-CCST), entirely consistent with the conservative LS method, is derived.

The following assumptions and simplifications are made to construct the governing equations to model the two-phase multicomponent transport process: (1) Under the isothermal condition, the two fluids are assumed to be Newtonian and incompressible. (2) Two immiscible phases (gaseous and liquid) are modeled. (3) The species can diffuse to/from the interface following Fick's law, and Henry's law defines the concentration distribution at the gas-liquid interface under thermodynamic equilibrium. (4) The surface tension coefficient is constant and uniform at the interface. (5) No phase changes. (6) Only one solute species is modeled. (7) No chemical reactions are considered.

5.2.1 Hydrodynamics – Level-Set Method

In the standard level-set equation, a smooth signed distance function denoted as f_{LS} is introduced into the multiphase flow system to capture the interface movement (Osher and Sethian, 1988):

$$|f_{LS}(\vec{x})| = d(\vec{x}) = \min_{x_I \in I} (|\vec{x} - \vec{x}_I|) \quad (5.1)$$

where I is the interface, \vec{x} is the position vector, and $d(\vec{x})$ is a distance measure; if $f_{LS}(\vec{x}) > 0$, the cell occupies one side of the interface; if $f_{LS}(\vec{x}) < 0$, the cell occupies the other side of the interface; and the free interface is represented by the set of points where $f_{LS}(\vec{x}) = 0$. The standard LS advection equation is given by:

$$\frac{\partial f_{LS}}{\partial t} + \nabla(\vec{u} f_{LS}) = 0 \quad (5.2)$$

The interface velocity is typically treated as the normal velocity of the LS function, which is computed using the gradient of the LS function. However, the gradient of the LS function would become too small on the interface (e.g., the zero level-set), which results in the level-set function not exactly equal to the signed distance function (Sussman et al., 1999; Sussman and Puckett, 2000; Khenner et al., 2001; Hartmann et al., 2010). A process called reinitialization is applied to alleviate numerical deterioration and enhance numerical stability at the interface; it entails re-initializing the LS function corresponding to the signed distance function to keep $|\nabla\phi| = 1$ (Sussman and Puckett, 2000; Khenner et al., 2001; Hartmann et al., 2010). Here, an iteration method proposed by Sussman et al. (1994) is used, where the level-set function f_{LS} is re-initialized by solving the Eikonal equation as an evolution equation to a steady state that satisfies the signed distance property $|\nabla\phi| = 1$ in each time step (Sussman et al., 1994; Sussman and Puckett, 2000).

$$\frac{\partial f_{LS}}{\partial t} = S(f_{LS,0})(1 - |\nabla f_{LS}|), \quad (t \rightarrow \infty) \quad (5.3)$$

where $S(f_{LS,0})$ is a smoothed sign function that goes to 0 at the interface (i.e., $S(f_{LS,0} = 0) = 0$),

$$S(f_{LS,0}) = \frac{f_{LS,0}}{\sqrt{f_{LS,0}^2 + \varepsilon^2}} \quad (5.4)$$

ε is a smoothing parameter that usually equals half the smeared-out interface thickness. The principal drawback of the classic LS is that it inherently does not meet mass conservation. Therefore, Olsson and Kreiss (2005) and Olsson et al. (2007) proposed a conservative LS method by introducing a smeared-out Heaviside function, H_{sm} , to replace the signed distance function.

$$\phi = H_{sm}(f_{LS}(\bar{x})) = \begin{cases} 0 & f_{LS}(\bar{x}) < -\varepsilon \\ \frac{1}{2} \left(1 + \frac{f_{LS}(\bar{x})}{\varepsilon} + \frac{1}{\pi} \sin\left(\frac{\pi f_{LS}(\bar{x})}{\varepsilon}\right) \right) & -\varepsilon \leq f_{LS}(\bar{x}) \leq \varepsilon \\ 1 & f_{LS}(\bar{x}) > \varepsilon \end{cases} \quad (5.5)$$

After computing ϕ Equation 5.5, the volume fraction varies from 0 to 1, and the interface is located by the contour where the value equals 0.5. In the end, we have a conservative LS equation introduced by Olsson and Kreiss (2005) and Olsson et al. (2007).

$$\frac{\partial \phi}{\partial t} + \vec{u} \cdot \nabla \phi = \gamma \nabla \cdot \left(\varepsilon \nabla \phi - \phi(1-\phi) \frac{\nabla \phi}{|\nabla \phi|} \right) \quad (5.6)$$

where ε is the same parameter in **Equation 5.4**, and γ is the reinitialization parameter, generally considered the maximum expected local velocity magnitude.

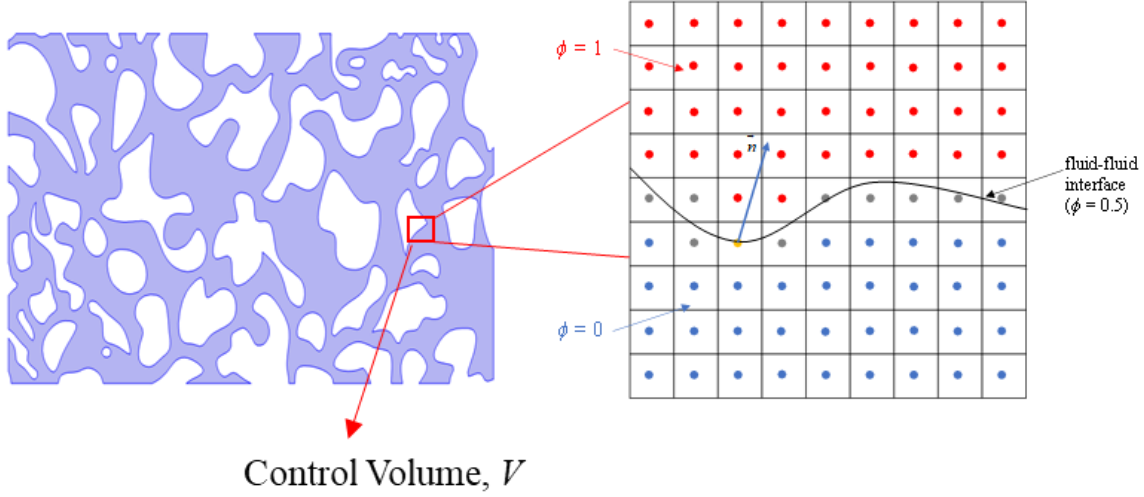


Figure 5.1. Representation of the level-set method of the gas-liquid interface.

Under the isothermal condition, the pressure and velocity field satisfy a single-field formulation of Navier-Stokes equations. The governing equations for momentum and mass balance are:

$$\rho \frac{\partial \bar{u}}{\partial t} + \rho \bar{u} \cdot \nabla \bar{u} = -\nabla p + \nabla \cdot \bar{\tau} + \bar{F}_{st} + \rho \bar{g} \quad (5.7)$$

$$\nabla \cdot \bar{u} = 0 \quad (5.8)$$

where \bar{u} is the velocity field, $\bar{\tau} = \mu(\nabla \bar{u} + \nabla \bar{u}^T)$ is the stress tensor. In the single-filed formulation, the fluid density and viscosity, which are considered mixture quantities, are defined as weighted averages using the smoothed LS function, ϕ (e.g., two-phase flow:

$\phi_1 = 1 - \phi_2$) with the p -phase ($p = 1, 2$):

$$\begin{aligned} \rho &= \rho_1 \phi_1 + \rho_2 \phi_2 \\ \mu &= \mu_1 \phi_1 + \mu_2 \phi_2 \end{aligned} \quad (5.9)$$

F_{st} is the surface tension evaluated numerically as a volume force with the continuum surface force (CSF) model (Brackbill et al., 1992).

$$F_{st} = (-\sigma\kappa\vec{n})\nabla\phi \quad (5.10)$$

where σ is the surface tension coefficient, the interface normal vector \vec{n} , and the interfacial curvature κ are determined in terms of the LS function:

$$\vec{n} = \frac{\nabla\phi}{|\nabla\phi|} \Big|_{\phi=0.5} \quad (5.11)$$

$$\kappa = -\nabla \cdot \vec{n} \quad (5.12)$$

A wetted wall boundary condition is imposed on the surface of each solid grain for the LS equation, and the contact angle for the wetting phase θ is set to a constant value. The no-slip boundary condition is also applied on the surface of each solid grain for the Navier-Stokes equation.

$$\vec{n}_{wall} \cdot (\varepsilon_{ls} \nabla\phi - \phi(1-\phi) \frac{\nabla\phi}{|\nabla\phi|}) = 0 \quad (5.13)$$

$$\vec{n} = 0 \quad (5.14)$$

where ε_{ls} represents the interphase thickness and is defined as half of the maximum element size for numerical stability.

5.2.2 Mass Transfer Model

The mass transfer model is used to solve the transport equation of a dissolved solute. It is coupled with the Navier-Stokes and LS equations in section 5.2.1. There is a discontinuity in concentration across the phase interface. Haroun et al. (2010) proposed a single-field formulation that introduced an additional "discontinuity term, Φ ," referring to the Continuous Species Transfer method (CST) within the framework of the VOF, which only takes nonzero value at the interface zone.

$$\frac{\partial C_i}{\partial t} + \underbrace{\nabla \cdot (\vec{u} C_i)}_{\text{convection}} = \underbrace{\nabla \cdot (D_i \nabla C_i)}_{\text{diffusion}} + \underbrace{\nabla \Phi_i}_{\text{discontinuity}} \quad (5.14)$$

where

$$\Phi = -\frac{C_i(1-H)}{\phi + H(1-\phi)} \nabla \phi \quad (5.15)$$

The classic volume of fluid equation is given by

$$\frac{\partial \alpha}{\partial t} + \nabla \cdot (\vec{v} \alpha) = \nabla \cdot (\alpha(1-\alpha) \vec{v}_r) \quad (5.16)$$

where \vec{v}_r is the relative velocity between the two phases ($\vec{v}_r = \vec{v}^2 - \vec{v}^1$). For the traditional/classic CST method, the phase relative velocity is assumed to be zero under the adopted mixture model (Marschall et al., 2012; Deising et al., 2016; Maes and Soulaine, 2018), causing the third term in **Equation 5.16** to vanish and missing of a compressive term in the LHS of **Equation 5.14**. On the other hand, numerical instability issues arise when the Péclet number, Pe , as defined by the ratio of the convection term to the diffusive term, exceeds unity (Beers, 2007; Deen, 1998):

$$Pe = \frac{\text{Convective term}}{\text{Diffusive term}} = \frac{U_o L_{char}}{D} \quad (5.17)$$

where L_{char} and U_o are the characteristic length and velocity; D is the diffusion coefficient.

As discussed in Section 5.1, Yang et al. (2017) stated that the condition of local $Pe < 0.5$ is needed to avoid numerical instability and accurately capture the interface concentration jump for a grid size of Δx .

$$Pe_{local} = \frac{U_o \Delta x}{D} \quad (5.18)$$

Following the above discussion on the classic CST method, we revisited the conservative level-set function (**Equation 5.6**) and have the governing equation describing

the fluid mass conservation equation with the phase volume fraction for each phase ($p = 1, 2$), respectively.

$$\begin{aligned}\frac{\partial \phi_1}{\partial t} + \bar{u} \cdot \nabla \phi_1 &= \gamma \nabla \cdot \left(\varepsilon \nabla \phi_1 - \phi_1 (1 - \phi_1) \frac{\nabla \phi_1}{|\nabla \phi_1|} \right) \\ \frac{\partial \phi_2}{\partial t} + \bar{u} \cdot \nabla \phi_2 &= \gamma \nabla \cdot \left(\varepsilon \nabla \phi_2 - (1 - \phi_2) \phi_2 \frac{\nabla \phi_2}{|\nabla \phi_2|} \right)\end{aligned}\quad (5.19)$$

Here, for a two-phase flow system, we have

$$\phi_1 + \phi_2 = 1, \text{ and } \frac{\nabla \phi_1}{|\nabla \phi_1|} = - \frac{\nabla \phi_2}{|\nabla \phi_2|}.\quad (5.20)$$

After substituting **Equation 5.20** into **Equation 5.19**, we obtain:

$$\begin{aligned}\frac{\partial \phi_1}{\partial t} + \nabla \cdot (\bar{u} \phi_1 - \gamma (\varepsilon \nabla \phi_1 - \phi_1 \phi_2 \frac{\nabla \phi_1}{|\nabla \phi_1|})) &= 0 \\ \frac{\partial \phi_2}{\partial t} + \nabla \cdot (\bar{u} \phi_2 - \gamma (\varepsilon \nabla \phi_2 + \phi_1 \phi_2 \frac{\nabla \phi_1}{|\nabla \phi_1|})) &= 0\end{aligned}\quad (5.21)$$

Thus, the total volumetric flux F_1, F_2 for each phase can be expressed as:

$$\begin{aligned}F_1 &= \bar{u} \phi_1 - \gamma (\varepsilon \nabla \phi_1 - \phi_1 \phi_2 \frac{\nabla \phi_1}{|\nabla \phi_1|}) \\ F_2 &= \bar{u} \phi_2 - \gamma (\varepsilon \nabla \phi_2 + \phi_1 \phi_2 \frac{\nabla \phi_1}{|\nabla \phi_1|})\end{aligned}\quad (5.22)$$

Hence, for the concentration of species i in each phase p (e.g., $c_{i,1}, c_{i,2}$), the species mass conservation equation in each phase p writes:

$$\frac{\partial \phi_p c_{i,p}}{\partial t} + \nabla \cdot (F_p c_{i,p}) = 0 \quad (p = 1, 2)\quad (5.23)$$

The transport equation is rewritten in terms of the global concentration of species i in the single-field formulation. The global concentration, C_i , is defined as:

$$C_i = c_{i,1} \phi_1 + c_{i,2} \phi_2\quad (5.24)$$

Adding the concentration of species i in both phases from **Equation 5.23** would give:

$$\frac{\partial(\phi_1 c_{i,1} + \phi_2 c_{i,2})}{\partial t} + \nabla \cdot (F_1 c_{i,1} + F_2 c_{i,2}) = 0 \quad (5.25)$$

Substituting **Equations 5.22** and **5.24** into **Equation 5.25**, we can have a single-field transport equation in terms of C_i .

$$\frac{\partial C_i}{\partial t} + \nabla \cdot (\vec{u} C_i) = \nabla \cdot (\gamma \varepsilon \nabla \phi_1 (c_{i,1} - c_{i,2}) - \gamma \phi_1 \phi_2 (c_{i,1} - c_{i,2}) \frac{\nabla \phi_1}{|\nabla \phi_1|}) \quad (5.26)$$

The local concentration difference of species i can be derived based on the interfacial boundary conditions and the definition of the global concentration (Haroun et al., 2010). Additional details of the CST method derivations can be found in Haroun et al. (2010) and Yu and Leung (2023).

$$c_{i,1} - c_{i,2} = \frac{(1-H)}{\phi + H(1-\phi)} C_i \quad (5.27)$$

Equation 5.26 describes the transport of species due to velocities. The complete transport equation should also include molecular diffusion and discontinuity terms, as noted in **Equation 5.14**. Therefore, substituting **Equation 5.27** into **Equation 5.26** and adding the molecular diffusion and discontinuity terms, a single-field governing equation, referred to as the LS-C-CST method, is shown in **Equation 5.28**.

$$\begin{aligned} \underbrace{\frac{\partial C_i}{\partial t}}_{\text{accumulation}} + \underbrace{\nabla \cdot (\vec{u} C_i)}_{\text{convection}} = \underbrace{\nabla \cdot (D \nabla C_i)}_{\text{diffusion}} \dots \\ - \underbrace{\nabla \cdot \left(D \frac{C_i(1-H)}{\phi + H(1-\phi)} \nabla \phi_1 \right)}_{\text{discontinuity}} + \underbrace{\gamma \nabla \cdot \left(\left(\frac{C_i(1-H)}{\phi + H(1-\phi)} \right) \left(\varepsilon \nabla \phi - \phi(1-\phi) \frac{\nabla \phi}{|\nabla \phi|} \right) \right)}_{\text{diffusion flux} \quad \text{compression flux}} \end{aligned} \quad (5.28)$$

The effective diffusion coefficient, D , can be expressed as a harmonic mean mixture diffusion coefficient.

$$D = \frac{D_{i,1}D_{i,2}}{\phi_1 D_{i,2} + \phi_2 D_{i,1}} \quad (5.29)$$

Here, the local concentration of species i in each phase, C_i , has a zero-mass flux condition $\vec{n}_s \cdot \nabla c_{i,p} = 0$ ($p = 1,2$). However, it does not mean the global concentration of species i has a zero-flux condition on solid walls. Graveleau et al. (2017) derived a proper boundary condition for the global concentration C_i at the solid walls.

$$\vec{n}_s \cdot \nabla C_i = \vec{n}_s \cdot \frac{(1-H)}{\phi + H(1-\phi)} \vec{C}_i \nabla \phi \quad (5.30)$$

5.3 Discretization Schemes

The proposed framework is implemented in a commercial finite-element-based solver COMSOL Multiphysics 6.0 (2021). The spatial discretization is performed with the limited linear differencing scheme. The implicit backward differentiation formula (BDF) solver is selected for the time stepping for its stability (Söderlind and Wang, 2006). The sets of the governing partial differential equations are solved by the COMSOL linear system solver – Parallel Direct Sparse Solver (PARDISO) (Schenk and Gärtner, 2004). The adaptive time-stepping scheme adjusts the timestep size automatically to maintain the desired relative tolerance. The convergence criteria are based on the weighted Euclidean normal of the solution-based estimated relative error. The mesh size is refined according to the complexity of the geometry and interface thickness. Test cases are run to ensure that the results are grid-size convergence.

5.4 Validation, Results, and Discussion

In this section, we first discuss the validity of the proposed hydrodynamic solver by comparing the simulation results with the analytical solution. We further evaluate the performance of the coupled hydrodynamic and mass transfer solver. A simple case is designed to compare simulation results against the analytical solution. Compared with the results of the standard CST method, the LS-C-CST method successfully captured the concentration jump and reduced the numerical instabilities around the interface. Finally, a single cavity model is constructed to investigate the flow behavior in a dead-end pore. The effect of the viscosity ratio on phase trapping is studied, and the simulation results are then used to estimate/upscale the effective mass transfer coefficient at the representative elementary volume (REV) scale.

5.4.1 Hydrodynamic Solver Validation – Co-Current Two-Phase Flow

The first validation case is to evaluate the performance of the proposed hydrodynamics solver (section 5.2.1 only, without the mass transfer model). This model simulates the immiscible two-phase layered flow between two infinite parallel plates, and the simulation results are compared with the analytical solutions. As illustrated in **Figure 5.2**, a two-dimensional (2D) domain with a height (h) of 0.2 mm is considered here. Initially, a wetting phase, i.e., phase 1, flows along the solid walls while the non-wetting phase, i.e., phase 2, flows in the center of the channel. The no-slip boundary condition is imposed on the solid wall. The periodic boundary condition is applied in the x-direction to mimic "infinite parallel plates" ($x = 0$ and $x = L$). Both fluids have the same density of 1000 kg/m^3 . The viscosity of the wetting phase (phase 1) is constant = $0.001 \text{ Pa}\cdot\text{s}$, and two viscosity ratios (

$M = \mu_{mw} / \mu_w$) 0.2 and 5 are tested. Assuming the flow in the channel is Poiseuille-type, the analytical solution for the velocity in the y-direction $u(y)$ can be obtained (Yiotis et al., 2007).

$$u(y) = \begin{cases} \frac{3h^2 \cdot \nabla p}{8\mu_w} + \frac{\nabla p}{2\mu_{mw}} \left(\frac{h^2}{4} - y^2\right) & 0 \leq y \leq 0.1 \text{ (mm)} \\ \frac{\nabla p}{2\mu_w} (h^2 - y^2) & 0.1 \leq y \leq 0.2 \text{ (mm)} \end{cases} \quad (5.31)$$

where the ∇p is the pressure gradient along the flow direction (x-direction here).

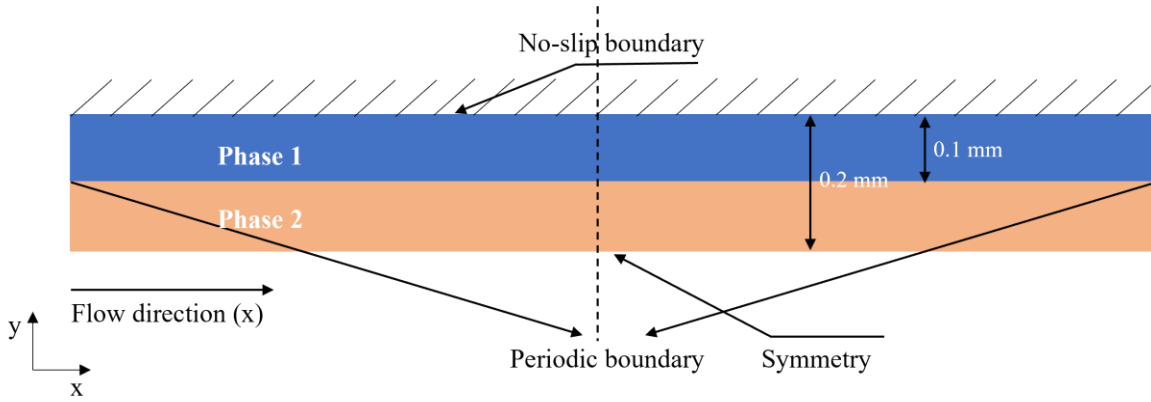


Figure 5.2. Schematic of the layered co-current two-phase flow in a horizontal channel.

The simulation is carried out until a steady state is achieved (i.e., where the velocity is no longer changing with the flow direction). As shown in **Figure 5.3**, the simulation results of the velocity distribution along the y-direction in the middle of the channel ($x = L/2$) are in good agreement with the analytical solution.

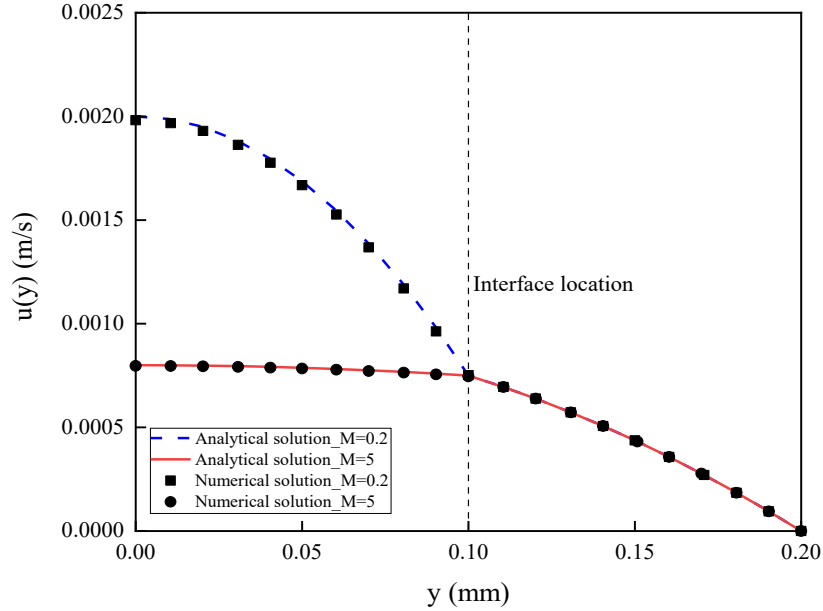


Figure 5.3. The velocity distribution in the y -direction at $x = L/2$ for different viscosity ratios.

5.4.2 Coupled Hydrodynamic and Mass Transfer Solver Validation – Two-Phase Displacement

This section aims to test the validity of the fully-coupled model presented in section 5.2.2. Instability is observed over a wider region near/around the interface when the local Péclet number exceeds 0.5 when using the classic CST method (Yang et al., 2017; Maes and Soullaine, 2018, 2020; Gao et al., 2021). Our previous work, Yu and Leung (2023), which adopted an LS-CST approach, also reported this instability issue, and an artificial diffusion was added to reduce the fluctuations around the interface. In this section, the new LS-C-CST formulation is tested for cases with $Pe_{local} > 0.5$ to examine the accuracy of interfacial mass transfer compared to the previous model.

We consider a one-dimensional (1D) capillary channel with a length of 0.2 mm. Initially, a portion domain ($0 < x < 0.02$ mm) is filled with phase 1 ($\phi = 1$), while the other domain ($0.02 < x < 0.2$ mm) is filled with phase 2 ($\phi = 0$). Phase 1 contains a passive tracer (component i) with an initial concentration of 1 mol/m^3 and 0.5 mol/m^3 in phase 2. Phase 1 ($c_{i,1} = 1 \text{ mol/m}^3$) is injected into the capillary channel from the left boundary at constant velocity ($U_o = 0.05 \text{ m/s}$), with the right boundary as an outlet with constant pressure $P = 0$. Since the dimensionless Henry's constant equals 0.5, the distribution of component i in both phases is in equilibrium initially. Thus, the analytical solution for $c_{i,p}$ ($p = 1, 2$) can be

expressed as $C_{i,p}(x, t) = \begin{cases} 1, & 0 \leq x \leq 20 + U_o t \text{ } (\mu\text{m}) \\ 0.5, & x \geq 20 + U_o t \text{ } (\mu\text{m}) \end{cases}$. We can see that the interface is advancing

along the capillary channel at a constant velocity over a wide range of the Pe_{local} , which is varied by changing D (10^{-6} , 10^{-8} , and $10^{-10} \text{ m}^2/\text{s}$), corresponding to local Péclet numbers ranging from 0.005, 0.5 to 50. The maximum element size of the domain is $1 \times 10^{-7} \text{ m}$.

Figure 5.4 shows the concentration profile at different times for different Pe_{local} numbers using the LS-C-CST and LS-CST approaches and compared with the analytical solutions. As shown in **Figure 5.4(b)**, the LS-C-CST-based simulation results are in much better agreement with analytical solutions. No instability or unphysical concentration fluctuations are detected, particularly near the interface or front. In contrast, we can see significant unphysical fluctuations around/near the interface, especially for $Pe_{\text{local}} = 50$ in **Figure 5.4(a)**. This indicates that the proposed LS-C-CST method could achieve the optimum result in capturing the interfacial concentration discontinuity for $Pe_{\text{local}} > 0.5$.

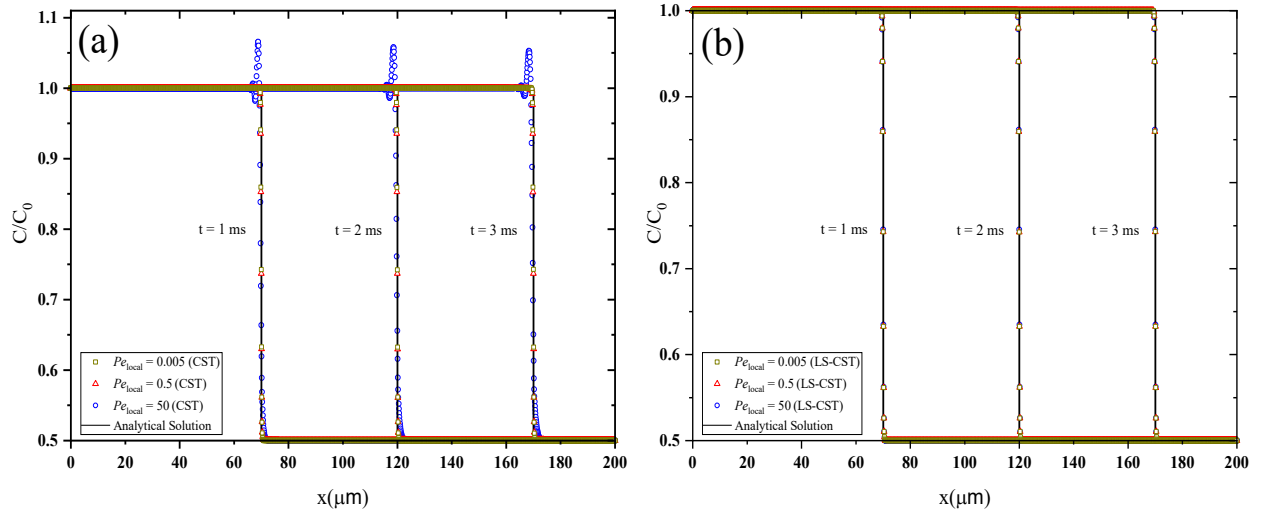


Figure 5.4. Concentration profiles of (a) LS-CST and (b) LS-C-CST approaches at different times for $Pe_{local} = 0.005, 0.5,$ and 50 cases.

5.5 Lid-Driven Cavity

During the drainage process, clusters of the wetting phase can be trapped in dead-end pores as the non-wetting phase saturation increases. Roman et al. (2016) observed that the residual saturation is not immobile during drainage; instead, a recirculating motion is observed. It is similar to lid-driven cavity flow, where the viscous shear force results in the internal circular movement of the displacement fluid. Roman et al. (2016) indicated that the recirculating phenomena may affect the multicomponent mass transport through interface renewal enhancing mixing.

This section considers a single two-dimensional cavity to the wetting phase trapping in the dead-end pores during displacement. The main objective is to investigate the viscous coupling effects on interphase mass transfer. Cases with different viscosity ratios (M) and capillary numbers ($Ca = \mu_w U / \sigma$) are tested. The schematic of the cavity is illustrated in

Figure 5.5. Initially, the bottom cavity (blue section) is saturated with the wetting phase (20% DI water + 80% glycerol), and the top part of the microchannel (orange section) is filled with the non-wetting fluid. Then, the non-wetting fluid (Silicone oil five cSt) is injected at a constant flow rate ($U_0 = 1.45 \times 10^{-3}$ m/s) from the left boundary. A constant pressure condition, $P = 0$, is imposed on the right boundary. A wetting and no-slip boundary condition is assigned to other boundaries. The properties of the fluid and other relevant parameters are listed in **Table 5.1** (Roman et al., 2020). $Ca = 4.74 \times 10^{-3}$ and $M = 0.094$. A two-step process is simulated. First, a drainage process is achieved by injecting the non-wetting phase at a constant velocity, and the system reaches a steady state with the interface configuration matching the given contact angle. Then, a species i is injected from the left boundary at $C_i = 1$ mol/m³. The hydrodynamic simulation, coupled with the mass transfer, begins. The diffusion coefficient of species i in wetting and non-wetting fluid is $D_{w,i} = D_{nw,i} = 1 \times 10^{-9}$ m²/s, and the dimensionless Henry's constant at the interface is $H_i = 0.5$. The corresponding global Péclet number is 362.5, with the characteristic length as the radius of the cavity ($L = 2.5 \times 10^{-4}$ m).

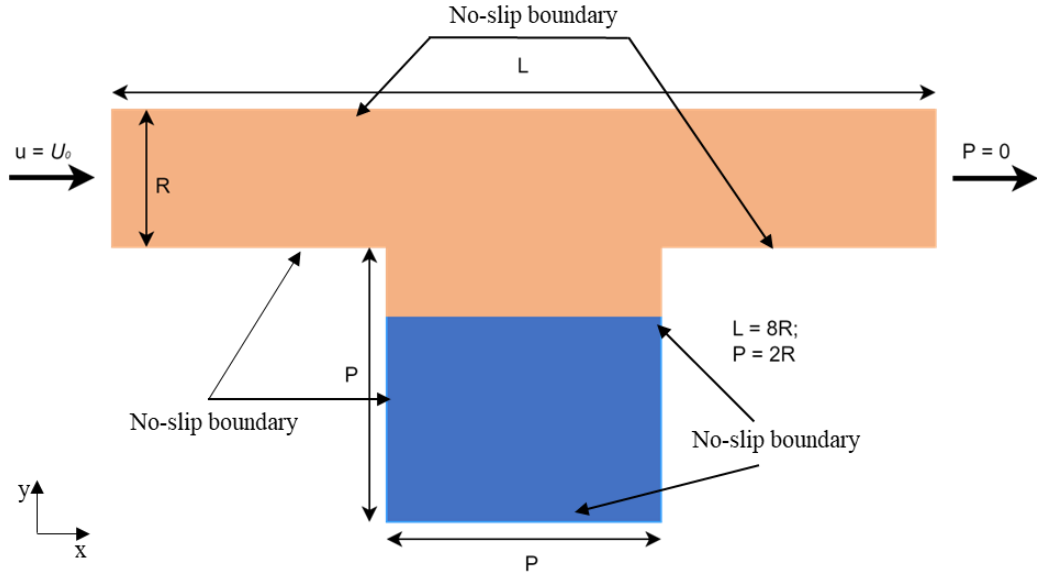


Figure 5.5. Schematic of the single lid-driven cavity.

Table 5.1. Fluid properties for case #1.

Parameters	Value
Wetting fluid density (20% DI water + 80% glycerol) (kg/m^3)	1000
Wetting fluid viscosity (20% DI water + 80% glycerol) ($\text{mPa}\cdot\text{s}$)	49
Non-wetting fluid density (Silicone oil 5 cSt) (kg/m^3)	1000
Non-wetting fluid viscosity (Silicone oil 5 cSt) ($\text{mPa}\cdot\text{s}$)	4.6
Surface tension coefficient (mN/m)	15
Contact angle ($^\circ$)	45

Cases with different viscosity ratios (M) are designed to explore the effect of fluid dynamics properties on the recirculation within the trapped phase and associated interphase mass transfer. Fig.6 presents the simulation results of the velocity profile at equilibrium and concentration distribution at different times for each case of M . Comparing **Figures 5.6a, f, k, and p**, and we can see that the velocity vortex centroids shift to the right when M increases

from 0.09. The more the invading viscosity, the more drag force is exerted on the interface, pushing the interface to the right side.

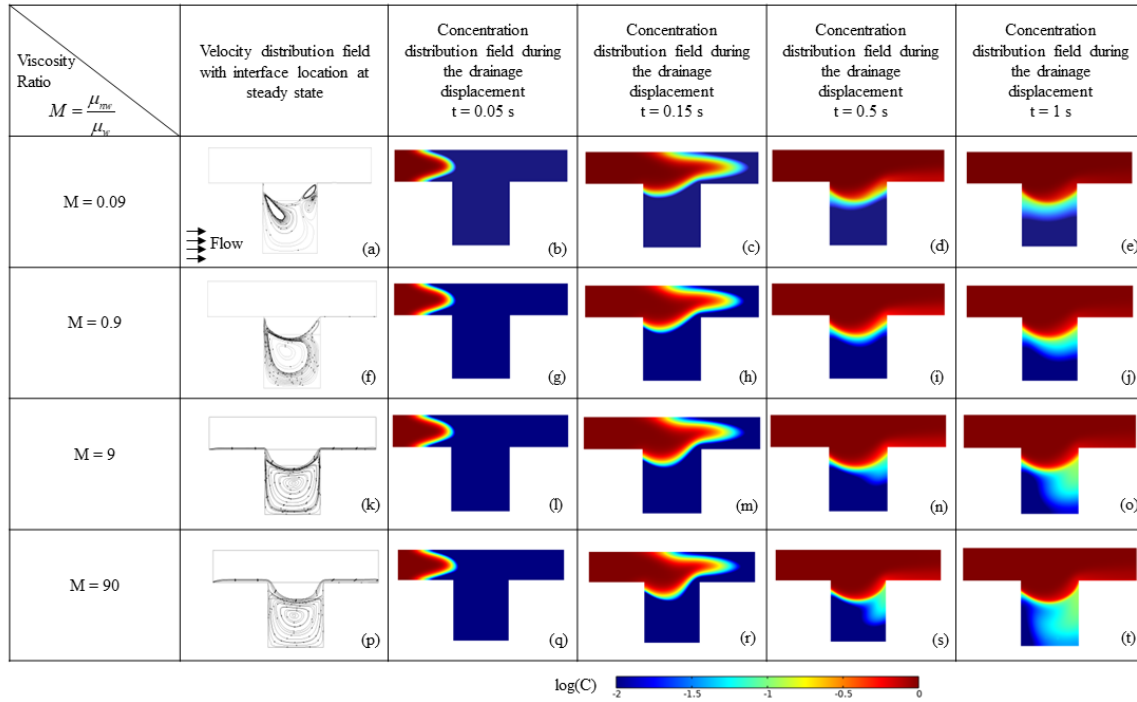


Figure 5.6. Simulated velocity profiles at steady state and concentration fields at different times for different viscosity ratios.

Then, the average velocity within the trapped phase is computed. Several cases with different non-wetting phase viscosity, corresponding to a viscosity ratio ranging from 0.94 to 94, are added. The results are shown in **Figure 5.7**. It is observed that the average velocity within the trapped phase exhibits a linear relationship with $\ln(M)$.

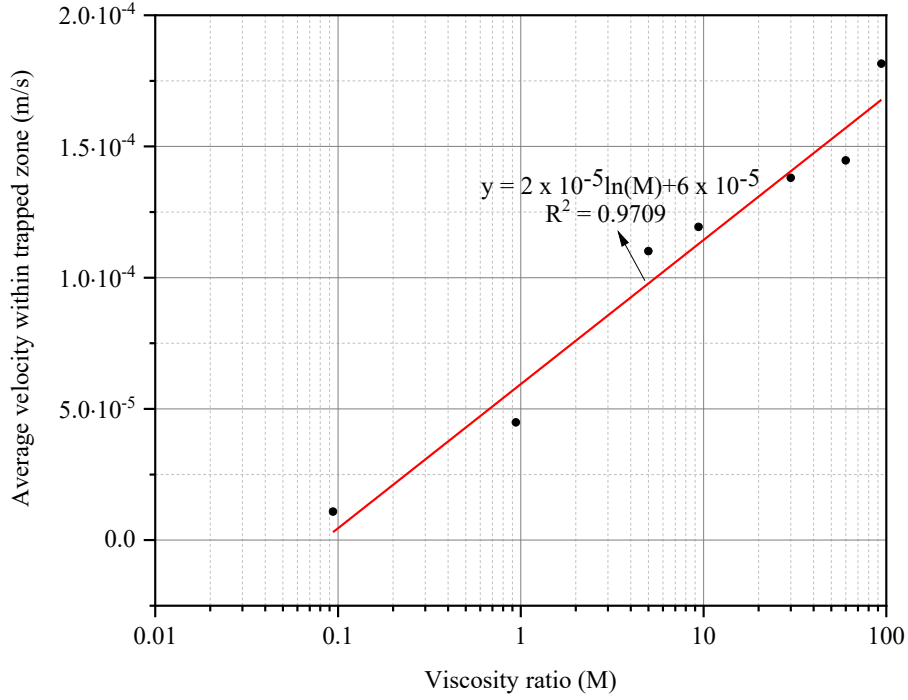


Figure 5.7. Average velocity within trapped zone versus viscosity ratio.

The global concentration distribution for various viscosity ratios at different times is plotted in **Figure 5.6**. In the early time, species i in the non-wetting phase did not reach the main channel's central part until the first pocket (**Figures 5.6b** and **c**). Thus, the species concentration in the wetting phase equals 0. It propagates by advection and diffusion in the following non-wetting phase and reaches the pocket area until the thermodynamic equilibrium at the interface is satisfied. Furthermore, we then investigate the effect of M quantitatively on interphase mass transfer. The following equation can compute the concentration of species i in each phase p .

$$C_{i,p} = \frac{\int_V \frac{\phi_p C}{\phi_{nw} + H(1-\phi_{nw})} dV}{\int_V \phi_p dV} \quad p = nw, w \quad (5.32)$$

The pore-scale simulation results can then be used to compute the effective mass transfer coefficient k_i at the macro-scale, which combines the effect of diffusion, dispersion,

and interfacial transport (Leung and Srinivasan, 2012). The mass flux F_i is a function of k_i , the effective interfacial area a , and the driving force or local concentration difference (Soullaine et al., 2011; Agaoglu et al., 2015):

$$F_i = k_i a (H \overline{C_{i,mw}} - \overline{C_{i,w}}) \quad (5-33)$$

where a is defined as the area of the fluid-fluid interface, which can be numerically assessed by averaging the magnitude of the gradient of the phase fraction, $\|\nabla\phi\|$, over the domain. The local mass flux of species i across the interface can be directly computed by:

$$\dot{m}_i = ((-D\nabla C) - D \frac{C(H-1)}{\phi + H(1-\phi)} \nabla\phi) \cdot \nabla\phi \quad (5-34)$$

The mass flux F_i can be calculated by integrating \dot{m}_i the computational domain. The evolution of average concentration in both phases of different viscosity ratios is compared in **Figure 5.8a**. A similar trend of the average concentration of species i in the non-wetting phase of different viscosity ratios is observed. As M increases, the average concentration in the wetting phase increases. Furthermore, **Figure 5.8b** illustrates the changing trend of the total mass flux per interfacial area and the concentration difference (driving force) for different viscosity ratios. **Figure 5.9** shows the mass flux per interfacial area as a function of the concentration difference for different viscosity ratios. This plot is generated by using the data in **Figure 5.8b**. A positive correlation is observed between the mass flux per interfacial area and the concentration difference in each case, as expected from **Equation 5.33**.

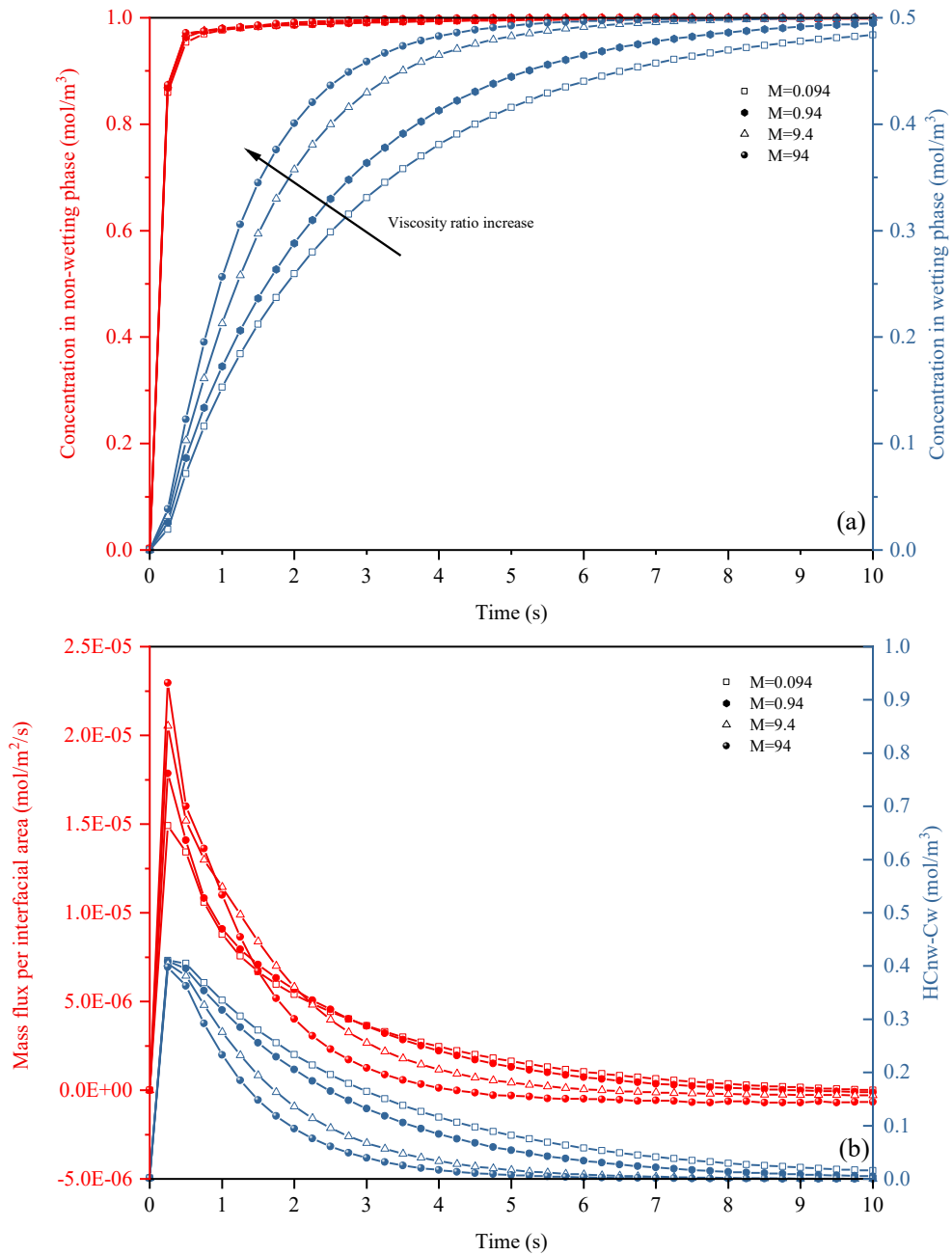


Figure 5.8. Simulation results for different viscosity ratios. (a) Average concentration in each phase versus time; (b) red curve – Mass flux per interfacial area and concentration difference versus time.

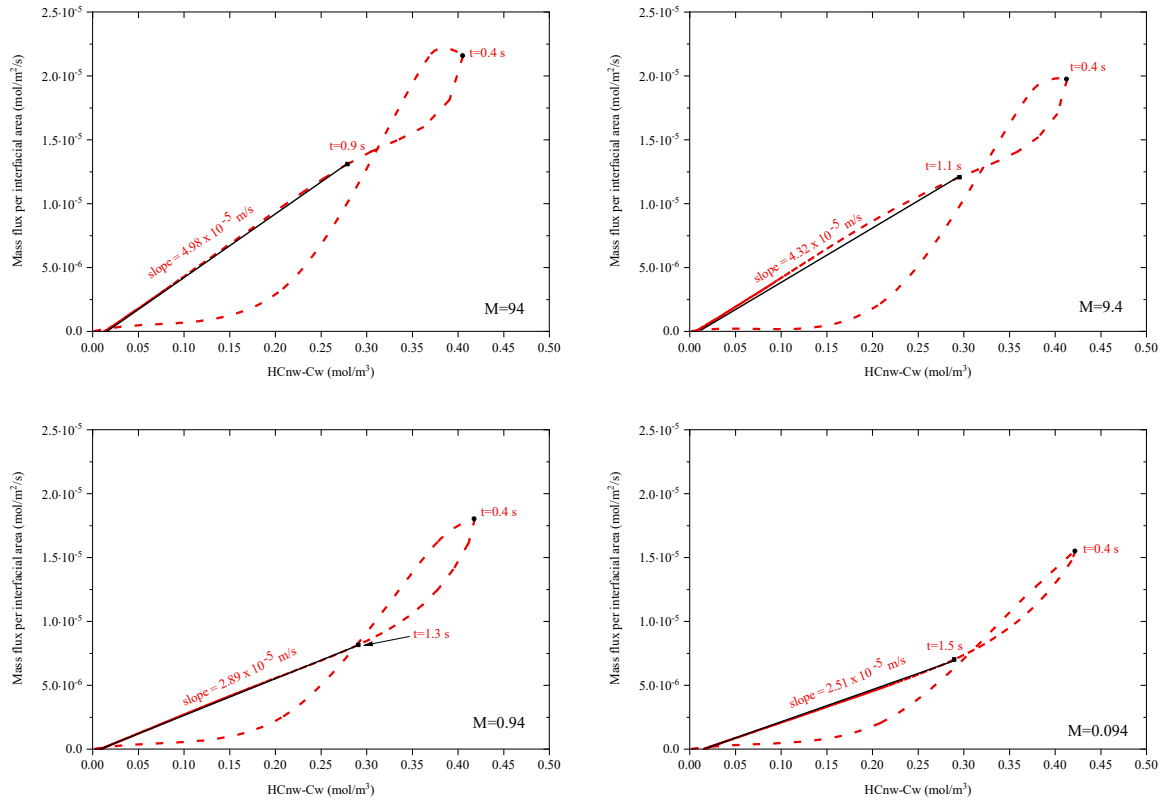


Figure 5.9. The mass flux per interfacial area at a particular time versus the corresponding concentration difference for different viscosity ratios.

In **Figure 5.9**, it can be observed that in all cases, the higher the viscosity ratio, the larger the mass flux per interfacial area, which corresponds to the lower concentration difference. We also note that after a certain period corresponding to the species' travel time across the domain (time case dependency), the mass flux per interfacial area can be approximated linearly in function of the concentration difference. Based on the linear transfer mode (**Equation 5.31**), the slope corresponds to the value of the effective mass transfer coefficient, k_i . For each case, the value of k_i after reaching the stable state is computed, and the results are shown in **Figure 5.9**. We observed that the viscosity ratio affects the interphase mass transfer and that this effect increases as the viscosity ratio increases.

5.6 Summary

A conservative LS-based single-field interphase mass transfer model (LS-CST) was proposed to model multiphase species transport at the pore scale. A consistent interphase mass transfer equation was coupled with a conservative LS method. This method is designed for a wider range of Péclet number cases, especially convection-dominated cases.

The proposed model was validated against analytical solutions for various specific setups. Compared with the standard CST method, we illustrated the proposed framework's capabilities to simulate convection-dominated cases with reasonable accuracy.

The LS-CST model has been used to investigate the viscosity ratio effect on the interphase mass transfer in the cavity where the wetting phase is trapped in the dead-end pore during the displacement process under various conditions and upscale the effective mass transfer coefficient at the REV scale. The recirculation motion inside the immobile pocket of the wetting phase was due to the momentum transmitted by the flowing non-wetting phase, which agrees with the experimental observation. The average velocity within the trapped phase in the pocket has a linear relationship with the natural logarithm of the viscosity ratio.

The upscaled effective mass transfer coefficient was computed for each case and showed a linear relationship with the average concentration difference (driving force) after a certain period.

This simulation framework and the upscaling methodology provide a robust tool for investigating and characterizing the interphase multicomponent mass transfer process under various conditions.

CHAPTER 6 : PORE-SCALE NUMERICAL SIMULATION OF VAPORIZED SOLVENT-BASED PRODUCTION PROCESSES

6.1 Overview

Against the backdrop of emissions reduction and energy efficiency in heavy oil and bitumen deposits, producing these resources remains a major challenge due to their high viscosity and low mobility. While existing thermal recovery operations have been criticized for being energy-intensive and environmentally damaging, solvent-based recovery processes offer a promising alternative. Despite numerous experimental and numerical studies on solvent-based recovery processes, there is a lack of mechanistic modeling studies at the pore scale to explore how to simulate interphase mass transfer mechanisms at the bitumen/solvent interfaces. Quantitative analysis of pore-scale effects is important in designing efficient field-scale production.

A two-phase multicomponent transport pore-scale simulator has been developed in the previous chapters to analyze the mass transfer mechanisms during the solvent recovery process. This pore-scale model employs the level-set (LS) method and a new consistent continuous species mass transfer formulation with LS to track the interface movement and interphase mass transfer. A series of partial differential equations are discretized by applying the finite-element method and then solved successively. The proposed model was validated against the analytical models related to multiphase fluid flow and mass transfer in Chapter 5. In this chapter, numerical simulation of the vapor extraction (VAPEX) process with uniform pore structure was studied to reproduce experimental observations. The influence of interfacial mass transfer was explored. Various Peclet numbers were studied to investigate

the effect on the upscale mass transfer during the VAPEX process at the Representative Elementary Volume (REV) scale. An original contribution of this work is to provide a general framework to simulate the interphase mass transfer with complex pore structures, providing a fundamental understanding of the physical phenomena. Moreover, the developed framework provides a modeling tool for incorporating relevant physical phenomena with promising potential for integration into pilot- or field-scale simulation models.

6.2 Pore-Scale Mechanisms

Heavy oil/bitumen, characterized by its high viscosity and density, is a crucial component of the global energy supply. Thermal-based recovery techniques, especially steam-assisted gravity drainage (SAGD), have been considered Canada's most common commercial technique (Farouq Ali, 2003). However, such techniques, such as significant greenhouse gas emissions and water usage, are traditionally energy-intensive and environmentally challenging. On the other hand, solvent-assisted recovery techniques are among the most promising opportunities to reduce GHG emission intensity from the oil sands and offer an environmentally sustainable alternative to the SAGD process. The focus here is the vapor extraction (VAPEX) process, which involves the use of a light hydrocarbon (such as propane, butane, or a mixture) to reduce the viscosity of heavy oil through mass transfer phenomena, facilitating its flow and extraction (Pourabdollah and Mokhtari, 2013).

As mentioned above, solvent processes are generally less effective than thermal-based recovery processes because mass transfer diffusion/dispersion is much slower than thermal energy transfer (e.g., thermal convection). Moreover, experimental works suggested that injected solvents could enhance the in-situ upgrading of the heavy oil due to the in-situ asphaltene precipitation (Haghighat and Maini, 2010; Mworira et al., 2024). Indeed,

experimental works conducted in the sand-packed porous medium have shown a higher recovery rate than Hele-Shaw cell experiments, considerably higher than the theoretical predictions (Das, 1997; Das and Butler, 1998; Boustani and Maini, 2001). Singhal and Das et al. (1996) attributed this increase (e.g., up to a 10-fold increase) to an enhanced interfacial contact area in porous media due to the pore-size heterogeneity. On the other hand, several VAPEX experiments conducted by Yazdani and Maini (2005) suggested that convection dispersion is a significant factor in porous medium in addition to molecular diffusion. VAPEX pore network glass micromodels experiments were conducted by Chatzis (2002) to investigate the important features of the VAPEX process (butane was used as vapor solvent) at the pore-scale level. The pore-scale visualization observed by Chatzis revealed that the oil production rate in VAPEX remains constant for a system given length. Chatzis concluded that the reason is that the geometry of the interface stays the same over the production. Indeed, he observed that the relatively large pores closest to the solvent chamber are the first to drain, starting from the top portion of the micromodels. Observed phenomena by Chatzis (2002) indicate that the snap-off mechanism and trapped vapor enhance the mass transfer rate through increased vapor solvent diffusivity due to the reduced heavy oil viscosity. No asphaltene precipitation was observed during this displacement process with vapor butane (Chatzis, 2002). Followed by Chatzis (2002), James (2009) designed several VAPEX micromodels and slabs of consolidated and unconsolidated glass beads to understand the pore-scale events better. James (2009) further concluded that the VAPEX interface velocity is linear with time for a given cross-section. The porous media characteristics (e.g., particle size, pore size, and aspect ratio) profoundly affect the VAPEX interface advancement velocity (James and Chatzis, 2004a). The recovery efficiency is a combination effect of

capillary phenomena, including drainage and imbibition type displacements at the pore scale, film flow, and gravity effect of the live oil (James and Chatzis, 2004a). Marangoni effect induced by surface tension gradient along the interface also reported as a key mechanism in oil recovery process (Lam et al., 1983; Lyford et al., 1998; Fletcher and Davis, 2010). During the VAPEX process, the Marangoni convection driven by surface tension gradient due to solvent concentration can enhance the rate of interphase mass transfer. To the best of the authors' knowledge, few numerical studies related to the literature were conducted to investigate the pore-scale mechanisms during the VAPEX process. Bayestehparvin et al. (2021) developed a 2D VAPEX pore-scale model followed by a Continuous Species Transfer (CST) model to predict the chamber front velocity and chamber propagation. However, the gravity effect, the primary mechanism of the VAPEX process, was ignored in their approach.

Pore-scale simulations of the interphase mass transfer studies mainly focused on the dissolution of non-aqueous phase liquids (NAPLs) in porous medium (Agaoglu et al., 2016; Aminnaji et al., 2019; Held and Celia, 2001; Graveleau et al., 2017; Sarikurt et al., 2017). The methods involved can be divided into the pore network models (PNM), Lattice Boltzmann methods (LBM), and the Direct Numerical simulation (DNS). PNM methods typically simplified the void space of porous medium as a network of pores connected by pore throats were governed by Poiseuille's law. The limitation of this simplification is that may not be able to capture the complex geometries of real pore spaces (Blunt et al., 2002). Indeed, PNM are often limited to accurately determining the fluid-fluid interfacial area, which is a significant parameter to compute the interphase mass transfer. LBM is a powerful tool to simulate the multiphase mass transfer at the pore scale. However, incorporating complex physical processes, such as chemical reaction or phase change, into LBM can be

more challenging compared to traditional computational fluid dynamics (CFD) methods. Here, the CFD methods provide an alternative way to simulate the interphase mass transfer in the multiphase flow, where Navier-Stokes equations are directly solved in the void space of the porous medium. Volume of fluid (VOF), level-set method (LS), and phase field method (PFM) are the main interface capturing methods. The main challenges of simulating the multiphase interphase transfer at pore-scale is handling the flux continuity and the concentration jump at the fluid-fluid interface. Haroun et al. (2010) developed a robust formulation, named as Continuous Species Transfer (CST) method in the framework of the VOF (VOF-CST) to insure the interface boundary conditions. Maes and Soullaine (2018) further improved this method with an additional compressive term to simulate convection-dominated regime more accurately. Our previous work (Yu and Leung, 2024) derived a consistent species mass transfer formulation based on the conservative level-set method, labelled to LS-C-CST method. Compared to the color function feature of VOF, the conservative LS method provides a high accuracy to handle the topological changes with a smooth continuous function. To the best of the authors' knowledge, few numerical studies related to the literature were conducted to investigate the pore-scale mechanisms during the VAPEX process. Bayestehparvin et al. (2021) developed a two-dimensional VAPEX pore-scale model followed by a Continuous Species Transfer (CST) model to predict the chamber front velocity and chamber propagation. The simulated interfacial velocity at the chamber edge shown a good agreement with experimental values. Capillary effect and trapped oil phenomena were all observed in the simulation results. However, the gravity effect, the primary mechanism of the VAPEX process, was ignored in their approach. The model's boundary conditions are not consistent with the experimental setup.

Therefore, one key challenge is incorporating the main mechanisms during the VAPEX process with the proposed LS-C-CST method to further have a better understanding of the Darcy scale observations based on the simulation of the physics processes taking place at the pore-scale level. In this study, a two-dimensional two-phase pore-scale model with interphase mass transfer is developed based on LS-C-CST method to investigate the main mechanisms during the VAPEX process. The detailed physical transport process or interfacial knowledges including the diffusion and convective mass transfer in a porous medium allows us to explain the experimental observations.

6.3 Mathematical Formulation

In this section, we introduce the main governing equations to solve the two-phase interphase mass transfer in porous medium at the pore-scale. The pressure, velocity, and the fluid-fluid interface are solved by the Navier-Stokes equations in the level-set framework. Then, we solved the developed LS-C-CST formulation to capture the evolution of the solvent concentration. During the VAPEX process, the solvent concentration has a significant effect on the heavy oil properties and further effect on the recovery factor. Therefore, such physics processes, including the multiphase flow, interface movement, and mass transfer are fully coupled with each other.

The following simplifications and assumptions are invoked: (1) The solvent molecules can diffuse away from the interface following Fick's law, and the solvent concentration distribution at the gas-liquid interface can be described by Henry's law. (2) Incompressible system. (3) No asphaltene precipitation. (4) Laminar flow. (5) Newtonian

fluids as the diluted heavy oil becomes Newtonian (Chen et al., 2005). (6) Isothermal conditions. (7) Only mass transfer of component solvent occurs between the phases.

6.3.1 Hydrodynamics equation

In this work, the Navier-Stokes equations for multiphase flow are solved with the level-set method, which has been widely used to track the fluid-fluid interface. The governing equation

$$\text{of the standard LS is defined as a distance function, } f_{LS} \text{ given by: } \frac{\partial f_{LS}}{\partial t} + \nabla(\vec{u}f_{LS}) = 0 \quad (6.1)$$

where the f_{LS} is defined as,

$$|f_{LS}(\vec{x})| = \min_{x_i \in I} (|\vec{x} - \vec{x}_I|) \quad (6.2)$$

where I is the interface; if $f_{LS}(\vec{x}) > 0$ (respectively $f_{LS}(\vec{x}) < 0$), then the cell is occupied by one phase (respectively the other phase) only. The interface is represented naturally by the cells when $f_{LS}(\vec{x}) = 0$. As discussed above, one of the drawbacks of the standard LS method is that they are not mass-conservative (Olsson and Kreiss, 2005; Maes and Soulaire, 2018).

To achieve numerical robustness, a smeared-out Heaviside function is introduced (Olsson and Kreiss, 2005).

$$\phi = H_\varepsilon(f_{LS}(\vec{x})) = \begin{cases} 0 & f_{LS} < -\varepsilon \\ \frac{1}{2} \left(1 + \frac{f_{LS}}{\varepsilon} + \frac{1}{\pi} \sin\left(\frac{\pi f_{LS}}{\varepsilon}\right) \right) & -\varepsilon \leq f_{LS} \leq \varepsilon \\ 1 & f_{LS} > \varepsilon \end{cases} \quad (6.3)$$

where ε corresponds to half of the thickness of the interface; and ϕ is the new defined smoothed LS function and define a sharp interface at $\phi = 0.5$ and the values from 0 to 1 away from the interface. The convection of the reinitialization level-set function reads as follows:

$$\frac{\partial \phi}{\partial t} + \vec{u} \cdot \nabla \phi = \gamma \nabla \cdot \left(\varepsilon \nabla \phi - \phi(1-\phi) \frac{\nabla \phi}{|\nabla \phi|} \right) \quad (6.4)$$

where γ is the re-initialization term and a suitable value is the maximum expected velocity magnitude.

With the incompressible, Newtonian fluid, and laminar flow assumptions, the velocity and pressure are solved throughout the entire computational domain by a single-field (Gueyffier et al., 1999) Navier-Stokes equations in the LS framework under the isothermal conditions. In this study, the gravity effect is considered here due to the VAPEX process.

$$\nabla \cdot \vec{u} = 0 \quad (6.5)$$

$$\rho \frac{\partial \vec{u}}{\partial t} + \rho \vec{u} \cdot \nabla \vec{u} = -\nabla p + \nabla \cdot \mu (\nabla \vec{u} + \nabla \vec{u}^T) + \vec{F}_{Ma} + \rho \vec{g} \quad (6.6)$$

Here, the material properties, such as the density and viscosity, in single-field formulation are defined the weighted averages of the fluid phase fraction p ($p = l, g$) over the entire computational domain as,

$$\begin{aligned} \rho &= \rho_1 \phi_1 + \rho_2 \phi_2 \\ \mu &= \mu_1 \phi_1 + \mu_2 \phi_2 \end{aligned} \quad (6.7)$$

where F_{Ma} is the the volume force induced by the surface tension, including the Marangoni effect, and it is evaluated numerically

$$F_{Ma} = f_s(x) \delta(x - x_s) \quad (6.8)$$

where x_s is the point on the interface, δ is the Dirac delta function, and f_s is the surface tension force per interfacial area, can be expressed as:

$$f_s = \sigma \kappa \vec{n} + \nabla_s \sigma \quad (6.9)$$

where σ is the surface tension coefficient,

δ represents a Dirac delta function that is nonzero only at the fluid-fluid interface with defined

as $\delta = 6|\phi(1-\phi)||\nabla\phi|$; κ is the curvature; and \vec{n} is normal vector of the fluid-fluid interface.

:

$$\vec{n} = \frac{\nabla\phi}{|\nabla\phi|} \quad (6.10)$$

$$\kappa = -\nabla \cdot \vec{n}. \quad (6.11)$$

In **Equation 6.9**, the first term on the right side shows the effect on the surface tension force while the second term represents the Marangoni effect force induced by the surface tension gradient along the interface.

A wetted wall boundary condition is imposed on the surface of each solid grain for the LS equation, and the contact angle for the wetting phase θ is set to a constant value. The no-slip boundary condition is also applied on the surface of each solid grain.

$$\vec{n}_{wall} \cdot (\varepsilon_{ls} \nabla\phi - \phi(1-\phi) \frac{\nabla\phi}{|\nabla\phi|}) = 0 \quad (6.12)$$

where ε_{ls} represents the interphase thickness and is defined as half of the maximum element size for numerical stability.

6.3.2 LS-C-CST Method

The compressive interphase mass transfer (LS-C-CST), based on the level-set method, is derived and validated in Chapter 5. During the VAPEX process, the solvent mass transfer across the interface and diffuses into the heavy oil phase has a significant impact on the fluid properties and oil recovery. Thus, mass transfer simulations were implemented by introducing the species transport equation and fully coupled with the hydrodynamics

equations. The main challenge of simulating interphase mass transfer in two-phase flow is that the discontinuity across the interface created by the thermodynamics equilibrium at the interface. Haroun et al. (2010) proposed a single-field species mass transport equation to insure the concentration discontinuity and flux continuity at the interface.

$$\frac{\partial C_i}{\partial t} + \underbrace{\nabla \cdot (\vec{u} C_i)}_{\text{convection}} = \underbrace{\nabla \cdot (D_i \nabla C_i)}_{\text{diffusion}} + \underbrace{\nabla \Phi_i}_{\text{discontinuity}} \quad (6.13)$$

where

$$C_i = \phi C_g + (1 - \phi) C_l \quad (6.14)$$

$$\Phi = -\frac{C_i(1-H)}{\phi + H(1-\phi)} \nabla \phi \quad (6.15)$$

$$D_i = \frac{1}{\frac{\phi}{D_g} + \frac{1-\phi}{D_l}} \quad (6.16)$$

Here D_i is the effective diffusion coefficient, and Deising et al. (2016) suggested that the harmonic average of the local phase diffusion coefficient is more robust. However, this standard CST method suffers the numerical stability issues when simulating the convection-dominated process (Yang et al., 2017; Maes and Soullaine, 2018; Yu and Leung, 2023). To solve these issues, we revisit and rederive the species transport equation in the conservative LS framework. The details derived steps can refer to Yu and Leung (2024). The final form of the LS-C-CST formulation is given as:

$$\begin{aligned} \underbrace{\frac{\partial C_i}{\partial t}}_{\text{accumulation}} + \underbrace{\nabla \cdot (\vec{u} C_i)}_{\text{convection}} = \underbrace{\nabla \cdot (D \nabla C_i)}_{\text{diffusion}} \dots \\ - \underbrace{\nabla \cdot \left(D \frac{C_i(1-H)}{\phi + H(1-\phi)} \nabla \phi \right)}_{\text{discontinuity}} + \underbrace{\gamma \mathcal{N} \cdot \left(\left(\frac{C_i(1-H)}{\phi + H(1-\phi)} \right) \left(\varepsilon \nabla \phi - \phi(1-\phi) \frac{\nabla \phi}{|\nabla \phi|} \right) \right)}_{\text{diffusion flux} \quad \text{compression flux}} \end{aligned} \quad (6.17)$$

The local mass flux of species i across the interface can be directly computed by:

$$\dot{m}_i = ((-D\nabla C) - D \frac{C(H-1)}{\phi + H(1-\phi)} \nabla \phi) \cdot \nabla \phi \quad (6.18)$$

The numerical implementation of the proposed model in COMSOL has been verified in the previous section by comparing it with the simple geometry with proper boundary and initial conditions where the analytical solution exists.

6.4 Physical Model Description

We performed a VAPEX micromodel experiment by James (2009) for model validation to investigate the VAPEX process. The micromodel pattern of the pore network has a uniform pore structure, including the dimension information, as shown in **Figure 6.1**. The experimental setup was explained in detail in Chatzis (2002). For simplicity, the micromodel was first filled with heavy oil and no residual water in this experiment. A ditch-like channel (a permeable trough) was constructed along one side of the micromodel, which serves as a vertical line source of vapor solvent to simulate the falling film over a vertical plate (Chatzis, 2002). Vapor solvent was allowed to enter the micromodel at the top of the trough, and the dilute heavy oil produced accumulated at the bottom part of the model. A schematic of the experimental setup is shown in **Figure 6.2**. The dynamic VAPEX experiments were conducted by allowing the vapor solvent to enter the system at a constant rate. **Table 6.1** shows the fluid properties for solvent extraction experiments.

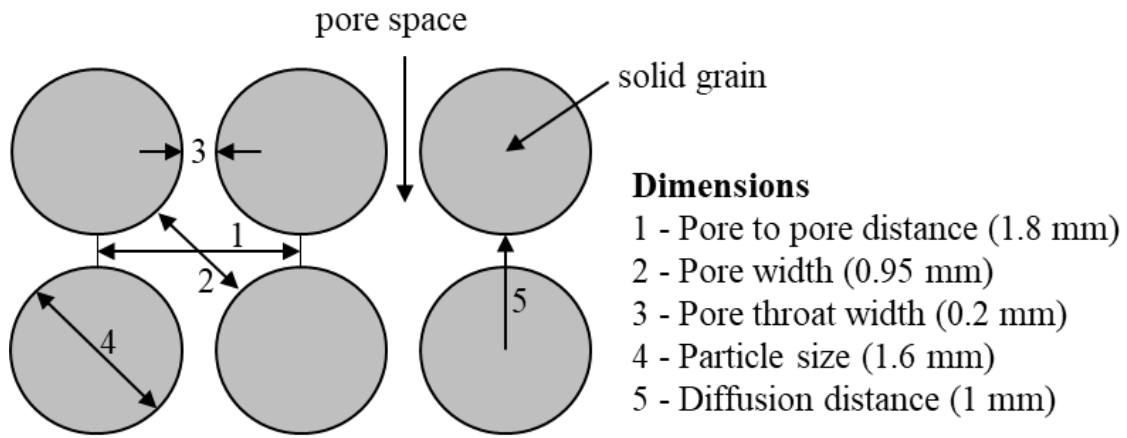


Figure 6.1. The Micromodel Design and Micromodel Pattern.

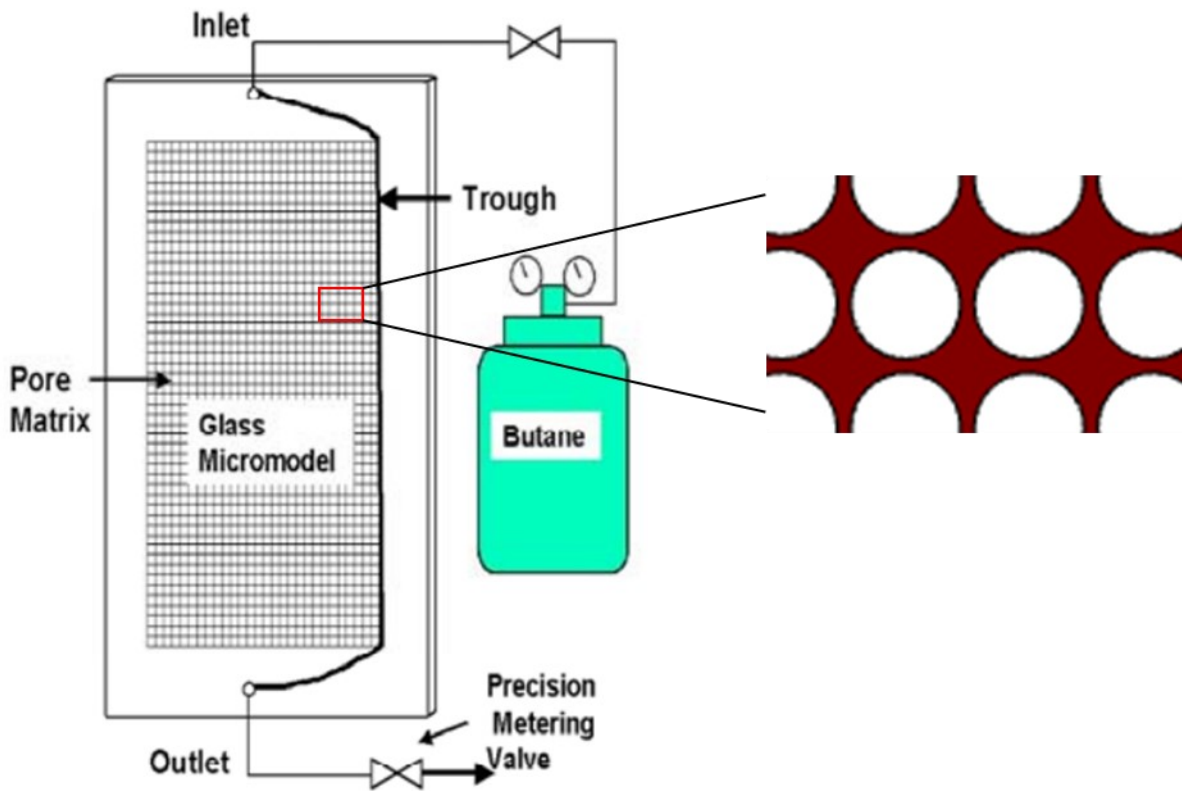


Figure 6.2. Schematic of the Experimental Setup (Modified from Chatzis, 2002).

Table 6.1. Fluid Properties for Solvent Extraction Experiments (James, 2009)

Fluid Properties	Value
Bitumen density, (kg/m ³)	987
Bitumen viscosity, (cP) @25 °C	23,000
Live oil density (diluted bitumen), (kg/m ³)	811.1
Live oil viscosity (diluted bitumen), (cP) @25 °C	5
n-Butane density (v) @25 °C, (kg/m ³)	6.2
n-Butane viscosity (v) @25 °C, (cP)	0.015
Diffusion Coefficient in liquid and gas phase, (m ² /s)	6.8 x 10 ⁻¹⁰ (Yang and Gu, 1996)
Dimensionless Henry's constant	0.5 @ 25 °C
Contact angle	45°
Surface tension, (mN/m)	34.7

Considering the computational time, a small model with 15 by 15 oil-wet solid grains with an attached side channel was constructed in this study, as shown in **Figure 6.3**. The domain of the simulated micromodel is 27.2 by 25.2 mm in size. The computational domain is divided into two parts: the main micromodel porous medium domain and an extensive trough channel on the left side. The width of the trough is 2 mm, which is relatively larger than the particle size to serve as a vertical line source of vapor solvent. Following James's experimental setup, the main domain is initially saturated with heavy oil, and the side channel is initially filled with vapor solvent. The vapor solvent ($C_i = C_0$ mol/m³) is injected from the inlet with a constant velocity, $u = 0.001$ m/s. The bottom of the side channel is set up as an outlet with a zero-pressure boundary condition, which is consistent with the experimental

setup. A wetted wall boundary condition with a constant contact angle ($\theta = 45^\circ$) (**Equation 6.9**) was assigned to the surface of sand grains, and other sides of the domain had no flow boundaries (no-slip boundary condition). The initial solvent concentration of the main domain is 0 without any dissolved solvent. The interfacial tension for vapor/heavy oil systems is 34.7 mN/m at a temperature of 25°C (Bowman 1967). The diffusion coefficient of the vapor butane in heavy oil is $9.76 \times 10^{-11} \text{ m}^2/\text{s}$ based on Das and Butler's diffusion model (Das and Butler, 1996). Here, a value of the dimensionless Henry's constant 0.5 is considered for vapor butane in Athabasca bitumen at a temperature of 25°C and atmospheric pressure (Bayestehparvin et al., 2021).

6.5 Numerical Scheme

The numerical simulation was performed using a commercial finite-element-based solver COMSOL Multiphysics 5.5 (2019). A linear solver – parallel direct sparse solver (PARDISO) is used in this study to solve the set of governing equations (COMSOL, 2019). Time stepping is solved with the backward Euler method. The reinitialization parameter γ , was equals to the maximum velocity of the computational domain to retain a constant interfacial thickness. The interface thickness ε , was set equal to half of the maximum element size. The adaptive time-stepping scheme was applied here to adjust the timestep size automatically to maintain the desired relative tolerance (COMSOL, 2019). The computational domain is discretized with total 310,124 triangular elements with the maximum and minimum element sizes equal to 0.054 and 0.011 mm, respectively (Figure 6.3 b).

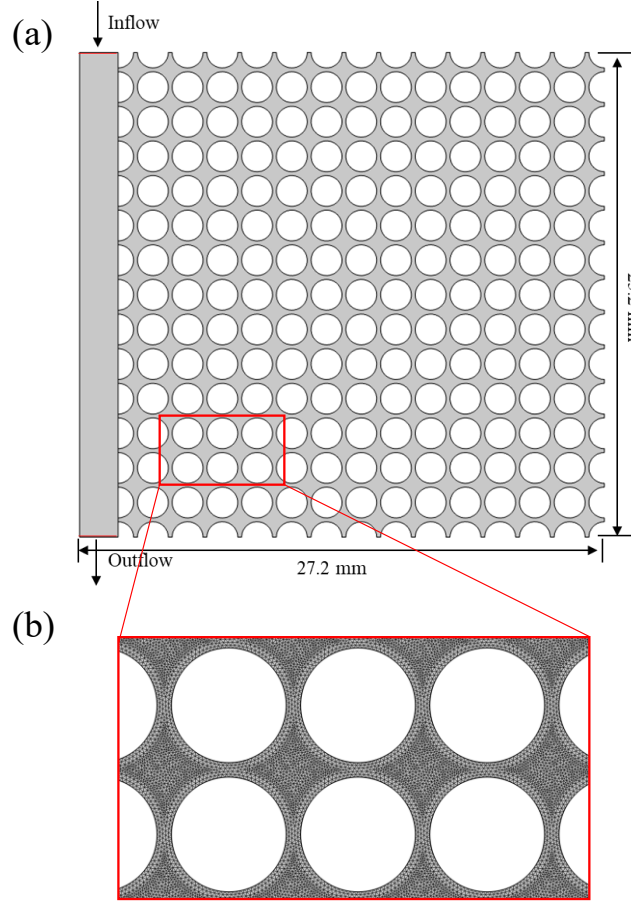


Figure 6.3. Plot of (a) Schematic of the computational domain and related boundary conditions (white area – solid grains; grey area – pore space); (b) finite element mesh generated with triangular elements.

Here, the density of the diluted heavy oil was assumed to be constant due to relatively small change (Sun et al., 2020), and its viscosity variation is considered to be a function of the vapor solvent concentration by a quarter-law mixing rule via the following equation (Koval, 1963; Fshari et al., 2018):

$$\mu = \mu(C) = \left[\frac{C - C_0}{C_{inj} - C_0} \mu_{solvent(v)}^{-0.25} + \left(1 - \frac{C - C_0}{C_{inj} - C_0}\right) \mu_{oil}^{-0.25} \right]^{-4} \quad (6.14)$$

where C_{inj} represents the solvent concentration in the injected solution; C_0 is the initial solvent concentration within the domain, which is considered to be zero in this case.

To consider the Marangoni effect in isothermal condition, the surface tension coefficient σ , is a function of the solvent concentration along the interface. Here, a linear model is introduced to represent the solvent concentration effect on the surface tension coefficient.

$$\sigma = \sigma_0(1 + \gamma C) \quad (6.15)$$

where σ_0 is the surface tension coefficient in a pure system, and γ is a negative constant in most cases. A value of -0.4 for the parameter γ is applied in this model for VAPEX process.

6.6 Results

The model is developed to investigate the VAPEX process and compare interface velocities with the results of James's (2019) experiment. Once communication between the vapor solvent and heavy oil was established, the solvent diffused into the heavy oil porous medium and reduction in viscosity. The simulation results of the phase distribution are shown in **Figure 6.4**.

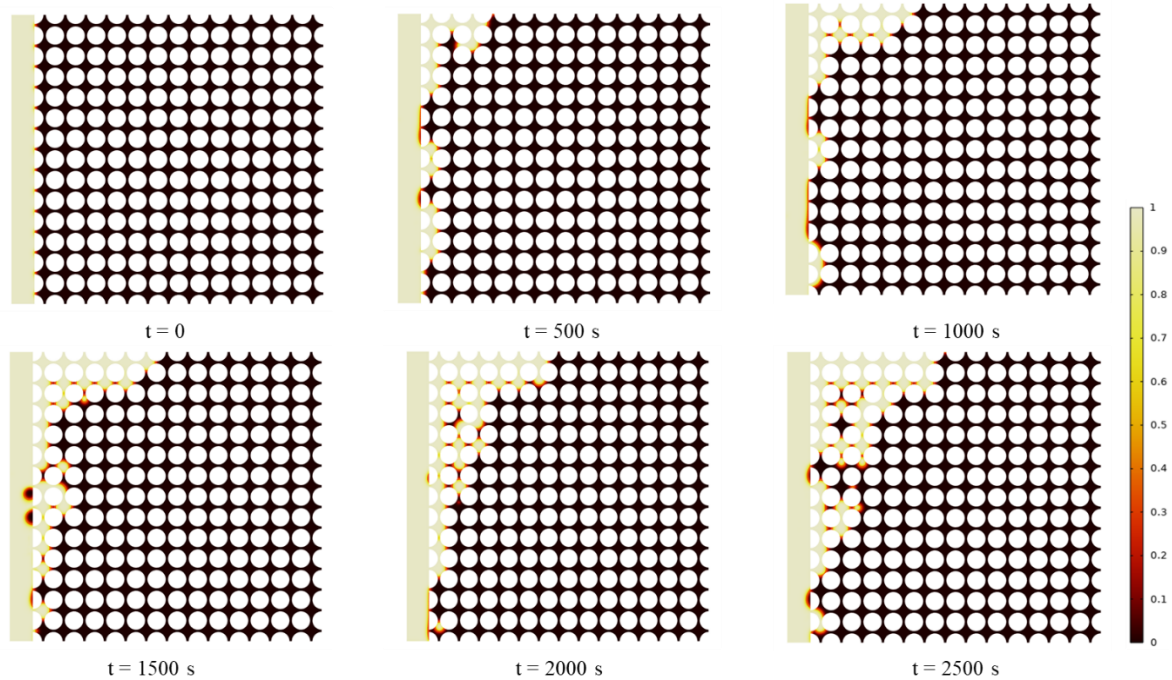


Figure 6.4. Evolution of the phase distribution during the VAPEX Process in a 2D Micromodel (grey area – Vapor solvent; dark area - Bitumen).

As **Figure 6.4** shows, since the solvent concentration difference between the solvent zone and bitumen porous medium, the vapor solvent would be diffused into the bitumen zone. Meanwhile, the buoyance effect arising from the difference in density between the solvent and bitumen leads to the growth of the solvent chamber within the top of the porous medium. The evolution of the solvent concentration within the porous medium is shown in **Figure 6.5**. Considering the dimensionless Henry's constant value of 0.5, the equilibrium of the dimensionless solvent concentration in the bitumen phase is 0.5.

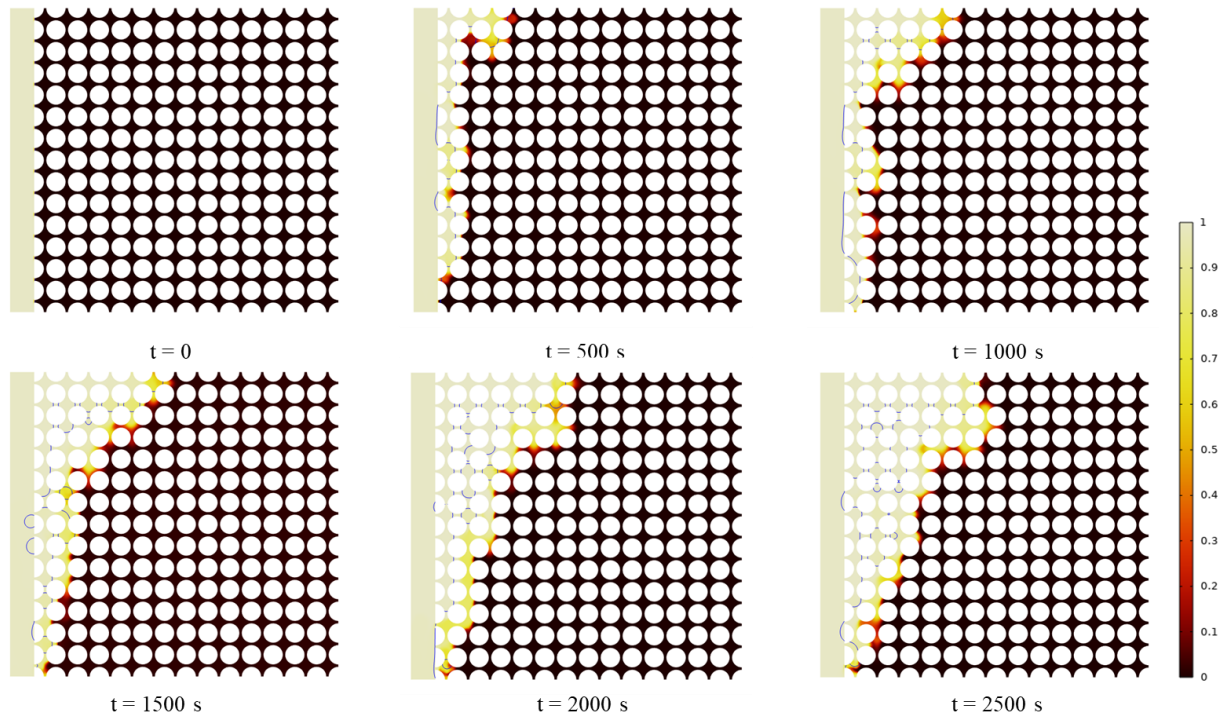


Figure 6.5. Evolution of the vapor solvent concentration distribution during the VAPEX Process in a 2D Micromodel (Grey area – Vapor solvent; dark area - Bitumen).

As Figure 6.6 (b) shows at 500 s, the concentration of diluted heavy oil near the interface (dashed zone) within the swept region is around 0.5, which means this section of the diluted heavy oil reached thermodynamic equilibrium. However, we can see that the solvent concentration of most of the swept area (transition zone) didn't reach the equilibrium after the 2000s later within such a small domain (27.2 x 25.2 mm), which was caused by the low molecular diffusion coefficient and low solubility of the solvent in heavy oil. Thus, convection mass transfer plays a significant role in the solvent-assisted recovery process.

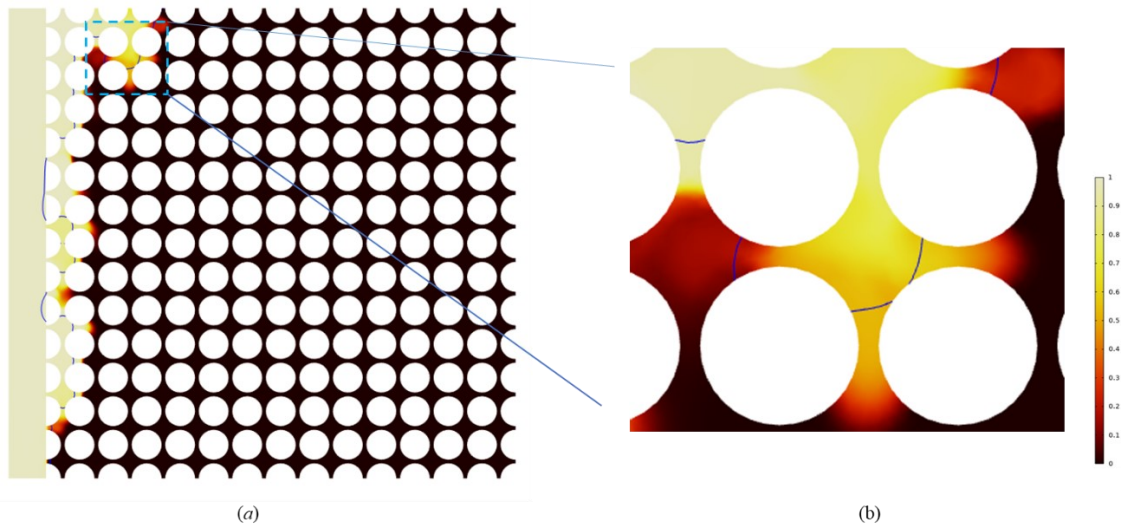


Figure 6.6. (a) Solvent concentration distribution within the porous medium at 500 s; (b) the enlarged area of the swept region near the interface.

When the diluted oil drained into dead-end pore spaces, Chatzis (2002) observed that the paths of oil film would be redirected to form peaks and valleys at the bitumen/solvent interface, referring to **Figure 6.7 (b)**. Similar phenomena were also observed in our simulation works (**Figure 6.7 (a)**), which is consistent with the experimental observations. The diluted oil would flow out once the gravity force overcomes the capillary and viscous forces. To some extent, such phenomena have a negative impact on oil production rates. Due to the capillary phenomena of snap-off mechanisms, the locally trapped vapor solvent in diluted oil-filled pores can be observed in Figure 6.8 (a). As Figure 6.8 (a) shows, the non-wetting phase (vapor solvent) drained the diluted oil (wetting phase). Indeed, the propagation of the bitumen/solvent interface is not uniform in the porous medium due to the effect of the capillary and viscous force.

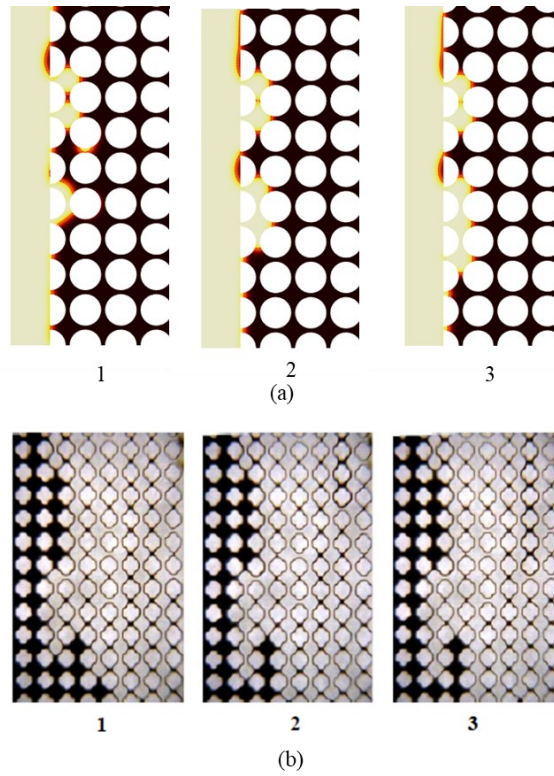


Figure 6.7. Formation of valleys and peaks at the bitumen/solvent interface (a) Simulation results; (b) experimental results (Chatzis, 2002).

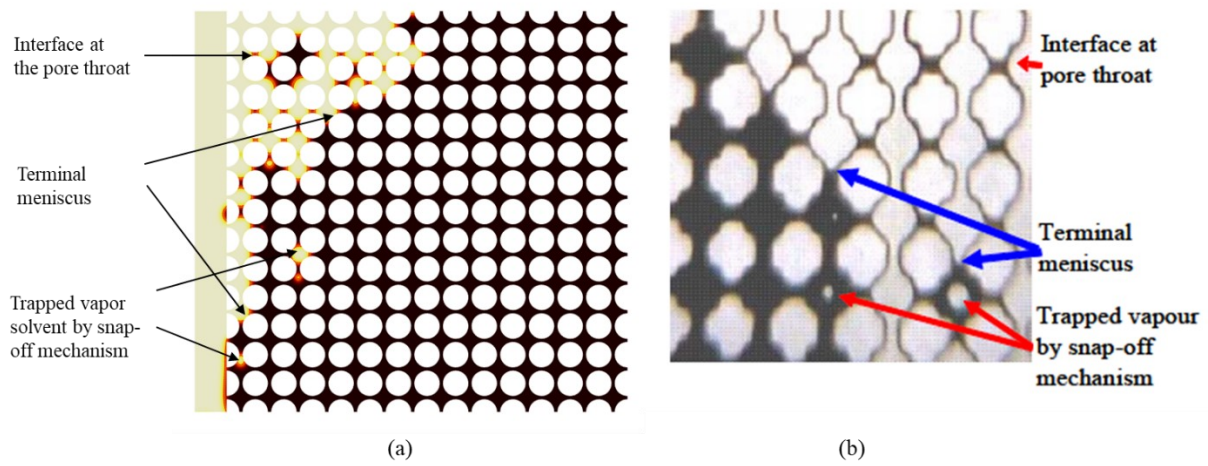


Figure 6.8. Pore-scale phenomena in VAPEX interfaces: capillary effect, snap-off, and advancing terminal meniscus (a) simulation results at time = 2950 s; (b) experimental observations (Chatzis, 2002).

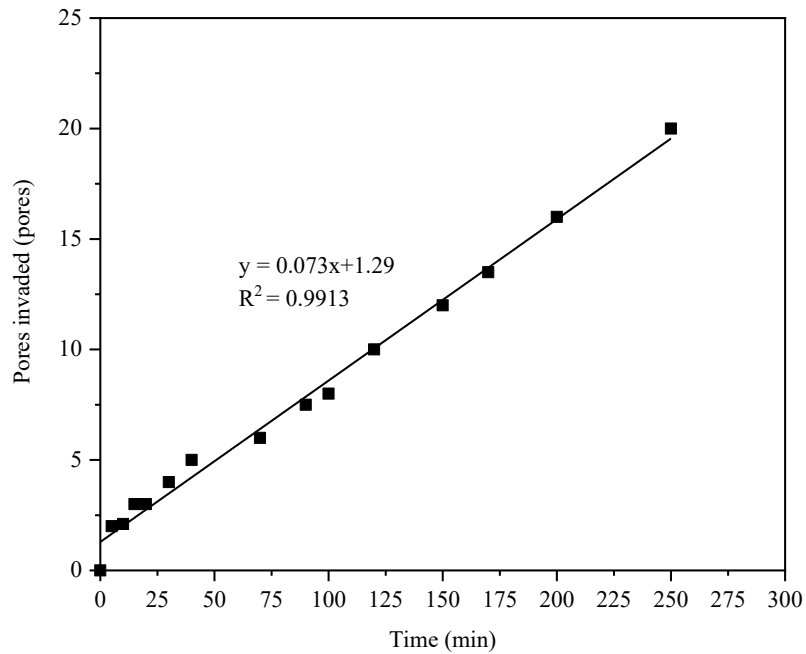


Figure 6.9. VAPEX interface advancement in micromodel.

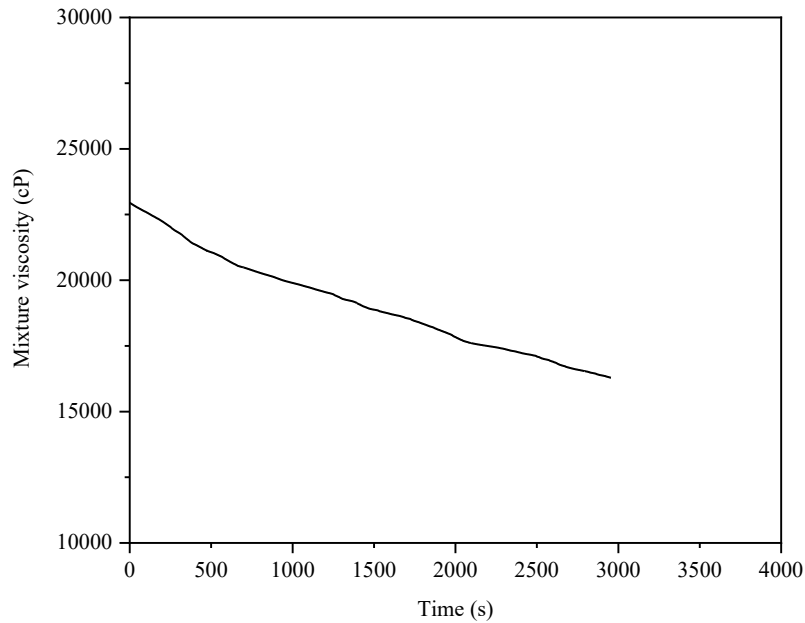


Figure 6.10. Evolution of the average oil viscosity within the porous medium during the VAPEX process.

Figure 6.9 shows the advancement of the bitumen/solvent interface over time. Except for the earlier time, the interface movement's velocity is linear with time. The general trend of the interface movement is consistent with the experimental results provided by James (2019). However, the simulation results of the interface movement are faster than the experimental observations. The main reason behind that is the incompressible system assumed in our simulation works. The evolution of the average oil viscosity within the porous medium can be evaluated based on the simulation results, as shown in Figure 6.10.

6.7 Summary

In this chapter, a pore-scale mathematical was proposed to simulate the interphase mass transfer phenomena of the VAPEX process at the pore-scale level and compared with

Chatzis's (2002) and James's (2009) experimental works. There are several conclusions that can be drawn from the VAPEX simulation works:

The proposed model can accurately capture VAPEX pore-scale phenomena (e.g., capillary effect, snap-off mechanisms, and the wettability effect), which is also consistent with experimental observations.

Based on the simulation results, the bitumen/solvent interface advancement is linear with time. The interface movement is essentially at constant velocity except for the zones when they reach the domain boundaries.

CHAPTER 7 : CONCLUSION AND FUTURE WORK

7.1 Summary and Conclusions

The main objective of this research is to investigate the main mass transfer mechanisms of the vapor solvent extraction recovery process at the pore-scale level. The primary objective of the proposed pore-scale model is to simulate the interphase mass transfer during the immiscible process. Moreover, this model aims to incorporate new interfacial knowledge to explain the pore-scale observations during the VAPEX process.

A simulation framework (LS-CST) has been proposed to investigate the multicomponent interphase mass transfer at the pore-scale level. The LS-CST model is based on the conservative level-set method, coupled with the continuous species transfer model, including the interfacial boundary conditions (flux continuity and concentration jump at the interface). To solve the sets of partial differential equations, the commercial finite-element-based solver COMSOL Multiphysics (COMSOL, 2019) is applied. The primary capabilities of the proposed model include:

1. This model can simulate dynamic mass transfer across the interface in a complex porous medium. Compared with other pore-scale methods, our methods solve the computational domain directly using the finite-element method.
2. The model can be used to investigate the mass transfer in a two-phase flow, and the related macro-scale mass transfer coefficient can be obtained from the simulation results.
3. The proposed model can serve as a tool to examine the different mechanisms, interactions, and relative importance under various conditions.

Key mechanisms, including the diffusion, convection, and capillary effect, are incorporated in this model. Some of the key findings from the proposed LS-CST modeling are summarized below:

1. It was observed that numerical instability arises when simulating the high flow rates or when the diffusion coefficients of species are very small. The suggested simplest way is to introduce an artificial diffusive term as a function of mesh size to maintain numerical stability. Thus, a reasonable stabilization method needs to balance the computational efforts and model accuracy.
2. We used the proposed numerical framework to simulate the vaporized solvent displacement process in a real sandstone pore space. The simulation results are used to upscale the mass transfer coefficient that corresponds to a REV scale. It revealed that a single value of the average mass transfer coefficient can be evaluated for a given pore-scale model. Indeed, the information about the probability distribution of the results for different pores distribution realizations provides a way to evaluate the uncertainty due to heterogeneity at the reservoir scale.

A consistent interphase mass transfer was developed with an additional compressive term, named LS-C-CST, retrieved from the conservative level-set equation. Compared to the additional diffusive term method, the novelty of this new interphase mass transfer model is that the compressive term is derived from the consistent conservative LS equation. The LS-C-CST method can be used to solve the convective-dominated regime ($Pe > 1$) with high accuracy to capture the concentration jump at the interface. Indeed, the general contribution of the proposed solver (LS-C-CST) is that it can be broadly applied in the context of multiphase fluid flow interphase mass transfer phenomena in numerous subsurface flow

applications. Some case studies have been performed to investigate mass transfer in a 2D cavity under various conditions. The conclusions are listed as follows:

1. Due to the momentum transmitted by the following non-wetting phase, we observed the recirculation motion inside the immobile dead-end pores of the wetting phase, which is also consistent with the experimental observations. Compared with the different viscosity ratio cases, a better mixing in the wetting phase (trapped zone) corresponding to a larger interfacial can be computed in the convection-dominated regime.
2. In the 2D micromodel, the average velocity within the trapped zone has a linear relationship with the natural logarithm of the viscosity ratio.
3. In the case of the 2D cavity study, the upscaled mass transfer coefficient exhibits different conditions and reaches a constant value after a certain period of time.

This work aims to develop pore-level mathematical modeling to capture the main mass transfer mechanisms in the VAPEX process. The proposed LS-C-CST is employed to achieve this. The conclusions are listed below:

1. Once communication is built between the line source of the solvent and bitumen, the solvent/bitumen interface advances into the dead oil zone (except for the boundary near the area) at a constant velocity. The simulation results of the interface velocity also show the same trend but with a higher value. The reason for this, as well as the limitation of this model, is that the incompressible system is assumed.
2. Mass transfer during the VAPEX process is by diffusion and convection. The diluted oil drains under the gravity effect once it overcomes the capillary and viscous effects.

3. Some of the pore-scale phenomena, including solvents trapped by the snap-off mechanisms, terminal meniscus, and interface at the pore throat, can be observed in our simulation works. Indeed, the simulation results confirm that the mass transfer is not diffusion during the vapor solvent extraction process.
4. *In-situ* asphaltene precipitation is an important phenomenon during the VAPEX process. Asphaltene removal from bitumen is one of the effective techniques for reducing heavy oil viscosity. Due to the complexity of the asphaltene precipitation and the capacity of the proposed formulation (phase change including (liquid phase to solid phase)), we ignored this phenomenon. This is another limitation of this model.
5. The pore-scale simulation showed that the solvent diffusion alone cannot reduce the heavy oil viscosity effectively, even in a small micromodel work. It is indicated that the thermodynamic equilibrium at interface assumption may not be suitable for the VAPEX process.

7.2 Recommendations for Future Work

Based on the results of this thesis and the limitations of the proposed model, I make some recommendations for future work from three different perspectives: (1) more comprehensive pore-scale formulation include phase change; (2) incorporate the equation of states (EOS); (3) conducting condensing solvent include heat transfer. In specific, the recommendations are:

1. The proposed numerical model, LS-C-CST, does not include phase changes within the porous medium. Modeling the phase changes involves the transition between different states of matter (e.g., gas phase to liquid, liquid to solid phase), which is a complex

- phase behavior. It is recommended to involve a second interface track equation with a mass transfer term between the interfaces for each phase, respectively. In addition, it is also recommended that the mass transfer term be expressed as a function of the temperature and pressure, which may help to characterize the effect of the phase changes.
2. During the solvent-assisted process, the vapor solvents may condense on the bitumen interface at a certain condition. The experimental observations show that the solvent condenses may enhance the convective mixing and increase the interface movement (James, 2009). Thus, it is recommended that the fluid mixing and phase changes be governed dynamically by equations of state at the pore scale. Asphaltene precipitation phenomena in the VAPEX process could be incorporated into the pore-scale model with coupled equations of state.
 3. It is recommended to couple the convection-conduction heat transfer governing equation to simulate the heat transfer during the warm VAPEX process or any solvent-assisted recovery process. Viscosity reduction of heavy oil can be achieved by thermally (heating) and mass transfer (solvent dilution). Thus, one possible approach to investigate the mechanisms for this heated VAPEX process is to develop a coupled heat transfer and interphase mass transfer model to simulate the heat and mass transfer effects on the heavy oil properties during the extraction process.
 4. The simulation results in the VAPEX micromodel indicate that the instantaneous equilibrium assumption at the interface may not be valid. The viscosity reduction of the heavy oil process caused by solvent diffusion and convection is a long-term process that takes time to reach equilibrium. For future work, it is necessary to couple a time-

dependent non-equilibrium constant (as a function of pressure and temperature) to capture the interface mass transfer. The corresponding upscaling parameters may help us to have a more accuracy field scale model.

BIBLIOGRAPHY

- Afshari, S., Hejazi, S. H., & Kantzas, A. (2018). Role of medium heterogeneity and viscosity contrast in miscible flow regimes and mixing zone growth: A computational pore-scale approach. *Physical Review Fluids*, 3(5), 054501.
- Agaoglu, B., Coptý, N. K., Scheytt, T., & Hinkelmann, R. (2015). Interphase mass transfer between fluids in subsurface formations: A review. *Advances in Water Resources*, 79, 162-194.
- Agaoglu, B., Scheytt, T., & Coptý, N. K. (2016). Impact of NAPL architecture on interphase mass transfer: A pore network study. *Advances in Water Resources*, 95, 138-151.
- Agertz, O., Moore, B., Stadel, J., Potter, D., Miniati, F., Read, J., ... & Walder, R. (2007). Fundamental differences between SPH and grid methods. *Monthly Notices of the Royal Astronomical Society*, 380(3), 963-978.
- Ali, S. F. (2003). Heavy oil—evermore mobile. *Journal of Petroleum science and Engineering*, 37(1-2), 5-9.
- Alikhan, A. A., & Ali, S. M. (1974). Heavy oil recovery by steam-driven hydrocarbon slugs from linear porous media. In *Fall Meeting of the Society of Petroleum Engineers of AIME*. OnePetro.
- Allen, J. C. (1974). Gaseous solvent heavy oil recovery. *Canadian Patent*, 446874.
- Allen, J. C., & Redford, D. A. (1978). *Combination solvent-noncondensable gas injection method for recovering petroleum from viscous petroleum-containing formations including tar sand deposits* (No. US 4109720).

- Alpak, F. O., Riviere, B., & Frank, F. (2016). A phase-field method for the direct simulation of two-phase flows in pore-scale media using a non-equilibrium wetting boundary condition. *Computational Geosciences*, 20(5), 881-908.
- Aminnaji, M., Rabbani, A., J. Niasar, V., & Babaei, M. (2019). Effects of pore-scale heterogeneity on macroscopic NAPL dissolution efficiency: A two-scale numerical simulation study. *Water Resources Research*, 55(11), 8779-8799.
- An, S., Hasan, S., Erfani, H., Babaei, M., & Niasar, V. (2020). Unravelling effects of the pore-size correlation length on the two-phase flow and solute transport properties: GPU-based pore-network modeling. *Water Resources Research*, 56(8), e2020WR027403.
- Andrew, M., Bijeljic, B., & Blunt, M. J. (2013). Pore-scale imaging of geological carbon dioxide storage under in situ conditions. *Geophysical Research Letters*, 40(15), 3915-3918.
- Andriianova, E., Leung, J.Y. A Statistical Upscaling Workflow for Warm Solvent Injection Processes for Heterogeneous Heavy Oil Reservoirs. *Nat Resour Res* 30, 4417–4437 (2021). <https://doi.org/10.1007/s11053-021-09921-6>
- Ardali, M., Barrufet, M. A., Mamora, D. D., & Qiu, F. (2012, October). A critical review of hybrid steam-solvent processes to recover heavy oil. In *SPE Annual Technical Conference and Exhibition?* (pp. SPE-159257). SPE.
- Armstrong, R. T., & Wildenschild, D. (2012). Investigating the pore-scale mechanisms of microbial enhanced oil recovery. *Journal of Petroleum Science and Engineering*, 94, 155-164.

- Basirat, F., Yang, Z., & Niemi, A. (2017). Pore-scale modeling of wettability effects on CO₂-brine displacement during geological storage. *Advances in water resources*, 109, 181-195.
- Bayestehparvin, B., Farouq Ali, S. M., Kariznovi, M., & Abedi, J. (2021). Pore-scale modelling of solvent-based recovery processes. *Energies*, 14(5), 1405.
- Beers, K. J. (2007). Numerical methods for chemical engineering: applications in Matlab. Cambridge University Press.
- Benzi, R., Succi, S., & Vergassola, M. (1992). The lattice Boltzmann equation: theory and applications. *Physics Reports*, 222(3), 145-197.
- Blunt, M. J., Bijeljic, B., Dong, H., Gharbi, O., Iglauer, S., Mostaghimi, P., ... & Pentland, C. (2013). Pore-scale imaging and modelling. *Advances in Water resources*, 51, 197-216.
- Blunt, M. J., Jackson, M. D., Piri, M., & Valvatne, P. H. (2002). Detailed physics, predictive capabilities and macroscopic consequences for pore-network models of multiphase flow. *Advances in Water Resources*, 25(8-12), 1069-1089.
- Blunt, M., & King, P. (1991). Relative permeabilities from two-and three-dimensional pore-scale network modelling. *Transport in porous media*, 6, 407-433.
- Boustani, A., & Maini, B. B. (2001). The role of diffusion and convective dispersion in vapour extraction process. *Journal of Canadian Petroleum Technology*, 40(04).
- Bowman, C. W. (1967, April). Molecular and interfacial properties of Athabasca tar sands. In *World Petroleum Congress* (pp. WPC-12257). WPC.
- Brackbill, J. U., Kothe, D. B., & Zemach, C. (1992). A continuum method for modeling surface tension. *Journal of computational physics*, 100(2), 335-354.

- Butler, R. M., & Mokrys, I. J. (1991). A new process (VAPEX) for recovering heavy oils using hot water and hydrocarbon vapour. *Journal of Canadian Petroleum Technology*, 30(01).
- Butler, R. M., & Mokrys, I. J. (1991). A new process (VAPEX) for recovering heavy oils using hot water and hydrocarbon vapour. *Journal of Canadian Petroleum Technology*, 30(01).
- Butler, R.M. and Mokrys, I.J. (1989). The Rise of Interfering Solvent Chambers: Solvent Analog Model of Steam Assisted Gravity Drainage. *Journal of Canadian Petroleum Technology*, 32(3).
- Chatzis, I. (2002). Pore scale phenomena of heavy oil recovery using vapor extraction. *SCA2002-26*.
- Chen, P., Harmand, S., Ouenzerfi, S., & Schiffler, J. (2017). Marangoni flow induced evaporation enhancement on binary sessile drops. *The Journal of Physical Chemistry B*, 121(23), 5824-5834.
- Chevalier, L. (2019). Accounting for capillary effects in level-set based Finite Elements modelling of impregnation in fibrous media (Doctoral dissertation, Université de Lyon).
- Chomsurin, C., & Werth, C. J. (2003). Analysis of pore-scale nonaqueous phase liquid dissolution in etched silicon pore networks. *Water resources research*, 39(9).
- COMSOL 6.0. COMSOL online documentation; 2021.
- COMSOL, C. M. (2019). 5.5 User's Guide. COMSOL Inc.

- Dani, A., Guiraud, P., & Cockx, A. (2007). Local measurement of oxygen transfer around a single bubble by planar laser-induced fluorescence. *Chemical Engineering Science*, 62(24), 7245-7252.
- Das, S. (2005, November). Diffusion and Dispersion in the Simulation of VAPEX Process. In *SPE International Thermal Operations and Heavy Oil Symposium* (pp. SPE-97924). SPE.
- Azin, R., Kharrat, R., Ghotbi, C., & Vossoughi, S. (2005, March). Applicability of the VAPEX process to Iranian heavy oil reservoirs. In *SPE Middle East Oil and Gas Show and Conference* (pp. SPE-92720). SPE.
- Das, S. K. (1997). In situ recovery of heavy oil and bitumen using vaporized hydrocarbon solvents.
- Das, S. K. (1998). Vapex: An efficient process for the recovery of heavy oil and bitumen. *SPE journal*, 3(03), 232-237.
- Das, S. K., & Butler, R. M. (1996). Countercurrent extraction of heavy oil and bitumen. In *International Conference on Horizontal Well Technology*. OnePetro.
- Das, S. K., & Butler, R. M. (1998). Mechanism of the vapor extraction process for heavy oil and bitumen. *Journal of Petroleum Science and Engineering*, 21(1-2), 43-59.
- Das, S. K., & Butler, R. M. (1998). Mechanism of the vapor extraction process for heavy oil and bitumen. *Journal of Petroleum Science and Engineering*, 21(1-2), 43-59.
- Das, S.K. (1995). In Situ Recovery of Heavy Oil and Bitumen Using Vapourized Hydrocarbon Solvents, Ph.D. Dissertation, University of Calgary, Calgary, AB, Canada.

- Deen, W. M. (1998). Analysis of transport phenomena (Vol. 2). New York: Oxford university press.
- Deising, D., Marschall, H., & Bothe, D. (2016). A unified single-field model framework for volume-of-fluid simulations of interfacial species transfer applied to bubbly flows. *Chemical Engineering Science*, 139, 173-195.
- Dillard, L. A., & Blunt, M. J. (2000). Development of a pore network simulation model to study nonaqueous phase liquid dissolution. *Water Resources Research*, 36(2), 439-454.
- Engberg, R. F., Wegener, M., & Kenig, E. Y. (2014). The impact of Marangoni convection on fluid dynamics and mass transfer at deformable single rising droplets—A numerical study. *Chemical Engineering Science*, 116, 208-222.
- Engberg, R. F., Wegener, M., & Kenig, E. Y. (2014). The influence of Marangoni convection on fluid dynamics of oscillating single rising droplets. *Chemical Engineering Science*, 117, 114-124.
- Fayazi, A., & Kantzas, A. (2019). Determining diffusivity, solubility, and swelling in gaseous solvent–heavy oil systems. *Industrial & Engineering Chemistry Research*, 58(23), 10031-10043.
- Fayazi, A., & Kantzas, A. (2019). Determining diffusivity, solubility, and swelling in gaseous solvent–heavy oil systems. *Industrial & Engineering Chemistry Research*, 58(23), 10031-10043.
- Fayazi, A., & Kantzas, A. (2019). Determining diffusivity, solubility, and swelling in gaseous solvent–heavy oil systems. *Industrial & Engineering Chemistry Research*, 58(23), 10031-10043.

- Ferrari, A., & Lunati, I. (2013). Direct numerical simulations of interface dynamics to link capillary pressure and total surface energy. *Advances in water resources*, 57, 19-31.
- Fleckenstein, S., & Bothe, D. (2015). A volume-of-fluid-based numerical method for multicomponent mass transfer with local volume changes. *Journal of Computational Physics*, 301, 35-58.
- Francois, J., Dietrich, N., Guiraud, P., & Cockx, A. (2011). Direct measurement of mass transfer around a single bubble by micro-PLIFI. *Chemical Engineering Science*, 66(14), 3328-3338.
- Ganguli, A. A., & Kenig, E. Y. (2011). A CFD-based approach to the interfacial mass transfer at free gas-liquid interfaces. *Chemical engineering science*, 66(14), 3301-3308.
- Gao, H., Tatomir, A. B., Karadimitriou, N. K., Steeb, H., & Sauter, M. (2021). A two-phase, pore-scale reactive transport model for the kinetic interface-sensitive tracer. *Water Resources Research*, 57(6), e2020WR028572.
- Ghanavati, M., Hassanzadeh, H., & Abedi, J. (2014). Application of Taylor dispersion technique to measure mutual diffusion coefficient in hexane+ bitumen system. *AIChE Journal*, 60(7), 2670-2682.
- Golparvar, A., Zhou, Y., Wu, K., Ma, J., & Yu, Z. (2018). A comprehensive review of pore scale modeling methodologies for multiphase flow in porous media. *Advances in Geo-Energy Research*, 2(4), 418-440.
- Gopala, V. R., & Van Wachem, B. G. (2008). Volume of fluid methods for immiscible-fluid and free-surface flows. *Chemical Engineering Journal*, 141(1-3), 204-221.

- Gostick, J., Aghighi, M., Hinebaugh, J., Tranter, T., Hoeh, M. A., Day, H., ... & Putz, A. (2016). OpenPNM: a pore network modeling package. *Computing in Science & Engineering*, 18(4), 60-74.
- Graveleau, M., Soullaine, C., & Tchelepi, H. A. (2017). Pore-scale simulation of interphase multi-component mass transfer for subsurface flow. *Transport in porous media*, 120(2), 287-308.
- Graveleau, M., Soullaine, C., & Tchelepi, H. A. (2017). Pore-scale simulation of interphase multicomponent mass transfer for subsurface flow. *Transport in porous media*, 120, 287-308.
- Groothuis, H., & Zuiderweg, F. J. (1960). Influence of mass transfer on coalescence of drops. *Chemical Engineering Science*, 12(4), 288-289.
- Guo, Z., & Zheng, C. (2008). Analysis of lattice Boltzmann equation for microscale gas flows: relaxation times, boundary conditions and the Knudsen layer. *International Journal of Computational Fluid Dynamics*, 22(7), 465-473.
- Haggerty, R., & Gorelick, S. M. (1995). Multiple-rate mass transfer for modeling diffusion and surface reactions in media with pore-scale heterogeneity. *Water Resources Research*, 31(10), 2383-2400.
- Haghighat, P., & Maini, B. B. (2008, June). Role of asphaltene precipitation in VAPEX process. In *Canadian International Petroleum Conference*. OnePetro.
- Haghighat, P., & Maini, B. B. (2010). Role of asphaltene precipitation in VAPEX process. *Journal of Canadian Petroleum Technology*, 49(03), 14-21.
- Haghighat, P., & Maini, B. B. (2010). Role of asphaltene precipitation in VAPEX process. *Journal of Canadian Petroleum Technology*, 49(03), 14-21.

- Haroun, Y., Legendre, D., & Raynal, L. (2010a). Volume of fluid method for interfacial reactive mass transfer: Application to stable liquid film. *Chemical Engineering Science*, 65(10), 2896-2909.
- Haroun, Y., Legendre, D., & Raynal, L. (2010b). Direct numerical simulation of reactive absorption in gas–liquid flow on structured packing using interface capturing method. *Chemical Engineering Science*, 65(1), 351-356.
- Hartmann, D., Meinke, M., & Schröder, W. (2010). The constrained reinitialization equation for level set methods. *Journal of computational physics*, 229(5), 1514-1535.
- Held, R. J., & Celia, M. A. (2001). *Pore-scale modeling extension of constitutive relationships in the range of residual saturations* (Vol. 37, No. 1, pp. 165-170).
- Hui, M. H., & Blunt, M. J. (2000). Effects of wettability on three-phase flow in porous media. *The Journal of Physical Chemistry B*, 104(16), 3833-3845.
- Irani, M., & Gates, I. (2013). Understanding the Convection Heat-Transfer Mechanism in the Steam-Assisted-Gravity-Drainage Process. *SPE Journal*, 18(06), 1202-1216.
- Istchenko, C. M., & Gates, I. D. (2014). Well/wormhole model of cold heavy-oil production with sand. *Spe Journal*, 19(02), 260-269.
- James, L. (2009). Mass transfer mechanisms during the solvent recovery of heavy oil.
- James, L. A., & Chatzis, I. (2004a). VAPEX: mass transfer and gravity drainage in porous media.
- James, L. A., & Chatzis, I. (2007, June). Mass transfer coefficients in vapour extraction (VAPEX). In *Canadian International Petroleum Conference*. OnePetro.

- James, L. A., Rezaei, N., & Chatzis, I. V. A. P. E. X. (2008). VAPEX, warm VAPEX and hybrid VAPEX-the state of enhanced oil recovery for in situ heavy oils in Canada. *Journal of Canadian Petroleum Technology*, 47(04).
- James, L., & Chatzis, I. (2004b). Details of gravity drainage of heavy oil during vapor extraction. *Dimensions*, 3(2), 4.
- Jettestuen, E., Helland, J. O., & Prodanović, M. (2013). A level set method for simulating capillary-controlled displacements at the pore scale with nonzero contact angles. *Water Resources Research*, 49(8), 4645-4661.
- Jia, C., Shing, K., & Yortsos, Y. C. (1999). Visualization and simulation of non-aqueous phase liquids solubilization in pore networks. *Journal of Contaminant Hydrology*, 35(4), 363-387.
- Jiang, Q., Yuan, J. Y., Russel-Houston, J., Thornton, B., & Squires, A. (2010). Evaluation of recovery technologies for the Grosmont carbonate reservoirs. *Journal of Canadian Petroleum Technology*, 49(05), 56-64.
- Joekar-Niasar, V., & Hassanizadeh, S. M. (2012). Analysis of fundamentals of two-phase flow in porous media using dynamic pore-network models: A review. *Critical reviews in environmental science and technology*, 42(18), 1895-1976.
- Johns, M. L., & Gladden, L. F. (1999). Magnetic resonance imaging study of the dissolution kinetics of octanol in porous media. *Journal of colloid and interface science*, 210(2), 261-270.
- Johns, M. L., & Gladden, L. F. (2000). Probing ganglia dissolution and mobilization in a water-saturated porous medium using MRI. *Journal of colloid and interface science*, 225(1), 119-127.

- Kelder, O., & Smeulders, D. M. (1997). Observation of the Biot slow wave in water-saturated Nivelsteiner sandstone. *Geophysics*, 62(6), 1794-1796.
- Khalifa, M., & Lue, L. (2017). A group contribution method for predicting the solubility of mercury. *Fluid Phase Equilibria*, 432, 76-84.
- Khenner, M., Averbuch, A., Israeli, M., & Nathan, M. (2001). Numerical simulation of grain-boundary grooving by level set method. *Journal of Computational Physics*, 170(2), 764-784.
- Koval, E. (1963). A method for predicting the performance of unstable miscible displacement in heterogeneous media. *Society of Petroleum Engineers Journal*, 3(02), 145-154.
- Lake, L. W. (1989). Enhanced oil recovery.
- Lam, A. C., Schechter, R. S., & Wade, W. H. (1983). Mobilization of residual oil under equilibrium and nonequilibrium conditions. *Society of Petroleum Engineers Journal*, 23(05), 781-790.
- Leung, J. (2014). Scaleup of effective mass transfer in vapour-extraction process accounting for field-scale reservoir heterogeneities. *Journal of Canadian Petroleum Technology*, 53(05), 275-289.
- Leung, J. Y., & Srinivasan, S. (2011). Analysis of uncertainty introduced by scaleup of reservoir attributes and flow response in heterogeneous reservoirs. *SPE Journal*, 16(03), 713-724.
- Leung, J. Y., & Srinivasan, S. (2012). Scale-up of mass transfer and recovery performance in heterogeneous reservoirs. *Journal of Petroleum Science and Engineering*, 86, 71-86.

- Li, C., Huang, R., Ding, Z., Gatenby, J. C., Metaxas, D. N., & Gore, J. C. (2011). A level set method for image segmentation in the presence of intensity inhomogeneities with application to MRI. *IEEE transactions on image processing*, 20(7), 2007-2016.
- Li, X., Berg, S., Castellanos-Diaz, O., Wiegmann, A., & Verlaan, M. (2020). Solvent-dependent recovery characteristic and asphaltene deposition during solvent extraction of heavy oil. *Fuel*, 263, 116716.
- Li, X., Huang, H., & Meakin, P. (2010). A three-dimensional level set simulation of coupled reactive transport and precipitation/dissolution. *International Journal of Heat and Mass Transfer*, 53(13-14), 2908-2923.
- Lin, L., Zeng, F., & Gu, Y. (2014). A circular solvent chamber model for simulating the VAPEX heavy oil recovery process. *Journal of Petroleum Science and Engineering*, 118, 27-39.
- Liu, C., Liu, Y., Kerisit, S., & Zachara, J. (2015). Pore-scale process coupling and effective surface reaction rates in heterogeneous subsurface materials. *Reviews in Mineralogy and Geochemistry*, 80(1), 191-216.
- Luo, P., & Gu, Y. (2007). Effects of asphaltene content on the heavy oil viscosity at different temperatures. *Fuel*, 86(7-8), 1069-1078.
- Lyford, P. A., Pratt, H. R. C., Shallcross, D. C., & Grieser, F. (1998). The marangoni effect and enhanced oil recovery Part 1. Porous media studies. *The Canadian Journal of Chemical Engineering*, 76(2), 167-174.
- Ma, Z., & Leung, J. Y. (2018, March). Integration of data-driven models for characterizing shale barrier configuration in 3D heterogeneous reservoirs for SAGD operations. In *SPE Canada Heavy Oil Technical Conference*. OnePetro.

- Maes, J., & Menke, H. P. (2021). GeoChemFoam: Direct modelling of multiphase reactive transport in real pore geometries with equilibrium reactions. *Transport in Porous Media*, 139(2), 271-299.
- Maes, J., & Soullaine, C. (2018). A new compressive scheme to simulate species transfer across fluid interfaces using the volume-of-fluid method. *Chemical Engineering Science*, 190, 405-418.
- Maes, J., & Soullaine, C. (2020). A unified single-field Volume-of-Fluid-based formulation for multi-component interfacial transfer with local volume changes. *Journal of Computational Physics*, 402, 109024.
- Marschall, H. R., & Schumacher, J. C. (2012). Arc magmas sourced from mélange diapirs in subduction zones. *Nature Geoscience*, 5(12), 862-867.
- Marschall, H., Hinterberger, K., Schüller, C., Habla, F., & Hinrichsen, O. (2012). Numerical simulation of species transfer across fluid interfaces in free-surface flows using OpenFOAM. *Chemical engineering science*, 78, 111-127.
- Meakin, P., & Tartakovsky, A. M. (2009). Modeling and simulation of pore-scale multiphase fluid flow and reactive transport in fractured and porous media. *Reviews of Geophysics*, 47(3).
- Mehmani, Y., & Tchelepi, H. A. (2019). Multiscale formulation of two-phase flow at the pore scale. *Journal of Computational Physics*, 389, 164-188.
- Menke, H. P., Bijeljic, B., Andrew, M. G., & Blunt, M. J. (2015). Dynamic three-dimensional pore-scale imaging of reaction in a carbonate at reservoir conditions. *Environmental science & technology*, 49(7), 4407-4414.

- Miller, C. T., Poirier-McNeil, M. M., & Mayer, A. S. (1990). Dissolution of trapped nonaqueous phase liquids: Mass transfer characteristics. *Water Resources Research*, 26(11), 2783-2796.
- Moghadam, S., Nobakht, M., & Gu, Y. (2009). Theoretical and physical modeling of a solvent vapour extraction (VAPEX) process for heavy oil recovery. *Journal of Petroleum Science and Engineering*, 65(1-2), 93-104.
- Mohammadzadeh, O., Rezaei, N., & Chatzis, I. (2010). Pore-level investigation of heavy oil and Bitumen recovery using solvent- aided steam assisted gravity drainage (SA-SAGD) process. *Energy & Fuels*, 24(12), 6327-6345.
- Mokrys, I. J., & Butler, R. M. (1993, March). In-situ upgrading of heavy oils and bitumen by propane deasphalting: the VAPEX process. In *SPE Oklahoma City Oil and Gas Symposium/Production and Operations Symposium* (pp. SPE-25452). SPE.
- Molins, S., & Knabner, P. (2019). Multiscale approaches in reactive transport modeling. *Reviews in Mineralogy and Geochemistry*, 85(1), 27-48.
- Mworia, M. R., Wu, Z., Shu, K., Jiang, S., Gou, Q., Chen, Z., & Said, A. A. (2024). A review of VAPEX recovery technique: Mechanisms, driving models uncertainties, and enhancement factors analysis. *Fuel*, 361, 130645.
- Nenniger, E. H. (1979). Hydrocarbon recovery.
- Nenniger, J. E., & Dunn, S. G. (2008, June). How fast is solvent based gravity drainage?. In *PETSOC Canadian International Petroleum Conference* (pp. PETSOC-2008). PETSOC.
- Nenniger, J., & Nenniger, E. (2005). *U.S. Patent No. 6,883,607*. Washington, DC: U.S. Patent and Trademark Office.

- Ohser, S., & Sethian, J. A. (1988). Front Propagating with Curvature Dependent Speed: Algorithms Based on Hamilton-Jacobi Formulations. *J. Comput Phys*, 1988, 79, 12-49.
- Olsson, E., & Kreiss, G. (2005). A conservative level set method for two phase flow. *Journal of computational physics*, 210(1), 225-246.
- Olsson, E., Kreiss, G., & Zahedi, S. (2007). A conservative level set method for two phase flow II. *Journal of Computational Physics*, 225(1), 785-807.
- Perkins, T. K., & Johnston, O. (1963). A review of diffusion and dispersion in porous media. *Society of Petroleum Engineers Journal*, 3(01), 70-84.
- Pourabdollah, K., & Mokhtari, B. (2013). The VAPEX process, from beginning up to date. *Fuel*, 107, 1-33.
- Pourabdollah, K., & Mokhtari, B. (2013). The VAPEX process, from beginning up to date. *Fuel*, 107, 1-33.
- Pratt, H. R. C. (1991, November). Marangoni flooding with water drives: A novel method for EOR?. In *SPE Asia Pacific Oil and Gas Conference and Exhibition* (pp. SPE-22982). SPE.
- Qi, Z., Abedini, A., Lele, P., Mosavat, N., Guerrero, A., & Sinton, D. (2017). Pore-scale analysis of condensing solvent bitumen extraction. *Fuel*, 193, 284-293.
- Rostami, B., Etminan, S. R., Soleimani, A., & Kharrat, R. (2007, June). Effect of Capillarity and Surface Tension on the performance of VAPEX Process. In *PETSOC Canadian International Petroleum Conference* (pp. PETSOC-2007). PETSOC.

- Sagiv, A., Christofides, P. D., Cohen, Y., & Semiat, R. (2015). On the analysis of FO mass transfer resistances via CFD analysis and film theory. *Journal of Membrane Science*, 495, 198-205.
- Saraf, S., & Bera, A. (2021). A review on pore-scale modeling and CT scan technique to characterize the trapped carbon dioxide in impermeable reservoir rocks during sequestration. *Renewable and Sustainable Energy Reviews*, 144, 110986.
- Sarikurt, D. A., Gokdemir, C., & Coptu, N. K. (2017). Sherwood correlation for dissolution of pooled NAPL in porous media. *Journal of contaminant hydrology*, 206, 67-74.
- Schenk, O., & Gärtner, K. (2004). Solving unsymmetric sparse systems of linear equations with PARDISO. *Future Generation Computer Systems*, 20(3), 475-487.
- Shi, J., & Leung, J. Y. (2013, June). Physics-based proxy for vapex process modeling in heterogeneous reservoirs. In *SPE Canada Heavy Oil Conference* (pp. SPE-165558). SPE.
- Shi, J., & Leung, J. Y. (2014). Semi-analytical proxy for vapex process modeling in heterogeneous reservoirs. *Journal of Energy Resources Technology*, 136(3), 032904.
- Singhal, A. K., Das, S. K., Leggitt, S. M., Kasraie, M., & Ito, Y. (1996, November). Screening of reservoirs for exploitation by application of steam assisted gravity drainage/vapex processes. In *International Conference on Horizontal Well Technology*. OnePetro.
- So, K. K., Hu, X. Y., & Adams, N. A. (2011). Anti-diffusion method for interface steepening in two-phase incompressible flow. *Journal of Computational Physics*, 230(13), 5155-5177.
- Söderlind, G., & Wang, L. (2006). Adaptive time-stepping and computational stability. *Journal of Computational and Applied Mathematics*, 185(2), 225-243.

- Soll, W. E., Celia, M. A., & Wilson, J. (1993). Micromodel studies of three-fluid porous media systems: Pore-scale processes relating to capillary pressure-saturation relationships. *Water resources research*, 29(9), 2963-2974.
- Sorensen, T. S. (1980). Marangoni phenomena at a spherical interface. *JCS Faraday II*, 76(1), 170-1.
- Soulaine, C., Debenest, G., & Quintard, M. (2011). Upscaling multi-component two-phase flow in porous media with partitioning coefficient. *Chemical Engineering Science*, 66(23), 6180-6192.
- Soulaine, C., Debenest, G., & Quintard, M. (2011). Upscaling multicomponent two-phase flow in porous media with partitioning coefficient. *Chemical Engineering Science*, 66(23), 6180-6192.
- Sternling, C. A., & Scriven, L. E. (1959). Interfacial turbulence: hydrodynamic instability and the Marangoni effect. *AIChE Journal*, 5(4), 514-523.
- Sun, D. L., & Tao, W. Q. (2010). A coupled volume-of-fluid and level set (VOSET) method for computing incompressible two-phase flows. *International Journal of Heat and Mass Transfer*, 53(4), 645-655.
- Sussman, M., & Puckett, E. G. (2000). A coupled level set and volume-of-fluid method for computing 3D and axisymmetric incompressible two-phase flows. *Journal of computational physics*, 162(2), 301-337.
- Sussman, M., Almgren, A. S., Bell, J. B., Colella, P., Howell, L. H., & Welcome, M. L. (1999). An adaptive level set approach for incompressible two-phase flows. *Journal of Computational Physics*, 148(1), 81-124.

- Tafuni, A., De Giorgi, M. G., & De Rosis, A. (2021). Smoothed Particle Hydrodynamics vs Lattice Boltzmann for the solution of steady and unsteady fluid flows. *Computational Particle Mechanics*, 1-23.
- Taheri, S., Kantzas, A., & Abedi, J. (2010, October). Mass diffusion into bitumen: A sub-pore scale modeling approach. In *SPE Canada Unconventional Resources Conference?* (pp. SPE-138129). SPE.
- Transport phenomena, R. B. Bird, W. E. Stewart, and E. N. Lightfoot, John Wiley and Sons, Inc., New York (1960). 780 pages.
- Trebotich, D., & Graves, D. (2015). An adaptive finite volume method for the incompressible Navier–Stokes equations in complex geometries. *Communications in Applied Mathematics and Computational Science*, 10(1), 43-82.
- Upreti, S. R., Lohi, A., Kapadia, R. A., & El-Haj, R. (2007). Vapor extraction of heavy oil and bitumen: a review. *Energy & Fuels*, 21(3), 1562-1574.
- van Dijk, R. E., Kaden, J. C., Argüelles-Ticó, A., Dawson, D. A., Burke, T., & Hatchwell, B. J. (2014). Cooperative investment in public goods is kin directed in communal nests of social birds. *Ecology letters*, 17(9), 1141-1148.
- Van Vranken, J. G., Li, J., Mitchell, D. C., Navarrete-Perea, J., & Gygi, S. P. (2021). Assessing target engagement using proteome-wide solvent shift assays. *Elife*, 10, e70784.
- Vishal, V., Leung, J.Y. (2017). A multi-scale particle-tracking framework for dispersive solute transport modeling. *Computational Geosciences* 22(2): 485–503.

- Wang, J., Yang, C., & Mao, Z. (2008). Numerical simulation of Marangoni effects of single drops induced by interphase mass transfer in liquid-liquid extraction systems by the level set method. *Science in China Series B: Chemistry*, 51(7), 684-694.
- Wang, Q., Jia, X., & Chen, Z. (2016). Mathematical modeling of the solvent chamber evolution in a vapor extraction heavy oil recovery process. *Fuel*, 186, 339-349.
- Wang, T. S., Shi, W. Y., & Duan, F. (2022). Marangoni convection instabilities in an evaporating droplet on a non-isothermal substrate. *International Journal of Heat and Mass Transfer*, 195, 123140.
- Washburn, E. W. (1921). The dynamics of capillary flow. *Physical review*, 17(3), 273.
- Wegener, M., & Paschedag, A. R. (2011). Mass transfer enhancement at deformable droplets due to Marangoni convection. *International journal of multiphase flow*, 37(1), 76-83.
- Wegener, M., Fevre, M., Paschedag, A. R., & Kraume, M. (2009). Impact of Marangoni instabilities on the fluid dynamic behaviour of organic droplets. *International journal of heat and mass transfer*, 52(11-12), 2543-2551.
- Weller, H. G. (2008). A new approach to VOF-based interface capturing methods for incompressible and compressible flow. OpenCFD Ltd., Report TR/HGW, 4, 35.
- Xu, F., Hébrard, G., & Dietrich, N. (2020). Comparison of three different techniques for gas-liquid mass transfer visualization. *International Journal of Heat and Mass Transfer*, 150, 119261.
- Xu, J. J., Li, Z., Lowengrub, J., & Zhao, H. (2006). A level-set method for interfacial flows with surfactant. *Journal of Computational Physics*, 212(2), 590-616.

- Xu, L., Abedini, A., Qi, Z., Kim, M., Guerrero, A., & Sinton, D. (2018). Pore-scale analysis of steam-solvent coinjection: azeotropic temperature, dilution and asphaltene deposition. *Fuel*, 220, 151-158.
- Yaksi, K., Demiray, Z., & Coptu, N. K. (2021). Impact of cosolvents on the interphase mass transfer of NAPLs in porous media. *Water Resources Research*, 57(8), e2020WR029326.
- Yang, C., & Mao, Z. S. (2005). Numerical simulation of interphase mass transfer with the level set approach. *Chemical Engineering Science*, 60(10), 2643-2660.
- Yang, L., Dietrich, N., Loubière, K., Gourdon, C., & Hébrard, G. (2016). Visualization and characterization of gas–liquid mass transfer around a Taylor bubble right after the formation stage in microreactors. *Chemical Engineering Science*, 143, 364-368.
- Yang, L., Nieves-Remacha, M. J., & Jensen, K. F. (2017). Simulations and analysis of multiphase transport and reaction in segmented flow microreactors. *Chemical Engineering Science*, 169, 106-116.
- Yazdani, A. J., & Maini, B. B. (2005). Effect of drainage height and grain size on production rates in the VAPEX process: experimental study. *SPE Reservoir Evaluation & Engineering*, 8(03), 205-213.
- Yazdani, A. J., & Maini, B. B. (2005). Effect of drainage height and grain size on production rates in the VAPEX process: experimental study. *SPE Reservoir Evaluation & Engineering*, 8(03), 205-213.
- Ye, T., Phan-Thien, N., & Lim, C. T. (2016). Particle-based simulations of red blood cells—A review. *Journal of biomechanics*, 49(11), 2255-2266.

- Yin, Y., Qu, Z. G., & Zhang, J. F. (2019). Multiple diffusion mechanisms of shale gas in nanoporous organic matter predicted by the local diffusivity lattice Boltzmann model. *International Journal of Heat and Mass Transfer*, 143, 118571.
- Yiotis, A. G., Stubos, A. K., Boudouvis, A. G., & Yortsos, Y. C. (2001). A 2-D pore-network model of the drying of single-component liquids in porous media. *Advances in Water Resources*, 24(3-4), 439-460.
- Yiotis, A., Karadimitriou, N. K., Zarikos, I., & Steeb, H. (2021). Pore-scale effects during the transition from capillary-to viscosity-dominated flow dynamics within microfluidic porous-like domains. *Scientific Reports*, 11(1), 1-16.
- You, J., & Lee, K. J. (2022). Pore-Scale Numerical Investigations of the Impact of Mineral Dissolution and Transport on the Heterogeneity of Fracture Systems During CO₂-Enriched Brine Injection. *SPE Journal*, 27(02), 1379-1395.
- Yu, H., & Leung, J. Y. (2020). A sand-arch stability constrained dynamic fractal wormhole growth model for simulating cold heavy-oil production with sand. *SPE Journal*, 25(06), 3440-3456.
- Yu, H., & Leung, J. Y. (2023). Numerical pore-scale simulation of propane injection for heavy oil displacement processes. *International Journal of Multiphase Flow*, 159, 104319.
- Yu, H., Girimaji, S. S., & Luo, L. S. (2005). DNS and LES of decaying isotropic turbulence with and without frame rotation using lattice Boltzmann method. *Journal of Computational Physics*, 209(2), 599-616.

- Zaretskiy, Y., Geiger, S., Sorbie, K., & Förster, M. (2010). Efficient flow and transport simulations in reconstructed 3D pore geometries. *Advances in Water Resources*, 33(12), 1508-1516.
- Zhang, D., Du, X., Song, X., Wang, H., Li, X., Jiang, Y., & Wang, M. (2018). Application of the marangoni effect in nanoemulsion on improving waterflooding technology for heavy-oil reservoirs. *SPE Journal*, 23(03), 831-840.
- Zhao B, MacMinn CW, Primkulov BK, Chen Y, Valocchi AJ, Zhao J, Kang Q, Bruning K, McClure JE, Miller CT, Fakhari A.. (2019). Comprehensive comparison of pore-scale models for multiphase flow in porous media. *Proceedings of the National Academy of Sciences*, 116(28), 13799-13806.

Appendix A

For the one-dimensional analysis, the concentration of component i in each phase p with no convection is defined by Fick's second law:

$$\frac{\partial C_{p,i}}{\partial t} = D \frac{\partial^2 C_{p,i}}{\partial x^2} \quad (\text{A.1})$$

Here, we introduce the function $y = f(x, t) = \frac{x}{2\sqrt{Dt}}$ (A.2)

The partial derivatives of Equation. (A.2) are

$$\begin{aligned} \frac{\partial y}{\partial x} &= \frac{1}{2\sqrt{Dt}} \\ \frac{\partial y}{\partial t} &= -\frac{x}{4\sqrt{Dt^3}} \end{aligned} \quad (\text{A.3})$$

Dropping the subscript i for the sake of simplicity, the partial derivatives of C can be written as:

$$\begin{aligned} \frac{\partial C}{\partial t} &= -\frac{x}{4\sqrt{Dt^3}} \frac{dC}{dy} \\ \frac{\partial^2 C}{\partial x^2} &= \frac{1}{4Dt} \frac{d^2 C}{dy^2} \end{aligned} \quad (\text{A.4})$$

Substituting Equation. A.4 into A.1 yields

$$\frac{dC}{dy} = -\frac{\sqrt{Dt}}{x} \frac{d^2 C}{dy^2} \quad (\text{A.5})$$

Equations.A.5 and A.2 are combined into:

$$\frac{dC}{dy} = -\frac{1}{2y} \frac{d^2 C}{dy^2} \quad (\text{A.6})$$

Integrating Equation. A.6 gives:

$$\int dC = B \int e^{-y^2} dy \quad (\text{A.7})$$

Thus, the solution of C:

$$C = \begin{cases} A_1 \operatorname{erf}\left(\frac{x}{2\sqrt{Dt}}\right) + A_2 & \text{at } x < 0 \\ B_1 \operatorname{erf}\left(\frac{x}{2\sqrt{Dt}}\right) + B_2 & \text{at } x > 0 \end{cases} \quad (\text{A.8})$$

The boundary conditions are given below:

$$\begin{cases} C(x < 0, t = 0) = C_i^g \\ C(x > 0, t = 0) = C_i^l \end{cases} \quad (\text{A.9})$$

After incorporating the following relationships:

$$\begin{cases} \lim_{y \rightarrow -\infty} \operatorname{erf}(y) = -1 \\ \lim_{y \rightarrow \infty} \operatorname{erf}(y) = 1 \end{cases} \Rightarrow \begin{cases} -A_1 + A_2 = C_i^g \\ B_1 + B_2 = C_i^l \end{cases} \quad (\text{A.10})$$

The interfacial boundary conditions ($x=0$, t) are:

$$\begin{cases} C_{g,i} = HC_{l,i} \\ D_l \frac{\partial C_{l,i}}{\partial \bar{n}} = D_g \frac{\partial C_{g,i}}{\partial \bar{n}} \end{cases} \quad (\text{A.11})$$

Combing Equation. A.11 with Equation.A.8 yields:

$$\begin{cases} A_2 = HB_2 \\ A_1 = B_1 \end{cases} \quad (\text{A.12})$$

Hence, combining Equation s. A.10 and A.12 are the analytical solutions of Equation. A.1 for the concentration becomes

$$C_i(x, t) = \begin{cases} \frac{HC_i^g}{H+1} \operatorname{erf}\left(\frac{x}{2\sqrt{Dt}}\right) + \frac{C_i^g}{H+1}, & x < 0 \\ \frac{HC_i^g}{H+1} \operatorname{erf}\left(\frac{x}{2\sqrt{Dt}}\right) + \frac{H}{H+1}, & x > 0 \end{cases} \quad (\text{A.13})$$

Appendix B

This Python script is designed to generate a two-dimensional porous medium composed of non-overlapping circles and export the result as a DXF file. The porous medium and its properties are specified and visualized using Python libraries such as NumPy, Matplotlib, and ezdxf. Here's a detailed overview of the script's functionality and components:

```
1. import numpy as np
2. import matplotlib.pyplot as plt
3. import ezdxf
4. from scipy.spatial.distance import cdist
5. def generate_porous_medium(L1, L2, R1, R2, max_attempts=20000):
6.     circles = np.array([]).reshape(0, 3) # Initialize as an empty array with 3 columns
7.     min_gap = R1 / 2 # Minimum gap (half of the smallest radius)
8.
9.     while max_attempts > 0:
10.         r = np.random.uniform(R1, R2)
11.         x = np.random.uniform(r, L1-r)
12.         y = np.random.uniform(r, L2-r)
13.
14.         # Check if it overlaps or is too close to existing circles
15.         if circles.size == 0 or all(cdist([(x, y)], circles[:, :2]).min() >= circles[:, 2] + r + min_gap):
16.             circles = np.vstack([circles, [x, y, r]])
17.             max_attempts -= 1
18.
19.     return circles
20.
21. def plot_circles(circles, L1, L2):
22.     fig, ax = plt.subplots()
23.     for x, y, r in circles:
24.         circle = plt.Circle((x, y), r, edgecolor='b', facecolor='none')
25.         ax.add_patch(circle)
26.     ax.set_aspect('equal', adjustable='box')
27.     plt.xlim(0, L1)
28.     plt.ylim(0, L2)
29.     plt.show()
30.
```

```
31. def export_to_dxf(circles, filename):
32.     doc = ezdxf.new(dxfversion='R2010')
33.     msp = doc.modelspace()
34.     for x, y, r in circles:
35.         msp.add_circle(center=(x, y), radius=r)
36. doc.saveas(filename)
37. # Parameters
38. L1, L2 = 2000, 5000
39. R1, R2 = 35, 37.5
40.
41. # Generate and plot the porous medium
42. circles = generate_porous_medium(L1, L2, R1, R2)
43. plot_circles(circles, L1, L2)
44. plt.show()
45.
46. # Export to DXF
47. export_to_dxf(circles, 'C:/Username/Desktop/2D_circls_porous_medium.
    dxf')
```